

Dissertation

submitted to the
Combined Faculty of Mathematics, Engineering
and Natural Sciences
of Heidelberg University, Germany
for the degree of
Doctor of Natural Sciences

Put forward by

Florian Trost

born in Hagen

Oral examination: 10. May 2023

Time-resolved Fragmentation of
Diiodomethane studied in an XUV
Pump-Probe Experiment

Referees: Priv.-Doz. Dr. Robert Moshhammer

Priv.-Doz. Dr. Wolfgang Quint

Abstract

The dissociation dynamics of diiodomethane molecules (CH_2I_2) have been investigated in a 97.6 eV XUV-pump XUV-probe measurement at the reaction microscope endstation at the free-electron laser FLASH2. Ionic fragments created by 4d inner-valence ionisation followed by Auger decay have been detected in coincidence, enabling a kinematically complete reconstruction of the dissociation pathways. In the $\text{CH}_2^+ + \text{I}^+ + \text{I}^+$ one-photon absorption channel a concerted three-body breakup and a sequential dissociation via a rotating intermediate CH_2I^{++} ion have been identified. Classical simulations have been performed, and are compared to the data and to 'Atom Centered Density Matrix Propagation' (ADMP) calculations conducted by Martín et al. Both types of simulations reproduce different aspects of the observed fragmentation dynamics. In the time-resolved two-photon absorption channels $\text{I}^{+++} + \text{CH}_2\text{I}^+$ and $\text{CH}_2^+ + \text{I}^{+++} + \text{I}^+$, charge transfer occurs at short internuclear distances leading to suppression of the I^{+++} charge state formation. The timescales of charge transfer in the two different dissociation channels have been measured to be (200 ± 11) fs for $\text{I}^{+++} + \text{CH}_2\text{I}^+$ and (119 ± 15) fs for $\text{CH}_2^+ + \text{I}^{+++} + \text{I}^+$.

Zusammenfassung

Die Fragmentationsdynamik von Diiodomethan-Molekülen (CH_2I_2) wurde in einem XUV-Pump-XUV-Probe-Experiment bei 97.6 eV an der Reaktionsmikroskop-Einrichtung am Freie-Elektronen-Laser FLASH2 untersucht. Die geladenen Ionen, die durch Innervalenz-Ionisation der 4d-Schale gefolgt von Auger-Zerfall entstehen, wurden in Koinzidenz detektiert, sodass eine kinematisch vollständige Rekonstruktion der Fragmentierung möglich ist. Im Dissoziationskanal $\text{CH}_2^+ + \text{I}^+ + \text{I}^+$, welcher durch die Absorption eines Photons eingeleitet wird, konnten ein direkter drei-Ionen-Zerfall und ein sequenzieller Zerfall über den Zwischenschritt eines rotierenden CH_2I^{++} ions festgestellt werden. Klassische Simulationen wurden durchgeführt und mit den experimentellen Daten sowie mit „Atom Centered Density Matrix Propagation“ (ADMP) Simulationen von Martín et al. verglichen. Beide Simulationsmethoden können unterschiedliche Aspekte der beobachteten Fragmentierung des Moleküls reproduzieren. In der zeitaufgelösten Untersuchung der beiden Dissoziationskanäle $\text{I}^{+++} + \text{CH}_2\text{I}^+$ und $\text{CH}_2^+ + \text{I}^{+++} + \text{I}^+$ konnte Ladungstransfer bei kurzen Abständen der Ionen zueinander festgestellt werden, welche die Entstehung von I^{+++} Ionen unterdrücken. Die Zeitskalen des Ladungstrfers in den beiden Kanälen konnten bestimmt werden mit (200 ± 11) fs für $\text{I}^{+++} + \text{CH}_2\text{I}^+$ und (119 ± 15) fs für $\text{CH}_2^+ + \text{I}^{+++} + \text{I}^+$.

Contents

1	Introduction	1
2	Background Information	5
2.1	Light-matter interaction	5
2.1.1	Inner-valence ionisation	7
2.1.2	Auger decay	8
2.2	Diiodomethane	11
2.3	Classical Simulation	13
2.4	Electronegativity	17
2.5	The Physics of Coincidence Lines	19
2.5.1	PiPiCo lines	22
2.5.2	TriPiCo lines	28
2.5.3	Charge-scaling of flight times	32
3	Experimental Setup	39
3.1	XUV beamline and mirror chamber	40
3.2	Reaction Microscope	43
3.2.1	The Spectrometer	44
3.2.2	MCP detectors: measuring time	47
3.2.3	Delaylines: measuring position	50
3.3	Target Delivery System	50
3.4	Data Acquisition	53
3.5	Subsequent Updates of the Setup	53
4	Data Calibration and Analysis	55
4.1	<i>acquire</i> step	56
4.2	<i>unpack</i> step	56
4.3	<i>calc</i> step	62

Contents

4.3.1	Ion identification	62
4.3.2	Momentum calculation	63
4.3.3	Momentum resolution	66
4.3.4	Coincidence detection	67
5	Fragmentation Dynamics of Diiodomethane	69
5.1	Dissociation by absorption of a single XUV photon	72
5.1.1	Single Auger decay: 2 charges	72
5.1.2	Double Auger decay: 3 charges	76
5.1.3	ADMP Simulation of CH ₂ I ₂ fragmentation	83
5.2	Charge transfer in diiodomethane dissociation fragments	90
5.2.1	Dynamics of two-ion dissociation channel I ⁺⁺⁺ + CH ₂ I ⁺	91
5.2.2	Charge transfer dynamics in three-ion dissociation channels	94
6	Summary and Outlook	101
A	Atomic units	105
B	Inequation estimate	106
	Bibliography	108

Chapter 1

Introduction

One of the aims of atomic physics is to gain a better understanding of the fundamental processes in and between atoms, especially after ionisation and excitation occurs. To this end, the behaviour of systems of atoms, such as molecules and clusters, is observed after they have absorbed energy. This energy may come from interaction with projectiles such as highly charged ions [48, 62], high-energy electrons [9] or from the absorption of photons as in this work. In many cases, these interactions result in the dissolution of the original system through the emission of electrons and, in some cases, through breaking of the bonds that hold the atomic constituents together. The fragments of such dissociations, electrons, atomic or molecular ions, and neutral particles, can be detected to gain insight into the fragmentation processes and, therefore, into the fundamental nature of atomic systems.

Detecting the ionic fragments from a dissociation event and measuring the kinetic energy they received from the process can give information about their relation to other atoms in the original system. In addition, information on the process of dissociation itself can be obtained, especially regarding energy and charge re-distribution within the system after excitation occurred. Processes that have been discovered in excited atomic systems include inter-atomic Coulombic decay (ICD) [61], charge transfer (CT) [59], radiative charge transfer (RCT) [20, 51], and electron-transfer mediated decay (ETMD) [52, 68].

By detecting more than one fragment from the same original system in coincidence, one can measure correlations between the fragments' kinetic energies and momenta. In measuring the properties of all the final fragments of a dissociation process, information on the dynamics of the breakup of the original system can be inferred. However, to detect the changes an atomic system experiences after excitation in a more defined way, it is necessary to deploy a time-resolved meas-

urement technique, such as the pump-probe method. By varying the time delay between the two excitations it is possible to indirectly observe the dynamics of the fragmentation process initiated by the first excitation. The measured properties of the dissociation fragments will then depend on the time delay between the two excitation processes. This measurement technique has been employed with great success to study, for example, charge transfer dynamics in argon dimers [59] and hydrogen migration in ethanol molecules [26].

The timescale of dynamics in atomic systems is the femtosecond (10^{-15} s). The observation of events during such short times requires a physical process on the same scale. Ultrashort laser pulses are one such process that is used to initiate dynamics in atomic systems through excitation and ionisation. The temporal resolution of such measurements is, ultimately, limited by the duration of the laser pulse.

Studying the dissociation dynamics of molecular systems into more than two fragments is especially interesting because of the possibility to observe different and sometimes competing dissociation pathways. For example, a direct fragmentation into three ions as well as a sequential breakup process via an intermediate molecular ion has been observed in several small molecules such as CO_2 [42], OCS [28], and SO_2 [30].

Detecting all fragments of a dissociation event in coincidence and analysing their correlated momenta can give information on the dissociation pathways. Gaining knowledge about possible intermediate ionic states and their properties is of interest for better understanding the intra-molecular processes that lead to fragmentation. In several studies the intermediate molecules of sequential fragmentations have been reported to rotate [19, 49, 67]. Information on the rotational frequency as well as the lifetime of the intermediate state would illuminate the processes that lead to sequential fragmentation, especially the inter-atomic dynamics of the intermediate molecular ions.

This work has studied the fragmentation dynamics of diiodomethane (CH_2I_2) to gain information on the dynamics of three-body dissociation in molecules after ionisation. The two iodine ions in various charge states as well as the CH_2^+ group have been detected in coincidence. Their momentum correlations give insight into the dissociation dynamics, showing the prevalence of both concerted and sequential dissociation channels.

The CH_2I_2 molecules were irradiated with 97.6 eV photons delivered by the Free-Electron Laser FLASH2 in Hamburg. FLASH2 provided extreme ultraviolet (XUV) pulses of approximately 50 fs duration. The pulses were split into two parts and

an adjustable time delay between zero and 1 ps was created between them such that the dynamics of the fragmentation processes could be measured in a pump-probe setup.

The iodine atom has a giant shape resonance at a photon energy around 90 eV. The absorption cross section of iodine atoms in this energy region is dominated by 4d inner-valence ionisation [41]. When the photoelectron leaves the atom, the created ion is in an excited state because of the hole in its 4d shell. It can undergo single or double Auger decay, resulting in a doubly or triply charged iodine ion [41]. Creating up to three charges with a single photon absorption is an efficient way of introducing several charges into molecular systems without directly affecting the molecular bonds. Excitation of the CH_2I_2 molecule triggers several different dissociation channels which are the subject of this work.

This thesis is structured as follows: Chapter 2 gives an overview of the physical processes relevant for the presented data such as inner-valence ionisation, giant shape resonances, and coincident detection of fragmentation products. The experimental setup on which the measurements were performed is presented in Chapter 3. The following Chapter 4 describes the data analysis with a focus on the calibration method for ion momentum calculation. The results of the measurement regarding ion momentum correlation in two- and three-body dissociations of CH_2I_2 molecules are presented and interpreted in Chapter 5. The final Chapter 6 summarises the results.

Chapter 2

Background Information

This chapter provides information on the different concepts and methods that are necessary to understand and contextualise the content presented in this work. Some aspects are kept brief with references to more detailed sources and publications. Other parts, such as the subject of coincidence lines, are covered more extensively and are meant to provide a general understanding of the underlying physical concepts.

The chapter is structured as follows: Section 2.1 provides a brief introduction into the concept of ionisation with emphasis on inner-valence ionisation and Auger decay. The target, diiodomethane, whose nature is the central topic of this work, is introduced in Section 2.2. Section 2.3 explains the classical simulation methods used to reproduce the fragmentation behaviour of CH_2I_2 molecules and Section 2.4 gives a brief summary of the concept of electronegativity. The final, most extensive Section 2.5 explains the nature, appearance, and interpretation of coincidence lines.

2.1 Light-matter interaction

This section gives a brief overview of the concept of photoionisation before inner-valence ionisation is covered in Section 2.1.1. More detailed information on ionisation processes in general can be found in [16].

There exist many different phenomena regarding the interaction of light with matter. The known effects range from elastic and inelastic scattering to processes in particle physics such as pair creation.

One of the fundamental interactions of light with matter is ionisation. In general, ionisation is the process of separating electrons from atoms, molecules or ions by photon interaction. Its most simple category is the absorption of a photon by an atom and the resulting emission of a photoelectron.



The sum of the kinetic energy of the photoelectron and the ion is equal to the difference of the photon energy $\hbar\omega$ and the binding energy E_b of the electron in the atom. In addition, the vector sum of the momenta of all involved particles is preserved.

$$E_{\text{kin}, e^-} + E_{\text{kin}, A^+} = \hbar\omega - E_b \quad (2.2)$$

The probability for atom-photon interaction is quantified by the interaction cross section. The cross section depends on the specific target and the photon energy. At low photon energies (around 10 eV) the most probable process is ionisation of a valence electron, leaving the created ion in its electronic ground state. At high photon energies (several keV), the cross section is dominated by Compton scattering, and at even higher energies (several MeV), pair production occurs.

At intermediate photon energies (several 10s to several 100s of eV), ionisation of non-valence electrons can occur. In this process, an electron from the inner shells of an atom or molecule interacts with the photon. When such an electron is emitted, it leaves behind a hole in the respective electronic shell and the created ion is not in its electronic ground state.

A core-hole excited ion can de-excite in a variety of ways, depending on the state of excitation and the ion's surroundings. An excited ion can, for example, relax radiatively by photon emission or by the emission of secondary electrons, for example by Auger decay. If there are other atomic systems in its vicinity, additional relaxation processes are possible through interaction with its surroundings, such as inter-atomic Coulombic decay (ICD) [61], charge transfer (CT) [59], radiative charge transfer (RCT) [20, 51], and electron-transfer mediated decay (ETMD) [52, 68]. All of these processes have different timescales and when multiple relaxation pathways are possible the faster processes tend to suppress the slower ones. It is therefore important to choose a suitable atomic or molecular system for the investigation of a specific relaxation process.

2.1.1 Inner-valence ionisation

The ionisation of non-valence electrons is closely connected to the emergence of so-called giant resonances in photon absorption processes. At certain photon energies, the total interaction cross section is dominated by the cross section for inner-valence ionisation, such as ionisation of 4d electrons in xenon [2] and iodine [41].

Here, a brief description of the emergence of giant resonances for inner-valence ionisation is given. It is summarised from [7] and [10] which give a more in-depth explanation of the effect.

The effective potential for atoms other than hydrogen can be described as the sum of a Coulomb attraction and a repulsive term due to centrifugal force connected to the angular momentum quantum number l :

$$V_{\text{eff}}(r) = V_{\text{Coulomb}}(r) + \frac{l(l+1)\hbar^2}{2m_e r^2} \quad (2.3)$$

Such a potential can for some atoms assume the form of a ‘double valley potential’ (see Figure 2.1). The reason for the emergence of the inner valley is that screening effects of the nuclear charge by the surrounding electrons decreases for shorter distances such that the Coulomb term can dominate again. For even smaller distances the r^{-2} term takes over and forms the inner barrier of the potential.

An electron exposed to such a double valley potential can become localised in the inner valley for specific values of Z and l which is called a ‘wave function collapse’. The exact nature of this collapse is very sensitive to the detailed shape of the effective potential.

For example, the wave function of a 4d shell electron can collapse into the inner potential valley for some values of Z . The collapsed wave function of the 4d electron then has a large spatial overlap with the 4f state wave function which makes transitions between these two shells very probable upon excitation. In iodine, the energy of the 4f state is above the ionisation threshold. It is therefore possible to not only excite but ionise an iodine atom via the 4d giant resonance. This picture gives a useful explanation of the emergence of giant resonances for inner-valence ionisation processes.

The spatial overlap of the ground state wave function and the wave function of the excited state may be very small at energies around the ionisation threshold. It only increases for higher photon energies and consequentially higher kinetic

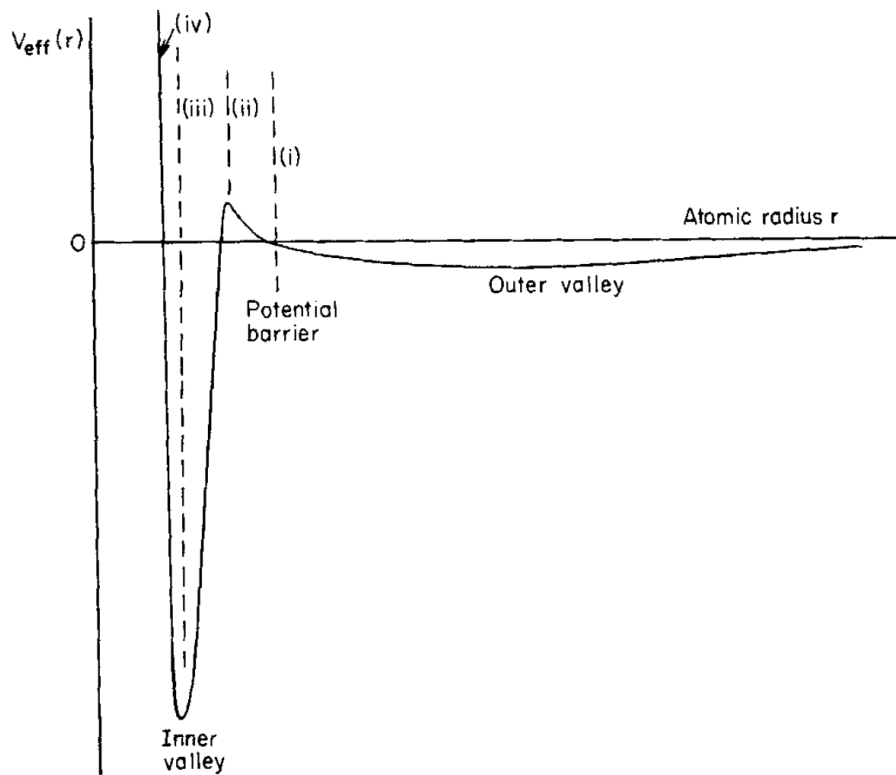


Figure 2.1: Principle structure of a double valley potential (not to scale). Figure from [10].

energy of the photoelectron. It is for this reason that the maximum interaction cross section for the giant resonance appears not at the ionisation threshold but at higher photon energies. This effect is called the delayed onset. It can be observed in iodine atoms where the binding energy of the 4d electrons is between 57 and 60 eV (depending on the specific sub-level) whereas the maximum of the 4d inner-valence ionisation cross section peaks at a photon energy of around 90 eV [41]. For even higher photon energies the wave function overlap decreases again such that a broad maximum in cross section is formed.

2.1.2 Auger decay

Auger decay is a specific form of relaxation for excited atomic systems [38]. The effect is observed in ions that have been created through inner-valence or core ionisation [2, 27]. In Auger decay, an electron changes from a state of higher energy to a state of lower energy to eliminate the hole in the inner shell, as sketched

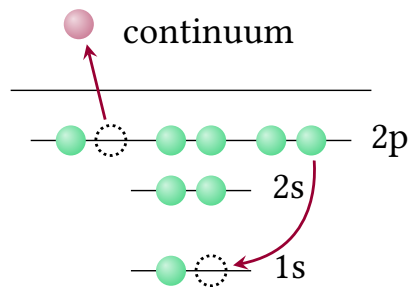


Figure 2.2: Sketch of Auger decay in a core hole-excited neon ion. Figure adapted from [60].

in Figure 2.2. The energy difference that is released by this process causes one or several electrons to be ejected from the ion. The electrons that are emitted during Auger decay must have had a combined binding energy lower than the energy difference between the two states of the electronic transition, otherwise they could not have been freed from the ion.

When one electron is emitted through this form of de-excitation, the process is called single Auger decay. The Auger electron has a specific kinetic energy that is determined by its binding energy subtracted from the energy difference of the electronic transition. Electron spectroscopy can therefore be used to identify Auger electrons and obtain information on the excited system [34].

Auger decay can involve the emission of more than one electron [6]. When two Auger electrons are emitted, the process is called double Auger decay, in contrast to single Auger decay with only one Auger electron. Double Auger decay has been detected in xenon atoms after 4d inner-valence ionisation [45] where both Auger electrons have been measured in coincidence with the xenon ion. The relaxation processes identified show a sequential emission of the two Auger electrons with high correlation of their kinetic energies. They do no longer need to have characteristic energy values as in the single Auger process, but the sum of their kinetic energies is constant, as indicated by the diagonal lines in Figure 2.3).

By analysing the width of the measured energy peaks, the lifetime of the original excited xenon ion prior to Auger decay has been found to be on the order of a few femtoseconds. Similar results have been obtained for Auger decay in molecular iodine and other molecules containing iodine atoms [11]. For double Auger decay, the intermediate state between the two Auger electron emissions has been found to have a longer lifetime (> 23 fs) than the original excited state [45].

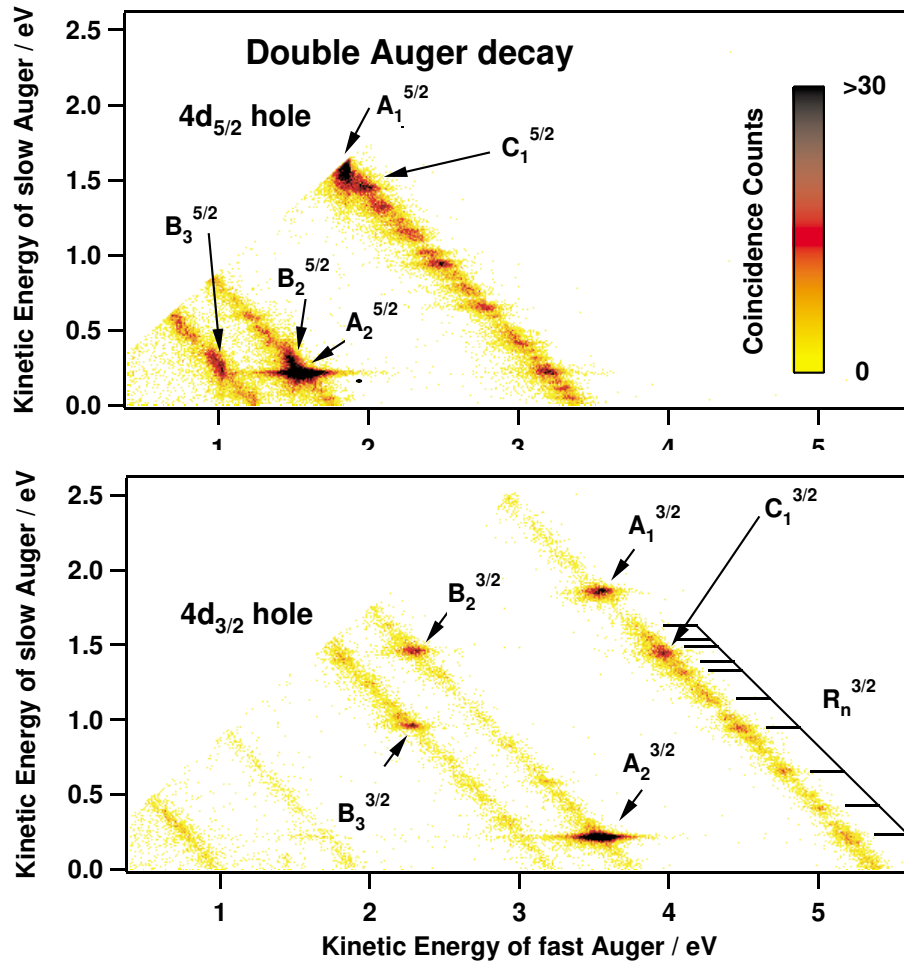


Figure 2.3: Two-dimensional energy spectrum of the two Auger electrons emitted from 4d-hole-excited xenon ions. The electrons have been detected in coincidence with the Xe³⁺ ions. Figure from [45].

2.2 Diiodomethane

Diiodomethane (CH_2I_2) is a small molecule consisting of five atoms: a carbon atom in its centre surrounded by two iodine atoms and two hydrogen atoms each connected to the carbon atom by a covalent bond. It can be described as a methane molecule where two hydrogen atoms have been exchanged for iodine atoms. Its ground state geometry is displayed in Figure 2.4.

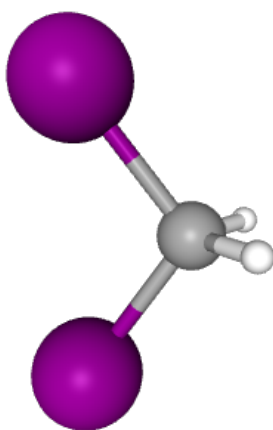


Figure 2.4: 3D structure image of the ground state geometry of diiodomethane. Iodine in violet, carbon in grey, hydrogen in white. The C–I bond length is 212 pm (4.0 au) and the I–I distance is 341 pm (6.4 au). Figure and ground state geometry from [47].

This molecule has been used as a model for studies of fundamental interactions in quantum systems in a variety of ways. There are several reasons for its popularity in this field:

- It contains two iodine atoms that act as absorption centres with a high cross section. It is therefore possible to excite a variety of different states that trigger different molecular dynamics such as charge transfer and structural changes. However, diiodomethane is still a small molecule with a manageable amount of fragmentation pathways.
- The CH_2I_2 molecule consists of three major groups which are the two iodine atoms and the methylene group CH_2 . It is therefore in principle possible to observe molecular fragmentation dynamics into three parts which

opens up a the opportunity to observe different molecular dynamics compared to systems containing only two major groups, such as CH_3I and I_2 .

- Iodine has a giant resonance for inner-valence ionisation (see Section 2.1.1 for details) in the XUV regime of photon energies. This enables the deposition of a large amount of energy in the molecule through creation of a 4d-hole-excited state without directly affecting the molecular bonds. The subsequent relaxation dynamics which involve Auger decay and charge transfer provide opportunities to study the fundamental dynamics of excited atomic systems.
- An additional advantage iodine has over other heavy absorption centres is that it has only one stable isotope, ^{127}I . This makes it much easier to do momentum reconstruction from measured time and position data because all iodine fragments of a specific charge state behave identically with regard to the detection method. Xenon, for example, has seven stable or metastable isotopes of significant abundance which makes coincidence measurements somewhat more challenging.

Diiodomethane has been studied as a model system in atomic physics for many decades. Existing studies on CH_2I_2 include experiments on gas-phase fragmentation dynamics in the gas phase [8, 22, 24, 33] and in solution [43, 64], theoretical calculations [32, 53] and transient absorption measurements [50, 65].

Photoelectron-photoion coincidence measurements after irradiation with 40 eV photons have been done by [8]. A dissociation channel was detected in which a neutral iodine atom was emitted. Calculations performed in the same study suggest that the dissociation may occur via an intermediate iso-diiodomethane radical $(\text{CH}_2\text{I}-\text{I})^{\bullet+}$.

In a recent transient absorption measurement at 50.4 eV conducted by [50], the isomerisation process described by [8] was found in the time-dependent absorption change of the CH_2I_2 molecule. The dissociation was found to be completed after around 400 fs.

The neutral dissociation into molecular iodine and a methylene group (CH_2) has been observed by [33] following one-photon absorption of 310 nm. The process was found to be fast (less than 100 fs) and concerted, meaning that no intermediate state was identified.

Recently, fragmentations of diiodomethane into three particles have been measured by [22] after strong field ionisation with an intense infrared laser pulse. The three ionic coincident fragments detected are CH_2^+ and two iodine ions of various charge states. Single-pulse measurements lead to three-body fragmentation into the $\text{CH}_2^+ + \text{I}^+ + \text{I}^+$ coincidence channel where different fragmentation pathways have been identified through momentum correlation between the created ions. These findings will be compared to the results of the measurements presented in this work later in Chapter 5.

2.3 Classical Simulation

Different types of simulations have been performed within this work. Classical simulations were used to gain insight into the qualitative nature of specific dissociation channels of the CH_2I_2 molecule. In addition, more sophisticated ‘Atom Centered Density Matrix Propagation’ (ADMP) simulations were performed by Martín et al. and provide a more general view on the fragmentation dynamics of charged diiodomethane molecules. The method of classical simulation is explained in this section. More details on the ADMP simulation are given in Section 5.1.3.

The classical model uses the electrostatic repulsion between point charges to simulate the fragmentation of diiodomethane molecules. The results are compared to the measurements in Chapter 5. It must be stated at the beginning that this is an extremely simplified model for molecular dynamics. The reason why the results of such simplified calculations are presented here is that they do in fact reproduce the qualitative features of the measured fragments’ momentum correlations. However, due to the model’s limitations, this simulation method should not be expected to correctly describe the details of the observed dissociation dynamics.

The simulation of electrostatic repulsion between point charges operates on a Coulombic potential. It does not take into account any electron interactions and only considers positively charged dimensionless nuclei. The charges are not distributed over the atoms and molecules they are assigned to, but localised to specific points in space. This is a simplification because even neutral molecules such as CH_2 have an internal charge distribution. Specifically, the simulated CH_2^+ molecule is treated as a single dimensionless particle without any rotational or vibrational motion.

When a binding potential between two nuclei is simulated, it is done so without regard for actual covalent binding potential shapes. It only serves the purpose of keeping the distance between the respective nuclei constant for a specific amount of simulated time. The simulation does not conserve energy because of its non-ideal Euler integration method. Energy conservation is explicitly violated in the cases when the binding potential is switched off after a pre-determined amount of time to cause the previously bound nuclei to dissociate. The simulation model does also not account for any type of charge rearrangement or transfer.

Momentum conservation of the simulation is empirically checked by comparing the sum of the momenta of all simulated particles at the first and at the last time step. Since the initial momentum of all individual particles is always zero, the total momentum sum at the end of a simulation scenario is a measure for momentum conservation.

When no binding potential is simulated, the momentum sum deviates from its initial value within around 0.1 au or 0.05 % of the final particle momenta. When a binding potential is used, the total momentum sum deviates from zero with increasing potential lifetime due to computational errors. For the longest lifetimes simulated, which are 1 ps, the total momentum error is 20 au, or approximately 15 % of the final particles' momenta.

The classical simulation calculates repulsion between point charges due to electrostatic force. For a point charge Q , the force it experiences from the presence of other charges q_i at distances r_i is

$$F_{\text{el}} = \sum_i F_{\text{el},i} = Qk_e \sum_i \frac{q_i}{r_i^2}, \quad (2.4)$$

with k_e being the Coulomb constant. Each point charge is assigned a mass according to the particle it represents. The simulation calculates the acceleration caused by electrostatic repulsion for each charge and derives the resulting changes in velocity and position via the Euler method. It then propagates the system to the next time step and starts over. The simulation uses three spatial dimensions for ion movement. However, since all objects are initially placed in the $x - y$ -plane and no force acts on them outside of that plane, their movement is confined to $z = 0$. All calculations in the simulation are done in atomic units. The time step is varied between 0.01 and 10 fs according to the acceleration the ions experience with higher acceleration leading to smaller time steps. The simulation is adjusted to terminate after a fixed time limit of 2 ns or after the residual electrostatic potential energy has fallen below a pre-defined fraction (10^{-6}) of the initial potential energy, whichever condition is reached first. When the simulation has terminated, the point charges' final positions and velocities are saved.

For point charges of equal sign, the resulting electrostatic forces will be purely repelling, as is the case for the Coulomb-exploding molecular systems that are simulated. The initial potential energy is gradually transferred into the ions' kinetic energy. For example, for the simulation of the direct three-body fragmentation of CH_2I_2 into two I^+ and one CH_2^+ ion, three unit point charges $+e$ were simulated. The charges were placed at the positions of the nuclei of the carbon and iodine atoms and given the respective masses. The positions of the nuclei in the neutral ground state geometry of CH_2I_2 were taken from [47]. Figure 2.5 shows the simulated ion trajectories for this initial arrangement of particles at different time steps. The CH_2^+ ion is repelled equally by the two iodine ions and therefore moves away in a straight line. The two I^+ are first mainly repelled by the CH_2^+ group, but since it is departing quickly, their later movement is dominated by mutual electrostatic repulsion. In general, the CH_2^+ group is moving away much more rapidly due to its lower mass (~ 14 u compared to ~ 127 u for iodine).

For the fragmentation into $\text{CH}_2^+ + \text{I}^+ + \text{I}^+$ it is clear that the three charges must be located at the three fragments. However, in the case of the CH_2^+ group, it is not certain where exactly the charge is located, whether at the carbon atom or at one of the hydrogen atoms or somewhere in between. It is similarly difficult to predict the charge localisation in molecular ions such as CH_2I^+ and CH_2I^{++} . The concept of electronegativity (see Section 2.4) may provide some guidelines for assumptions, but fundamentally it is not known where the charge within these ionic fragments is located.

For the simulation of sequential dissociation events an additional force on the nuclei is introduced in the form of a binding Lennard-Jones potential [21] of the form:

$$V_{\text{LJ}} = 4\epsilon \left[\left(\frac{\sigma}{r_{i,j}} \right)^{12} - \left(\frac{\sigma}{r_{i,j}} \right)^6 \right] \quad (2.5)$$

Here ϵ is a scaling parameter for the depth of the potential well. σ marks the position of the zero point of the potential and is therefore used to adjust the potential minimum. $r_{i,j}$ represents the distance between two charges i and j . The Lennard-Jones potential is most commonly used to describe the binding potential of neutral atoms based on van der Waals force. It was chosen here because of computation efficiency with regard to obtaining its derivative for the calculation of forces from the potential.

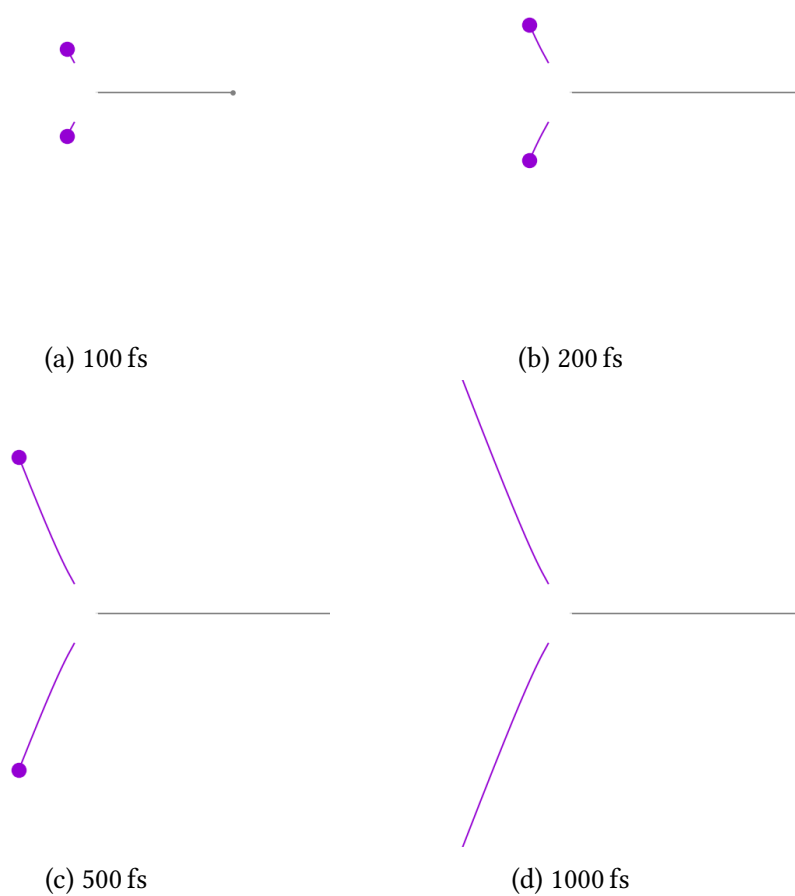


Figure 2.5: Simulated trajectories of the fragments of a direct triple dissociation of CH₂I₂ into two I⁺ ions (large violet circles) and a CH₂⁺ ion (small grey circle).

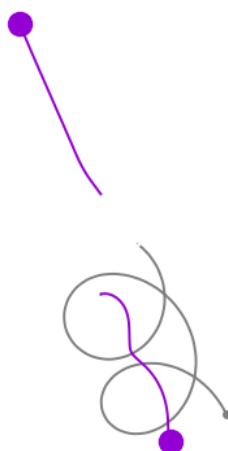


Figure 2.6: Simulation of CH_2I_2 dissociating into I^+ and CH_2I^+ . The neutral I is bound to the CH_2^+ group by a Lennard-Jones potential. The molecular ion starts to rotate as a result of the electrostatic repulsion between the iodine ion and the CH_2^+ group.

The Lennard-Jones potential is added to the electrostatic potential and adjusted in height such that it forms binding states between charged particles ($\epsilon = 1$ au). The position of the potential minimum is identical to the initial bond length such that the initially created force is zero. After a pre-defined time interval, the Lennard-Jones potential is switched off to simulate dissociation of the previously bound particles. This switching off violates energy conservation because the particles' potential energy is changed without an equivalent change in their kinetic energy.

Figure 2.6 shows the simulated trajectories of the I^+ ion and the constituents of the molecular ion CH_2I^+ . A Lennard-Jones potential binds the iodine atom and the CH_2 group together. The charge in the CH_2I^+ fragment is placed at the carbon atom. The repulsion between the dissociating I^+ ion and the CH_2^+ group introduces a rotation in the molecular ion.

2.4 Electronegativity

The concept of electronegativity is closely related to molecular bonds. It can be understood as the propensity of atoms to attract the electrons of a chemical bond it participates in. The description given here is based on the electronegat-

ivity definition of Linus Pauling given in [39].

Electronegativity as a concept predates the modern understanding of atoms and it was used to explain in a qualitative way how molecules formed from different types of atoms. There have been different attempts to quantify electronegativity as a force to attract electrons. Because this attraction is only observable when atoms interact, electronegativity describes the nature of interactions instead of a quality of atoms itself. Therefore, Pauling used properties of molecular bonds to assign numeric values to atoms in order to describe their electronegativity [44].

For a hypothetical molecule consisting of the two different atoms A and B, the term $D(A-B)$ describes its binding energy. Similarly, $D(A-A)$ and $D(B-B)$ are the binding energies of two molecules containing identical atoms. The energy Δ' is the difference between the binding energy of A - B and the geometric mean of the binding energies of A - A and B - B:

$$\Delta' = D(A-B) - \sqrt{D(A-A) \cdot D(B-B)} \quad (2.6)$$

This energy difference is related to the difference in electronegativity χ_A and χ_B of the atoms A and B:

$$\Delta'(A-B) = 30 (\chi_A - \chi_B)^2 \quad (2.7)$$

With this definition of electronegativity, a value can be assigned to each atom to quantify its affect to cause the measured energy difference Δ' , which is related to the atom's power to attract binding electrons. The number 30 in Equation (2.7) was chosen arbitrarily to obtain numbers of convenient size, between approximately 0.8 and 4. Small atoms with strong oxidising capability (such as fluorine and oxygen) have the highest values of electronegativity, large alkali atoms with weakly bound valence electrons have the lowest electronegativity (for example rubidium and caesium). The electronegativity of carbon (2.55) and iodine (2.66) is similar while the value for hydrogen is slightly lower (2.20).

2.5 The Physics of Coincidence Lines

Understanding the nature of coincidence lines can help a great deal in analysing and interpreting data of fragmentation dynamics of atomic systems. This section explains what coincidence lines are and how they are related to the initial momenta of coincidentally detected particles. Here the focus lies on ion coincidences, but the results can be transferred to ion-electron coincidences.

When studying the fragmentation of atomic systems such as molecules, a common approach is to detect the fragments and infer what momentum they gained from the dissociation process. It is of special interest to detect fragments that originated from the same original system. Correlations in their momenta can reveal the underlying dynamics of the dissociation. When all fragments of a dissociation event have been detected, a complete picture of the fragments' momenta can be reconstructed.

The detection of more than one fragment from the same dissociation event is called a coincidence measurement. It requires experimental techniques with the ability to register the arrival of multiple fragments within a short time frame and with high detection efficiency. Momentum correlation between the fragments will result in correlated arrival times at the detectors. This effect will cause the appearance of coincidence lines which allow for the identification of the fragments involved in a dissociation event.

In this section it will be shown that the relation between the initial momenta of dissociation fragments and their time of detection is fundamentally non-linear, but can be approximated as linear. Additionally, it will be shown that the proportionality between momentum and arrival time depends on the charge state of the fragment. This is especially important when observing three-particle coincidences where differently charged ions are involved.

A coincidence plot is a two-dimensional scatter plot or histogram where the TOF values of the measured particles are displayed. An entry in such a plot always contains the TOF values of two of the detector hits from a pulse, one marked on the x -axis and one marked on the y -axis. For example: After a laser pulse there have been four hits detected on an MCP at four different times t_1 , t_2 , t_3 and t_4 . In a coincidence histogram these four TOF values would be represented as the following pairs: (t_1, t_2) , (t_1, t_3) , (t_1, t_4) , (t_2, t_3) , (t_2, t_4) and (t_3, t_4) . Each TOF value is paired with each other value, with the shorter time always in the first position. Assuming the TOF values were 1, 2, 3 and 4, the corresponding coincidence histogram for these TOF pairs is presented in Figure 2.7. The first

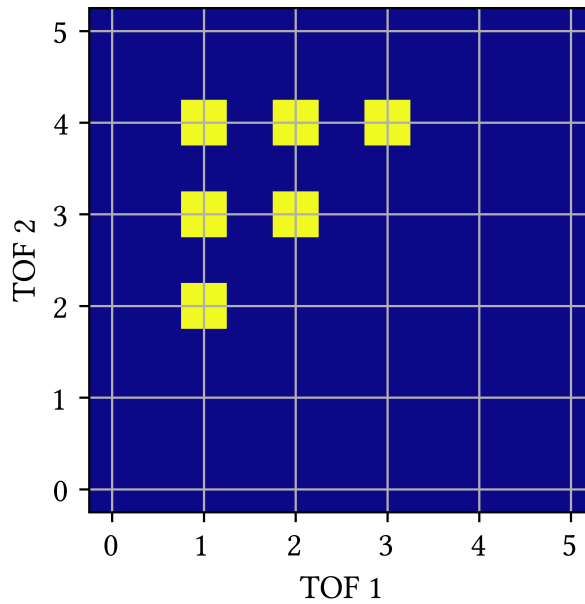


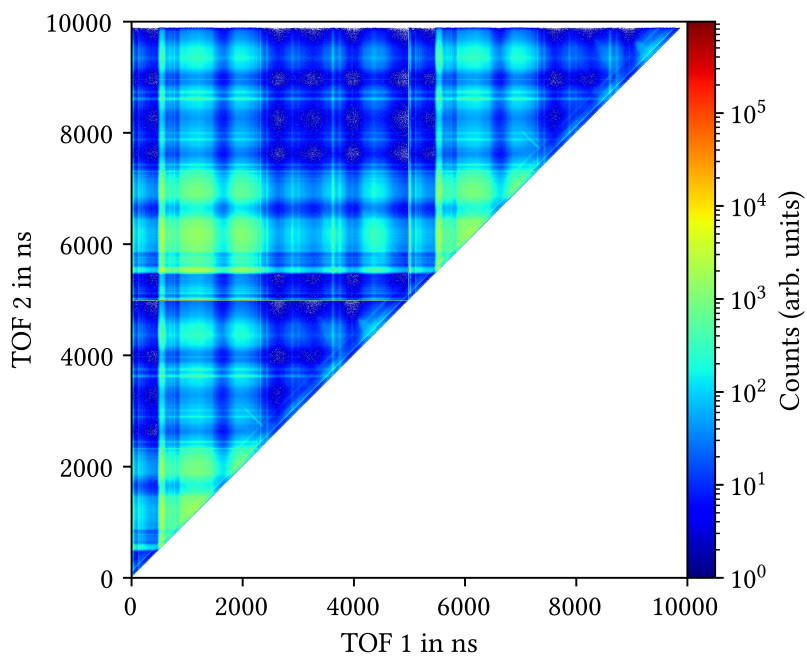
Figure 2.7: Example coincidence histogram with TOF pairs from a laser pulse with four detected particles. The TOF value of the particle that was detected first in each pair is represented on the x -axis.

entry of the pairs is plotted on the x -axis, the second on the y -axis. Thus, a laser pulse with four detected hits results in six entries in the coincidence histogram.

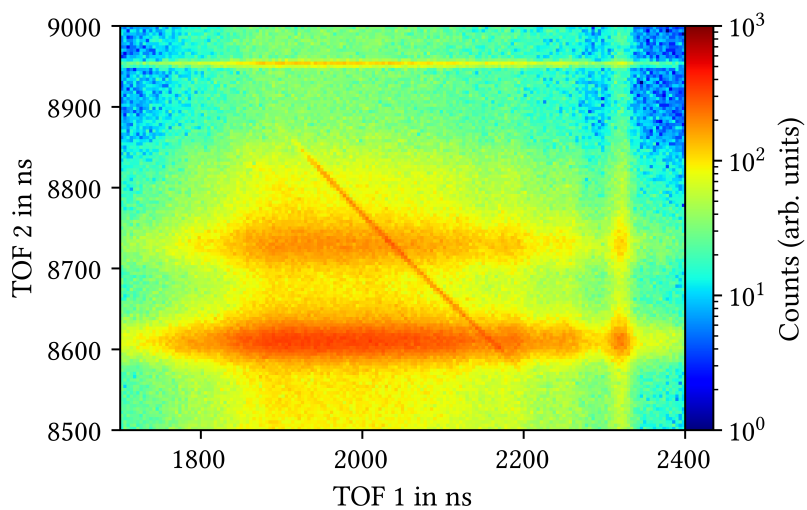
It is important to notice that by always plotting the first TOF value of each pair on the x -axis, the part of the histogram below its diagonal remains empty. In addition, the diagonal remains empty because it could only be populated by entries originating from identical TOF values, which cannot be detected.

The purpose of this representation is to check whether any pair of ion time-of-flight values correlate when aggregated over many laser pulses. A correlation does appear in the shape of a rather narrow line called a coincidence line, as shown in Figure 2.8.

The coincidence line reveals that the TOF values of the ions represented on that line are correlated. When the TOF value of one ion becomes shorter, the one of the other ion becomes longer. This is a strong indication that the two ions represented by pairs of TOF values on the line originate from the same dissociation event. In this regard, coincidence lines are an important tool in identifying coincidentally detected particles.



(a) Full coincidence histogram.



(b) Coincidence line example, here of CH_2^+ in coincidence with I_2^+ .

Figure 2.8: Examples of coincidence histogram and coincidence line from data set R947.

In the next subsections, it is explained out why coincidence lines appear and what gives them their characteristic shape. In addition, a close look is taken on the details of coincidence lines created by the detection of three ions.

2.5.1 PiPiCo lines

The term PiPiCo line stands for 'Photo-ion Photo-ion Coincidence line'. It refers to coincidence lines created by the coincident detection of exactly two fragments. When a particle interacting with a laser pulse dissociates into two charged fragments, due to momentum conservation their momenta are opposite to each other and equal in magnitude. The fragments' coincident detection will create an entry in the respective PiPiCo histogram. Where exactly this entry is depends on the specific TOF pair of the two fragments. The TOF value depends only on the z -component of the initial momentum the fragment receives from the dissociation (z -direction is defined to be positive towards the detector). Assuming equal charge and mass, the TOF values of two fragments will be equal if their initial momenta are parallel to the detector surface (zero momentum in z -direction). The difference in TOF values grows with increasing initial momentum in z -direction. It reaches a maximum for fragments ejected directly towards and away from the detector, respectively. Therefore, in the PiPiCo histogram, a line of entries appears for each fragmentation process that creates coincidentally detected fragments. The extent, shape, and slope of this line are the subject of interest of this subsection.

Fragments of equal mass and equal charge

It is assumed that the masses of the two fragments are equal, $m_1 = m_2 = m$, as well as their charges, $q_1 = q_2 = q$. In a spatially and temporally constant electric field, the particles experience identical constant acceleration a . The relation between the TOF value t and the distance s in a process of constant acceleration is

$$s(t) = \frac{1}{2}at^2 + v_0t. \quad (2.8)$$

Here v_0 is the initial velocity which depends on the initial momentum:

$$v_0 = \frac{p_0}{m} \quad (2.9)$$

Using this in Equation (2.8) and solving for t gives

$$t = \pm \sqrt{\frac{2s}{a} + \left(\frac{p_0}{am}\right)^2} - \frac{p_0}{am}. \quad (2.10)$$

Because only positive values for TOF are meaningful, the minus before the square root is neglected.

Note that both fragments will, regardless of their mass or charge, receive the same but opposite initial momentum. For the respective TOF values this means:

$$t_1 = t(p_0) \quad \Leftrightarrow \quad t_2 = t(-p_0). \quad (2.11)$$

The sum of the TOF values for the two fragments, t_1 and t_2 , is then

$$\begin{aligned} t_1 + t_2 &= t(p_0) + t(-p_0) \\ &= \sqrt{\frac{2s}{a} + \left(\frac{p_0}{am}\right)^2} - \frac{p_0}{am} + \sqrt{\frac{2s}{a} + \left(\frac{-p_0}{am}\right)^2} + \frac{p_0}{am} \\ &= 2\sqrt{\frac{2s}{a} + \left(\frac{p_0}{am}\right)^2} \end{aligned} \quad (2.12)$$

The sum of the two TOF values is not constant with respect to p_0 . For larger absolute values of initial momentum, $|p_0|$, the TOF sum increases. This means that the line in the PiPiCo histogram is not actually a straight line, but rather a slightly bent curve.

The actual shape of that line can be evaluated by finding a method to calculate t_2 not from p_0 but from t_1 . Then, one has obtained a direct equation for the lines that appear in the PiPiCo histogram.

This is done by starting to rearrange Equation (2.8) with $v_0 = p_0/m$ to p_0 :

$$p_0 = \frac{sm}{t} - \frac{1}{2}mat. \quad (2.13)$$

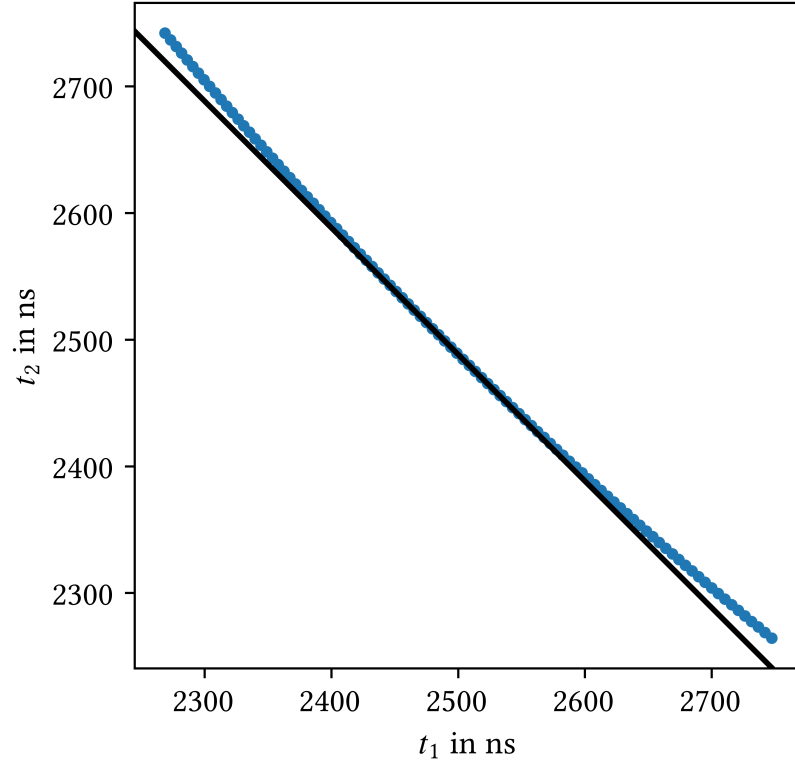


Figure 2.9: Calculated PiPiCo line for the two-fragment dissociation of an oxygen molecule into two O^+ ions with a hypothetical kinetic energy release of 10 eV. The straight line has a slope of -1 .

Now this is put into Equation (2.10) for t_2 :

$$\begin{aligned}
 t_2 &= t_2(-p_0) = \sqrt{\frac{2s}{a} + \left(\frac{-p_0}{am}\right)^2} + \frac{p_0}{am} \\
 &= t_2(t_1) = \sqrt{\frac{2s}{a} + \left(\frac{-\frac{sm}{t_1} + \frac{1}{2}mat_1}{am}\right)^2} + \frac{s}{at_1} - \frac{1}{2}t_1 \quad (2.14) \\
 &= \sqrt{\frac{s}{a} \left(\frac{s}{at_1^2} + 1\right) + \frac{1}{4}t_1^2} + \frac{s}{at_1} - \frac{1}{2}t_1
 \end{aligned}$$

In Figure 2.9, a PiPiCo line is shown that was calculated using the above result.

Now follows the calculation of the slope of the coincidence line. This slope is usually a good method to identify certain specific details about the fragmenta-

tion process, such as the charge states of the involved ions. The procedure is to calculate the derivative of $t_2(t_1)$ with respect to t_1 and then evaluate it at $p_0 = 0$.

$$\begin{aligned}\frac{dt_2(t_1)}{dt_1} &= \frac{d}{dt_1} \left(\sqrt{\frac{s}{a} \left(\frac{s}{at_1^2} + 1 \right) + \frac{1}{4}t_1^2} \right) - \frac{s}{at_1^2} - \frac{1}{2} \\ &= \frac{1}{2} \left[\frac{s}{a} \left(\frac{s}{at_1^2} + 1 \right) + \frac{1}{4}t_1^2 \right]^{-\frac{1}{2}} \cdot \left(\frac{1}{2}t_1 - 2\frac{s^2}{a^2t_1^3} \right) - \frac{s}{at_1^2} - \frac{1}{2}\end{aligned}\quad (2.15)$$

From Equation (2.10) it is obtained that $p_0 = 0$ is equivalent to $t = \sqrt{2s/a}$, the standard TOF value with zero initial momentum. Evaluation of the above derivative at $t_1 = \sqrt{2s/a}$ gives

$$\begin{aligned}\left. \frac{dt_2(t_1)}{dt_1} \right|_{p_0=0} &= \frac{1}{2} \left[\frac{s}{a} \left(\frac{s}{a} \cdot \frac{a}{2s} + 1 \right) + \frac{1}{4} \cdot \frac{2s}{a} \right]^{-\frac{1}{2}} \left(\frac{1}{2} \cdot \sqrt{\frac{2s}{a}} - 2\frac{s^2}{a^2} \cdot \frac{1}{\frac{2s}{a} \cdot \sqrt{\frac{2s}{a}}} \right) \\ &\quad - \frac{s}{a} \cdot \frac{a}{2s} - \frac{1}{2} \\ &= \frac{1}{2} \left(\frac{3s}{2a} + \frac{s}{2a} \right)^{-\frac{1}{2}} \cdot \left(\frac{1}{2} \sqrt{\frac{2s}{a}} - \frac{s}{a} \cdot \sqrt{\frac{a}{2s}} \right) - 1 \\ &= \frac{1}{2} \sqrt{\frac{a}{2s}} \cdot \underbrace{\left(\sqrt{\frac{s}{2a}} - \sqrt{\frac{s}{2a}} \right)}_{=0} - 1 \\ &= -1\end{aligned}\quad (2.16)$$

This means that the slope of the PiPiCo line at its centre ($p_0 = 0$) is -1 . This result is only true for particles with equal mass $m_1 = m_2 = m$ and equal charge $q_1 = q_2 = q$. Even though the charge does not directly appear in the calculation, it influences the acceleration a fragment experiences in the electric field and, therefore, the relation between initial momentum and change in TOF value. The next subsection generalises the calculation to fragments with arbitrary masses and charges.

Fragments of different masses and different charges

Here the equations from the previous subsection are generalised to fragments with different masses and different charges. As will be seen, the fragments'

masses have, in contrast to their charges, no influence on the slope of the PiPiCo line.

First, the acceleration a charged particle experiences in the homogeneous electric field E of the spectrometer is

$$a = \frac{F_{\text{ef}}}{m} = E \frac{q}{m}. \quad (2.17)$$

Because of the different charge states, the acceleration that the two particles experience is now no longer identical. A ratio of accelerations can be written as

$$\frac{a_1}{a_2} = \frac{q_1}{q_2} \cdot \frac{m_2}{m_1}. \quad (2.18)$$

The equations for the TOF values of the two fragments are now

$$t_1 = \sqrt{\frac{2s}{a_1} + \left(\frac{p_0}{a_1 m_1}\right)^2} - \frac{p_0}{a_1 m_1}, \quad (2.19)$$

$$t_2 = \sqrt{\frac{2s}{a_2} + \left(\frac{p_0}{a_2 m_2}\right)^2} + \frac{p_0}{a_2 m_2}. \quad (2.20)$$

Substituting $p_0 = p_0(t_1)$ from Equation (2.13) gives t_2 depending on t_1 .

$$\begin{aligned} t_2(t_1) &= \sqrt{\frac{2s}{a_2} + \left(\frac{1}{a_2 m_2} \left(\frac{s m_1}{t_1} - \frac{1}{2} m_1 a_1 t_1\right)\right)^2} + \frac{1}{a_2 m_2} \left(\frac{s m_1}{t_1} - \frac{1}{2} m_1 a_1 t_1\right) \\ &= \sqrt{\frac{2s}{a_2} + \left(\frac{s}{t_1 a_2} \cdot \frac{m_1}{m_2} - \frac{1}{2} t_1 \frac{m_1}{m_2} \cdot \frac{a_1}{a_2}\right)^2} + \frac{s}{t_1 a_2} \cdot \frac{m_1}{m_2} - \frac{1}{2} t_1 \frac{m_1}{m_2} \cdot \frac{a_1}{a_2} \end{aligned} \quad (2.21)$$

Substituting the acceleration from Equation (2.17) and the acceleration ratio from and Equation (2.18) leads to

$$\begin{aligned} t_2(t_1) &= \sqrt{\frac{2s m_2}{E q_2} + \frac{s^2}{t_1^2 E^2} \left(\frac{m_1}{q_2}\right)^2 - \frac{s m_1 q_1}{E q_2^2} + \frac{t_1^2}{4} \left(\frac{q_1}{q_2}\right)^2} + \frac{s}{E t_1} \cdot \frac{m_1}{q_2} - \frac{1}{2} t_1 \frac{q_1}{q_2} \\ &= \frac{1}{q_2} \left[\sqrt{\frac{s}{E} \left(2 m_2 q_2 + \frac{s m_1^2}{t_1^2 E} - m_1 q_1\right)} + \frac{1}{4} t_1^2 q_1^2 + \frac{s}{E} \cdot \frac{m_1}{t_1} - \frac{1}{2} t_1 q_1 \right] \end{aligned} \quad (2.22)$$

Again the derivative of t_2 with respect to t_1 is taken.

$$\begin{aligned}
 \frac{dt_2(t_1)}{dt_1} &= \frac{1}{q_2} \left[\frac{d}{dt_1} \left(\sqrt{\frac{s}{E} \left(2m_2q_2 + \frac{sm_1^2}{t_1^2E} - m_1q_1 \right) + \frac{1}{4}t_1^2q_1^2} \right) - \frac{s}{E} \cdot \frac{m_1}{t_1^2} - \frac{1}{2}q_1 \right] \\
 &= \frac{1}{q_2} \left[\frac{1}{2} \left(\frac{s}{E} \left(2m_2q_2 + \frac{sm_1^2}{t_1^2E} - m_1q_1 \right) + \frac{1}{4}t_1^2q_1^2 \right)^{-\frac{1}{2}} \right. \\
 &\quad \left. \cdot \left(-2 \frac{s^2m_1^2}{E^2t_1^3} + \frac{1}{2}q_1^2t_1 \right) - \frac{s}{E} \cdot \frac{m_1}{t_1^2} - \frac{1}{2}q_1 \right]
 \end{aligned} \tag{2.23}$$

Now this derivative is evaluated at the value of t_1 that corresponds to $p_0 = 0$, which is

$$p_0 = 0 \quad \Rightarrow \quad t_1 = \sqrt{\frac{2s}{a_1}} = \sqrt{\frac{2sm_1}{Eq_1}} \tag{2.24}$$

Substituting this in Equation (2.23) gives the slope of the PiPiCo line at its centre:

$$\begin{aligned}
 \left. \frac{dt_2(t_1)}{dt_1} \right|_{p_0=0} &= \frac{1}{q_2} \left[\frac{1}{2} \left(\frac{s}{E} \left(2m_2q_2 + \frac{1}{2}m_1q_1 - m_1q_1 \right) + \frac{1}{2} \frac{sm_1q_1}{E} \right)^{-\frac{1}{2}} \right. \\
 &\quad \left. \cdot \left(-\frac{sm_1q_1}{E} \sqrt{\frac{Eq_1}{2sm_1}} + \frac{1}{2}q_1^2 \sqrt{\frac{2sm_1}{Eq_1}} \right) - q_1 \right] \\
 &= \frac{1}{q_2} \left[\frac{1}{2} \left(\frac{2sm_2q_2}{E} \right)^{-\frac{1}{2}} \cdot \underbrace{\left(-\sqrt{\frac{2m_1q_1^3}{2E}} + \sqrt{\frac{2m_1q_1^3}{2E}} \right)}_{=0} - q_1 \right] \\
 &= -\frac{q_1}{q_2}
 \end{aligned} \tag{2.25}$$

This means that the slope of the PiPiCo line at $p_0 = 0$ is equal to the negative ratio of the fragments' charges. It is independent of the fragments' masses. Note that reversing the numbering of the fragments will invert the slope but it will also exchange the labeling of the axes of the PiPiCo histogram (so far, t_1 was assumed to be on the horizontal axis).

2.5.2 TriPiCo lines

As with two-particle coincidences, coincidence histograms can be created for the coincident detection of three fragments, called TriPiCo ('Triple Photoion Coincidence'). The procedure is, however, somewhat more complex and requires a deeper understanding of the relation between initial momentum of a fragment and the change of its TOF value.

There are three different TriPiCo histograms. Each plots the sum of the TOF values of two particles against the TOF value of the third particle. Therefore, the three histograms are $t_2 + t_3$ against t_1 , $t_1 + t_3$ against t_2 , and $t_1 + t_2$ against t_3 . The case $t_2 + t_3$ against t_1 is examined in the following, but all conclusions apply to the other two variants as well.

In the example in Section 2.5.1, a laser pulse was considered to result in four detector hits with four distinct TOF values: t_1 , t_2 , t_3 and t_4 . While in the case of a PiPiCo histogram the TOF values were paired, as in (t_1, t_2) , (t_1, t_2) and so on, in a TriPiCo histogram uses three TOF values to create one entry in the two-dimensional histogram. In the example, the pairs would be $(t_1, t_2 + t_3)$, $(t_1, t_2 + t_4)$, $(t_1, t_3 + t_4)$ and $(t_2, t_3 + t_4)$. Assuming again that the four TOF values were 1, 2, 3 and 4, the resulting TriPiCo histogram has four entries as depicted in Figure 2.10.

The momentum carried by fragment 1 is equal to the negative sum of the momenta of fragments 2 and 3. This is true for the 3D momenta as well as for every momentum component separately. Here, as in the previous section, only the momentum in z -direction is described (z -direction is positive towards the detector), because it is the only momentum component that influences the TOF value.

$$p_1 = -(p_2 + p_3) \quad (2.26)$$

The share of the momentum between fragments 2 and 3 is not determined and is considered to be randomly distributed. It can be described by a parameter x that ranges from 0 to 1:

$$\begin{aligned} p_2 &= -xp_1 \\ p_3 &= -(1-x)p_1 \end{aligned} \quad (2.27)$$

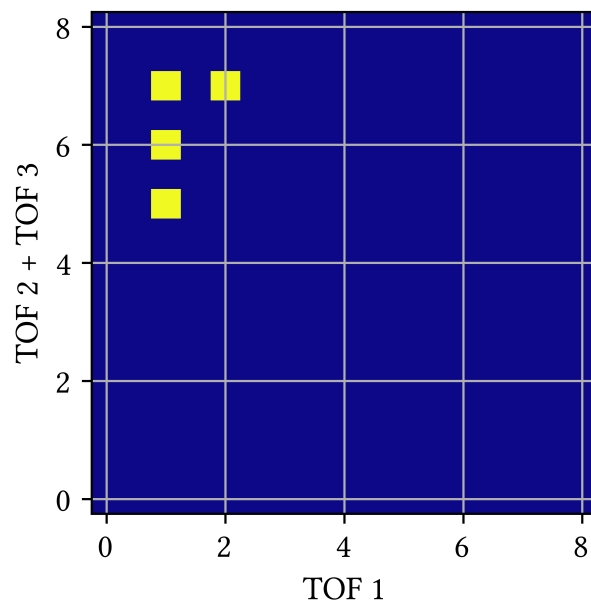


Figure 2.10: Example TriPiCo histogram created from a laser pulse with four detected particles at TOF values 1, 2, 3 and 4. The TOF value of the first detected fragment is on the x -axis. The entries of the histogram are (1, 2+3), (1, 2+4), (1, 3+4), and (2, 3+4).

Using the above description of p_2 and p_3 in Equation (2.10) gives the TOF values of fragments 2 and 3 depending on x and p_1 :

$$\begin{aligned}
 t_2 = t(-xp_1) &= \sqrt{\frac{2s}{a_2} + \left(\frac{-xp_1}{a_2 m_2}\right)^2} + \frac{xp_1}{a_2 m_2} \\
 t_3 = t(-(1-x)p_1) &= \sqrt{\frac{2s}{a_3} + \left(\frac{-(1-x)p_1}{a_3 m_3}\right)^2} + \frac{(1-x)p_1}{a_3 m_3}
 \end{aligned} \tag{2.28}$$

The sum of t_2 and t_3 is the value of the vertical axis in the considered TriPiCo histogram, with t_1 being the value on the horizontal axis. It computes to

$$\begin{aligned}
 t_{23} = t_2 + t_3 &= \sqrt{\frac{2s}{a_2} + x^2 \left(\frac{p_1}{a_2 m_2}\right)^2} + \sqrt{\frac{2s}{a_3} + (1-x)^2 \left(\frac{p_1}{a_3 m_3}\right)^2} \\
 &\quad + p_1 \left(\frac{x}{a_2 m_2} + \frac{1-x}{a_3 m_3}\right).
 \end{aligned} \tag{2.29}$$

This means that in a TriPiCo histogram the position of one entry is not only defined by p_1 but also by x representing the momentum share between two of the fragments.

In order to find an expression for the slope of the line in the TriPiCo histogram, t_{23} is written in terms of x and t_1 by substituting p_1 similarly as in Equation (2.13):

$$\begin{aligned}
 t_{23}(t_1) &= \sqrt{\frac{2s}{a_2} + x^2 \left(\frac{s m_1}{t_1 a_2 m_2} - \frac{1}{2} \frac{m_1 a_1}{m_2 a_2} t_1\right)^2} \\
 &\quad + \sqrt{\frac{2s}{a_3} + (1-x)^2 \left(\frac{s m_1}{t_1 a_3 m_3} - \frac{1}{2} \frac{m_1 a_1}{m_3 a_3} t_1\right)^2} \\
 &\quad + x \left(\frac{s}{t_1 a_2} \frac{m_1}{m_2} - \frac{t_1}{2} \frac{m_1 a_1}{m_2 a_2}\right) + (1-x) \left(\frac{s}{t_1 a_3} \frac{m_1}{m_3} - \frac{t_1}{2} \frac{m_1 a_1}{m_3 a_3}\right)
 \end{aligned} \tag{2.30}$$

Substituting $a_i = Eq_i/m_i$ simplifies this expression to

$$\begin{aligned}
 t_{23}(t_1) &= \frac{1}{q_2} \sqrt{\underbrace{\frac{2sm_2q_2}{E} + x^2 \left(\frac{sm_1}{t_1E} - \frac{t_1q_1}{2} \right)^2}_{=:Q_2}} \\
 &+ \frac{1}{q_3} \sqrt{\underbrace{\frac{2sm_3q_3}{E} + (1-x)^2 \left(\frac{sm_1}{t_1E} - \frac{t_1q_1}{2} \right)^2}_{=:Q_3}} \\
 &+ \underbrace{\left(\frac{sm_1}{t_1E} - \frac{t_1q_1}{2} \right) \left(\frac{x}{q_2} + \frac{1-x}{q_3} \right)}_{=:A} \\
 &= \frac{1}{q_2} \sqrt{Q_2} + \frac{1}{q_3} \sqrt{Q_3} + A
 \end{aligned} \tag{2.31}$$

As in the previous section, evaluating the derivative at $t_1(p_0 = 0) = \sqrt{2sm_1/Eq_1}$ yields the slope of the TriPiCo line, in this case depending on the momentum share parameter x .

$$\begin{aligned}
 \frac{dt_{23}(t_1)}{dt_1} &= \frac{1}{q_2} \frac{d\sqrt{Q_2}}{dt_1} + \frac{1}{q_3} \frac{d\sqrt{Q_3}}{dt_1} + \frac{dA}{dt_1} \\
 &= \frac{1}{q_2} \frac{1}{2} Q_2^{-\frac{1}{2}} \frac{dQ_2}{dt_1} + \frac{1}{q_3} \frac{1}{2} Q_3^{-\frac{1}{2}} \frac{dQ_3}{dt_1} + \frac{dA}{dt_1} \\
 &= \frac{1}{2} \underbrace{\left(\frac{1}{q_2} x^2 Q_2^{-\frac{1}{2}} + \frac{1}{q_3} (1-x)^2 Q_3^{-\frac{1}{2}} \right)}_{=:Q} \left(\frac{t_1q_1^2}{2} - \frac{2s^2m_1^2}{E^2t_1^3} \right) \\
 &\quad - \underbrace{\left(\frac{sm_1}{t_1^2E} + \frac{q_1}{2} \right) \left(\frac{x}{q_2} + \frac{1-x}{q_3} \right)}_{=:B}
 \end{aligned} \tag{2.32}$$

$$\begin{aligned}
 \left. \frac{dt_{23}(t_1)}{dt_1} \right|_{p_1=0} &= Q \left(\frac{q_1^2}{2} \sqrt{\frac{2sm_1}{Eq_1}} - \frac{sm_1q_1}{E} \sqrt{\frac{Eq_1}{2sm_1}} \right) - B \\
 &= Q \left(\underbrace{\sqrt{\frac{sm_1q_1^3}{2E}} - \sqrt{\frac{sm_1q_1^3}{2E}}}_{=0} \right) - B \\
 &= -B = - \left(\frac{sm_1}{E} \frac{Eq_1}{2sm_1} \right) \left(\frac{x}{q_2} + \frac{1-x}{q_3} \right) \\
 &= -q_1 \left(\frac{x}{q_2} + \frac{1-x}{q_3} \right)
 \end{aligned} \tag{2.33}$$

This means that the slope at the centre of a TriPiCo line depends only on the charges of the three fragments and on the momentum share parameter x . For the example of all fragments having equal charge ($q_1 = q_2 = q_3$) the slope is -1 .

Because the indices 1, 2 and 3 are interchangeable, the respective slopes for the other two TriPiCo histograms are

$$-q_2 \left(\frac{x}{q_1} + \frac{1-x}{q_3} \right) \quad \text{for } t_1 + t_3 \text{ against } t_2 \tag{2.34}$$

and

$$-q_3 \left(\frac{x}{q_1} + \frac{1-x}{q_2} \right) \quad \text{for } t_1 + t_2 \text{ against } t_3. \tag{2.35}$$

2.5.3 Charge-scaling of flight times

It can be shown experimentally (or with simulated data) that the curves found in TriPiCo histograms emerge more clearly when the TOF values of the fragments are scaled by their respective charge state. Often the curves only become visible at all if charge-scaling is applied. This section explains why this is the case.

The flight times of the three fragments originating from a three-body fragmentation can be expressed as follows (see Equations (2.10) and (2.28)):

$$\begin{aligned}
 t_1 &= \sqrt{\frac{2s}{a_1} + \left(\frac{p_1}{a_1 m_1}\right)^2} - \frac{p_1}{a_1 m_1} \\
 t_2 &= \sqrt{\frac{2s}{a_2} + \left(\frac{-x p_1}{a_2 m_2}\right)^2} + \frac{x p_1}{a_2 m_2} \\
 t_3 &= \sqrt{\frac{2s}{a_3} + \left(\frac{-(1-x)p_1}{a_3 m_3}\right)^2} + \frac{(1-x)p_1}{a_3 m_3}
 \end{aligned} \tag{2.36}$$

These equations assume a constant acceleration caused by an electric field parallel to the detector normal. Fragment 1 carries the initial z -momentum p_1 . This means that the added initial z -momenta of ion 2 and ion 3 must be $-p_1$ because of momentum conservation. How $-p_1$ is shared between the second and third ion is determined by the momentum share parameter x .

Because the connection between an ion's TOF value and its initial momentum is non-linear, a change in initial momentum (either by varying p_1 or by varying x) does not lead to a proportional change in flight time. Another way to express this is to say the derivations of t_i by p_i (i being 1, 2, 3; $p_2 = -x p_1$ and $p_3 = -(1-x)p_1$) are not constant with p_i . The non-constant change in flight time by initial momentum is, as was described in Section 2.5.1, the reason why the PiPiCo lines are not actually lines but curves; the sum of the two TOF values is not constant but depends on the ions' initial momentum.

Even for a fixed value of p_1 , the varying momentum share between ion 2 and 3 changes their respective TOF values in a non-linear way such that the sum of t_2 and t_3 is not constant for varying x . While PiPiCo lines are, in principle, ideal sharp curves without width, TriPiCo lines possess an intrinsic width that cannot be reduced below a certain threshold, at least in the general case.

In Figure 2.11 a TriPiCo line is shown that was calculated for three particles with equal masses (16 u) and charges (1 e). Even though the sum of the TOF values of particles 2 and 3 does not vary much with their respective momentum share, the line exhibits a significantly larger width compared to the calculated PiPiCo line in Figure 2.9, especially towards its ends where the initial momentum in z -direction is largest.

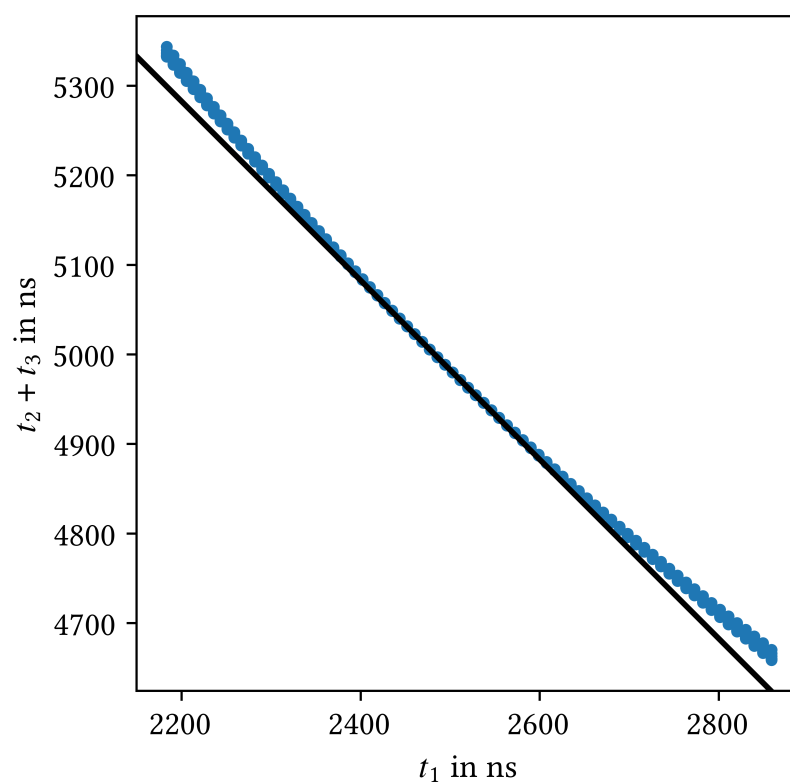


Figure 2.11: TriPiCo plot calculated for the dissociation of an ozone molecule (O_3) into three O^+ ions with a hypothetical KER of 10 eV. The larger width towards the ends of the line shows that the sum of TOF values 2 and 3 varies with their respective momentum share parameter x . The slope of the straight line is -1 .

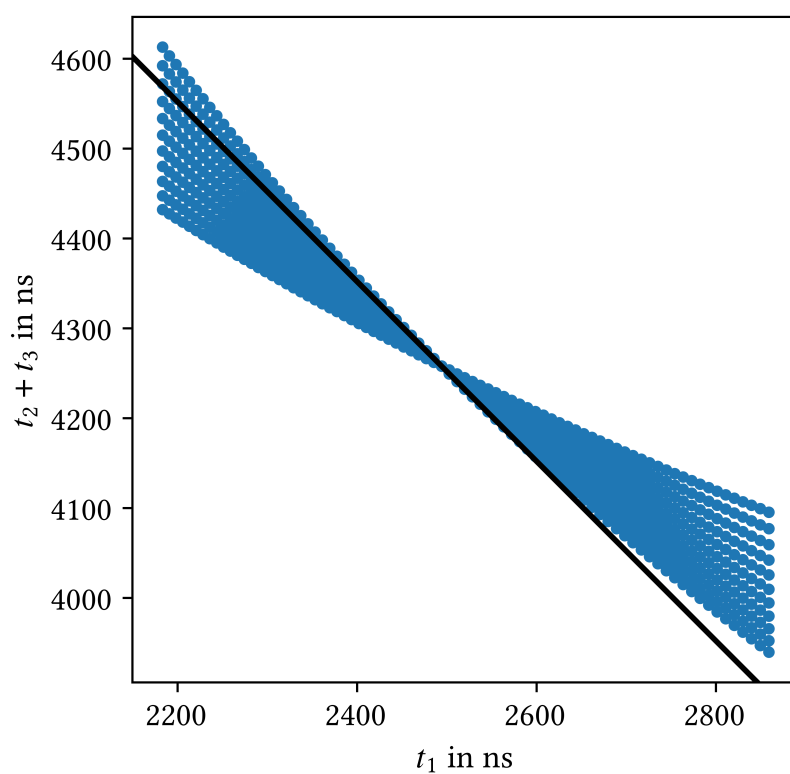


Figure 2.12: TriPiCo plot calculated again for the dissociation of an O_3 molecule into three fragments with a KER of 10 eV, but this time ions 1 and 3 are singly charged while ion 2 is doubly charged. The sum of the TOF values of ions 2 and 3 (that have different charge states) is now spread out over a much larger area of the plot which, when evaluating experimental data, can make it difficult to detect the line in the background noise.

The amount of variation in the sum of the TOF values of ions 2 and 3 for different values of x determines the intrinsic width of the TriPiCo curve. To quantify this variation in flight time sum, one can calculate the derivative of $t_{23} = t_2 + t_3$ by x :

$$\frac{dt_{23}}{dx} = \frac{dt_2}{dx} + \frac{dt_3}{dx} \quad (2.37)$$

The individual ions' TOF values derived by x are:

$$\begin{aligned} \frac{dt_2}{dx} &= \frac{p_1}{a_2 m_2} + x \frac{p_1^2}{a_2^2 m_2^2} \left(\frac{2s}{a_2} + \left(\frac{-x p_1}{a_2 m_2} \right)^2 \right)^{-\frac{1}{2}} \\ \frac{dt_3}{dx} &= -\frac{p_1}{a_3 m_3} - (1-x) \frac{p_1^2}{a_3^2 m_3^2} \left(\frac{2s}{a_3} + \left(\frac{-(1-x)p_1}{a_3 m_3} \right)^2 \right)^{-\frac{1}{2}} \end{aligned} \quad (2.38)$$

The second term is much smaller than the first term, so it can be neglected (for proof, see Appendix B). It follows that the derivation of the flight time sum t_{23} by the momentum share parameter x is approximately

$$\frac{dt_{23}}{dx} = \frac{p_1}{a_2 m_2} - \frac{p_1}{a_3 m_3} = \frac{p_1}{E} \left(\frac{1}{q_2} - \frac{1}{q_3} \right) \quad (2.39)$$

which depends on the charge states of the ions 2 and 3. For equal charge states, $q_2 = q_3$, the derivative vanishes. That means charge-scaling has no effect on TriPiCo histograms when the flight times of equally charged ions are added (as is the case in Figure 2.11). For non-equally charged ions the derivative is not zero and the flight time sum will vary significantly more with the momentum share between the ions 2 and 3. This case is shown in Figure 2.12 where the second particle is doubly charged while the other two remain singly charged. The TOF sum of particles 2 and 3 now varies much more with respect to the momentum share parameter x . In measurement data, the result is an increased width of the TriPiCo line, most of the times to a degree that they vanish in the background noise.

Charge-scaling overcomes this broadening by multiplying the individual flight times of the ions by a factor equal to the charge state of the ion. Charge state means the total charge q of the ion divided by the elementary charge e , such that $q = n \cdot e$ where n is the charge state.

The charge-scaled flight time sum of the ions 2 and 3 is then

$$t_{23,s} = n_2 t_2 + n_3 t_3. \quad (2.40)$$

The derivative of $t_{23,s}$ is then not only independent of the ions' respective charge state, it vanishes:

$$\begin{aligned} \frac{dt_{23,s}}{dx} &= n_2 \frac{dt_2}{dx} + n_3 \frac{dt_3}{dx} = n_2 \frac{p_1}{a_2 m_2} - n_3 \frac{p_1}{a_3 m_3} \\ &= \frac{p_1}{E} \left(\frac{n_2}{n_2 e} - \frac{n_3}{n_3 e} \right) = 0 \end{aligned} \quad (2.41)$$

This means that the scaled flight time sum does, in approximation, no longer vary with x . Therefore, plotting scaled flight time sums in the TriPiCo histograms leads to a decreased width of the TriPiCo curves and makes them more easily detectable than in the unscaled case. This is a helpful tool when searching for coincidence lines originating from three-ion dissociations. The effect of charge scaling is illustrated in Figure 2.13 on the example of the three-ion fragmentation of CH_2I_2 into $\text{CH}_2^+ + \text{I}^{++} + \text{I}^+$.

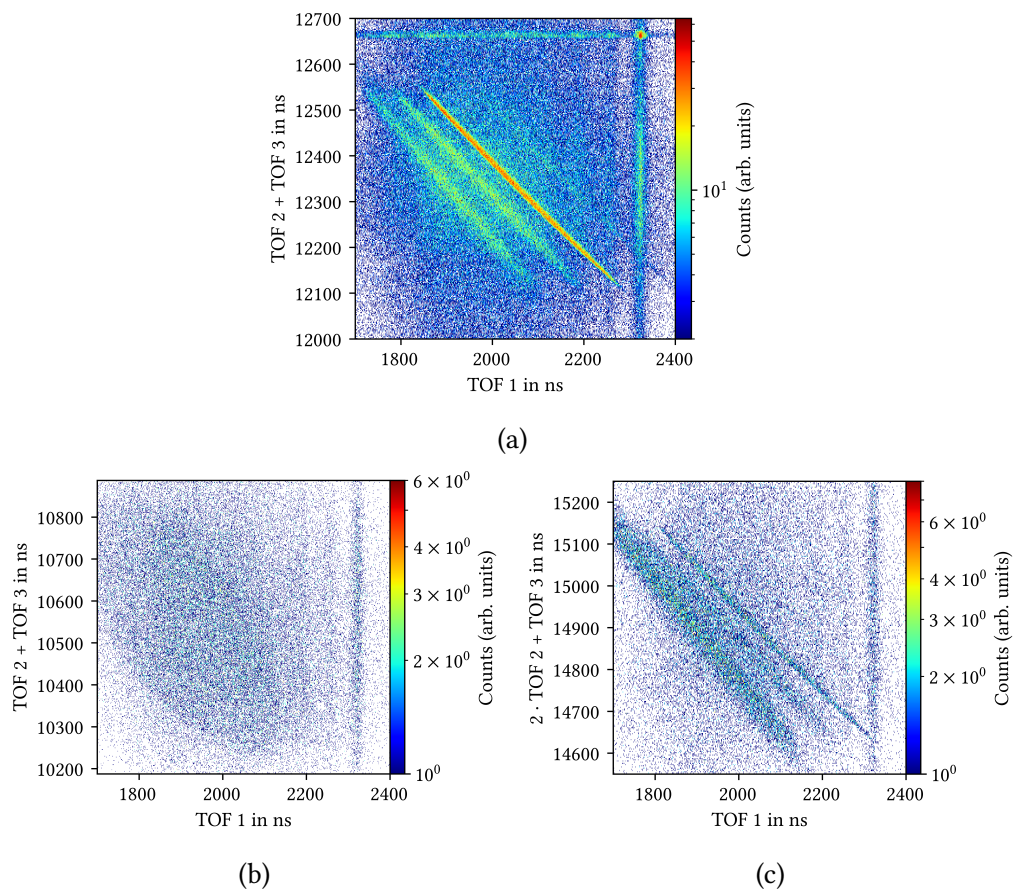


Figure 2.13: Illustration of the effect of charge-scaling TOF values for TriPiCo plots. In every histogram, the TOF of the CH_2^+ fragment is shown on the x -axis. (a): The $\text{CH}_2^+ + \text{I}^+ + \text{I}^+$ coincidence does not require charge-scaling because all ions have equal charge; (b): The non-charge-scaled TriPiCo histogram of $\text{CH}_2^+ + \text{I}^{++} + \text{I}^+$ does not show any coincidence line; (c): When charge-scaling is applied, the coincidence line of $\text{CH}_2^+ + \text{I}^{++} + \text{I}^+$ becomes visible.

Chapter 3

Experimental Setup

This chapter gives a general overview of the experimental setup used for the measurements of this work followed by a more detailed description of each subsystem. The basic functions and purpose of each part will be explained as well as the underlying physical principles of its operation. With the exception of Section 3.5, information will be given only on the parts of the measurement system that were used for obtaining and are necessary to understand the data presented in this work. Most of the content of this chapter is a synthesis of publications from the same group that were conducted on the same or a very similar setup such as [56, 60], and, focusing on the technical specifications of the system, [57].

The experimental setup used for conducting the measurements presented in this work is a permanent user endstation at the free-electron laser FLASH2, at DESY, Hamburg [1, 13]. It was built and commissioned by the research group of Dr. Robert Moshhammer at the Max Planck Institute for Nuclear Physics (MPIK). Its main sections are a reaction microscope (REMI), an in-line split-and-delay mirror stage and a supersonic jet target delivery system. The XUV laser pulses are generated by FLASH2.

The free-electron laser delivers the XUV pulses into the experimental hall. In the DESY-segment of the vacuum system, diagnostics provide information on the beam properties and positioning as well as mirrors with actuators to adjust the beam position and pointing. Then the XUV beam is passed into the user section of the vacuum setup. The FEL pulses pass, in this order, through a beam-line segment with filters, screens, and apertures, then through the XUV mirror chamber where they are split, delayed, and focused, into the REMI and, finally, into the FEL beam dump.

The MPIK beamline segment provides, in addition to the beam characterisation by DESY, apertures for beam size adjustment and screens for beam monitoring. In the mirror chamber, the FEL beam is split into an upper and a lower half, one of the halves is delayed with respect to the other, and both are focused into the REMI where they interact with the target. Both beam parts exit the REMI into an FEL beam dump to minimise back-reflection of stray XUV photons into the REMI. The supersonic target jet crosses the REMI main chamber at approximately 90° angle with respect to the FEL in such a way that the XUV focus is inside the jet volume. The jet exits the REMI into a two-stage jet dump to avoid contamination of the main chamber vacuum by diffused jet particles. In the following sections, each of these parts is explained in more detail.

3.1 XUV beamline and mirror chamber

The MPIK beamline upstream, with respect to the FEL, of the mirror chamber serves two different purposes: It houses adjustment and diagnostics equipment for the FEL beam and it serves as a differential pressure stage between the FLASH2 beamline and the mirror chamber. The pressure in the reaction microscope and, therefore, in the adjacent vacuum compartments, must be as low as possible to reduce ion and electron hits on the detectors from background gas ionisation. The REMI main chamber has a pressure of low 10^{-11} mbar while the DESY beamline usually has a few orders of magnitude higher pressure. The vacuum segment between the DESY beamline and the XUV mirror chamber mediates this pressure gradient with a series of differential pressure stages.

There are two arrays of apertures in this vacuum segment. Each array houses several differently sized circular apertures coated with fluorescent powder to make the FEL radiation visible to the human eye and optical cameras. By raising or lowering the arrays one can switch between different aperture diameters and, therefore, beam diameters. By changing the aperture position just slightly, the FEL beam position in the beamline can be adjusted in height or moved left and right. A fluorescent Ce:YAG screen is mounted downstream of the second aperture array just before the mirror chamber. The screen can be lowered into the beam path with a pneumatic actuator. In between the apertures there is a pair of beam blocks mounted to manual rotational actuators. The lower one can raise a metal plate from below into the FEL path, the upper one can lower a different plate from above. This arrangement is used to block the lower or upper part of the FEL which corresponds to blocking the delayed or the non-delayed beam half independently.

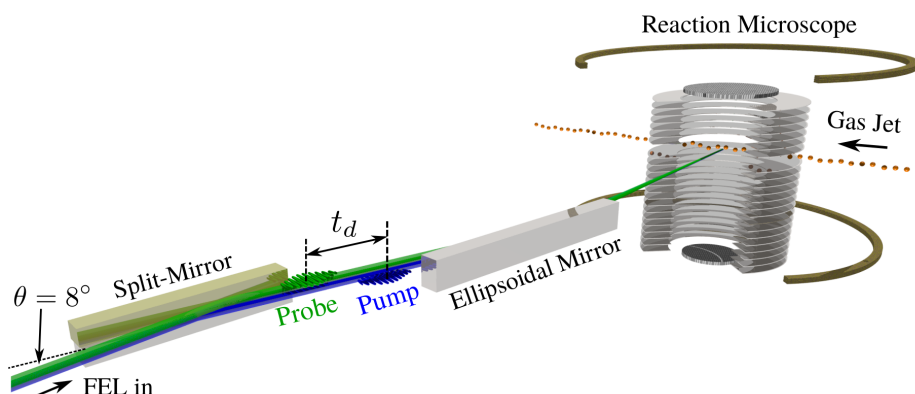


Figure 3.1: Schematic of the XUV split-delay-focusing optics. Figure from [56].

The next section the FEL beam enters is the XUV mirror chamber. There it is reflected on each of the two grazing incidence XUV mirrors (see Figure 3.1). The reflection angle is 8° . To avoid a permanent change of direction of the FEL path, the first mirror reflects the FEL to the right, the second one to the left again, resulting in a parallel displacement of the FEL path. The first mirror is the split-and-delay mirror, the second is the focusing mirror.

The split-and-delay mirror is an assembly of two plane mirrors, an upper and a lower one (see Figure 3.2). They are separated along a horizontal line. The lower mirror is fixed to the mirror mount, the upper mirror can be moved relative to the lower mirror. This movement is made possible by three stick-slip piezo actuators [57]. They allow for rotation along two different axes as well as for linear displacement of the mirror. The displacement creates a path length difference between the upper and lower parts of the FEL beam. This results in a time delay between the two pulses with regard to their arrival in the focus region. The rotational movement of the movable mirror is used for overlapping the two pulses in the focus plane. The necessary rotational corrections depend on the adjusted delay value.

The focusing mirror is an off-axis ellipsoid, meaning it has a curvature in both horizontal and vertical direction. It therefore has the advantage of focusing the incoming FEL pulses into a the interaction region with a single reflection. The ellipsoidal mirror is designed to focus light coming from one point into another point. Its source point is 85 metres away (inside the undulator region of the FEL) while its focus distance is one metre (the interaction region in the target jet). Even though being very close to one of the poles of the rotational ellipsoid that

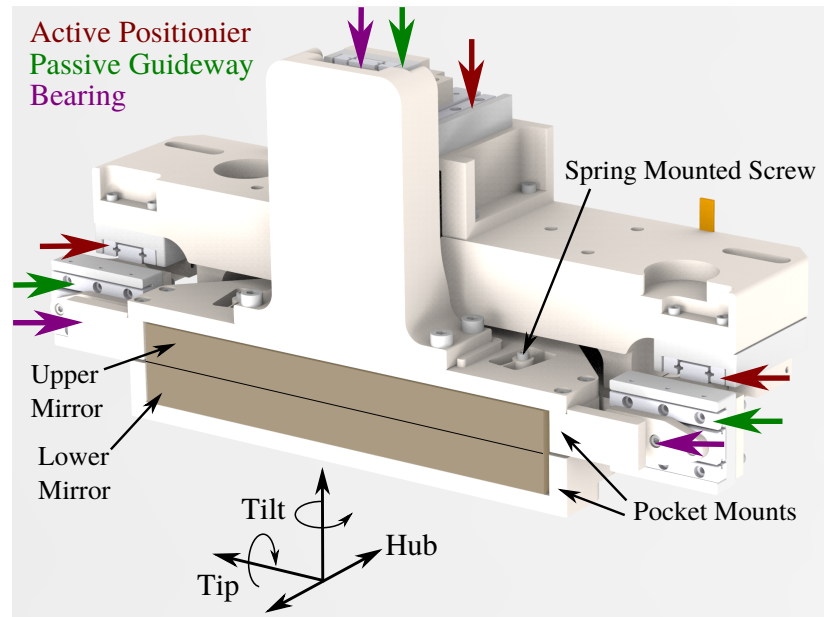


Figure 3.2: Schematic of the split-and-delay mirror. Figure from [56].

characterises its reflective surface, the focusing mirror has no visible asymmetry. However, it definitely has an asymmetry, which was discovered when the mirror was oriented in the wrong way during its first installation. This resulted in large focus distortions visible with the wavefront sensor that was used for mirror commissioning. Installed in the correct orientation, the ellipsoidal mirror focuses the incoming FEL pulses into a spot of approximately $3\ \mu\text{m}$ in diameter [57].

Each of the mirrors is suspended from the top of the mirror chamber by a hexapod support structure. Each hexapod has six linear step motors attached to it. With them it is possible to move each mirror linearly in three-dimensional space as well as rotate it along all three axes independently. This is necessary to optimise the focus properties. During normal operation of the endstation the hexapods are usually not moved because the position and orientation for optimal focus properties have been found to be constant over time. One exception is moving the split-and-delay mirror up and down to adjust the portions of the FEL on the two respective mirror parts. In this way it is possible to change the ratio of energy between the fixed and the delayed pulse.

The mirrors themselves are made of monocrystalline silicon substrate. The reflective coating is a 30 nm thick layer of carbon. The mirror reflectivity under 8° of incidence angle is displayed in Figure 3.3.

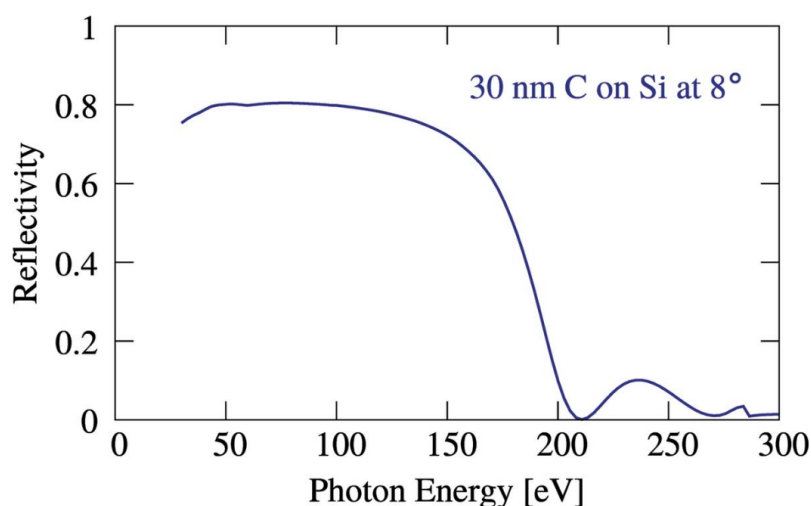


Figure 3.3: Reflectivity of a 30 nm carbon layer on monocrystalline silicon under 8° incidence angle for various photon energies. Figure from [56].

The FEL intensity in the focus can be estimated from the focus size, the pulse duration and the pulse energy. At the photon energy of 97.6 eV, the mirror reflectivity is approximately 80 %. Therefore, the pulse energy of approximately $60 \mu\text{J}$ measured by DESY will be reduced to $0.8^2 \cdot 60 \mu\text{J} = 38.4 \mu\text{J}$ after reflection on both mirrors. Focused into a circular area of $3 \mu\text{m}$ diameter with a pulse duration of approximately 50 fs, this results in a focus intensity of approximately $3 \times 10^{15} \text{ W cm}^{-2}$.

3.2 Reaction Microscope

A reaction microscope is a versatile instrument for investigating atomic dissociation processes [40]. It enables the detection of time and position information of all particles that originate from dissociation events, such as photoionisation or molecular fragmentation. From the measured information, the particles' initial momenta can be calculated and a kinematically complete reconstruction of the observed process is possible.

To achieve this, a reaction microscope applies homogeneous parallel electric and magnetic fields in a spectrometer. The ions and electrons created by the dissociation event are affected by the fields and move towards their respective detect-

ors at opposite ends of the spectrometer. There, the time of flight and the two-dimensional position on the detector is measured for each particle. The magnetic field is necessary because the kinetic energy of electrons from dissociation events can be much higher than for ions. If electrons start with much higher kinetic energy and enough momentum transversal to the electric field, they can miss the detector. The Lorentz force of the magnetic field forces the electrons on spiral trajectories. This increases the upper limit for detectable electron energies. In this work, no electron measurements are presented, which is why the focus lies on the detection method of ionic dissociation products.

The reaction microscope at FLASH2 is installed vertically such that the detectors are on the upper and lower end of a cylindrical vacuum chamber. The spectrometer consists of a stack of metal rings and the electric field is created by applying voltage to these spectrometer rings. Two copper coils in Helmholtz configuration are installed outside of the REMI vacuum chamber to create the magnetic field.

In the following, the separate parts of the spectrometer and the detectors are explained in more detail.

3.2.1 The Spectrometer

The spectrometer creates the conditions that guide the charged particles from the interaction region to the detectors where their time-of-flight (TOF) and position information is measured. In Figure 3.4 a schematic of the spectrometer is shown.

A homogeneous and constant electric field is created in the focus interaction region and between the ion and electron detectors. The ions are therefore affected by a constant acceleration from the moment they are created until the end of the spectrometer.

The spectrometer consists of a cylindrical stack of steel rings that are electrically connected. A voltage can be applied to the rings such that they create the homogeneous electric field in the inner cylindrical volume. At both ends of the spectrometer, before the detectors, there are metal grids in order to provide a smooth termination of the constant electric field region. The distance from the interaction region to the grid on the ion side of the spectrometer is shorter (approximately 94.5 mm) than the distance on the electron side (approximately 180.5 mm). A picture of the spectrometer including the ion detector can be seen in Figure 3.5.



Figure 3.5: Photo of the spectrometer in the FLASH2 hall, shortly before installation in the REMI on 21. September 2017.

Due to their much smaller mass, electrons have a higher kinetic energy than ions at equal momentum. For example, photoelectrons leave the interaction region at a much higher velocity than the corresponding photoions. An electric field that is well-adjusted for measuring slow ions would let most high-energy electrons escape the spectrometer sideways before they could reach the detector. Therefore, a homogeneous and constant magnetic field is applied parallel to the electric field. It forces the electrons on cyclotron trajectories while keeping their TOF values unchanged due to the Lorentz force perpendicular to the electrons' velocity. The position information of the much heavier ions is not significantly affected by the magnetic field. In this way, with appropriately adjusted electric and magnetic fields, it is possible to detect all ions and electrons created in the interaction region with 4π acceptance. The data presented in this work was recorded at 7500 V/m. Typical values for the magnetic field are on the order of 10 Gauss [57].

It is an idealised assumption that the electric field is homogeneous and constant for the entire path of the ions from the interaction region to the detector. This assumption is sufficient for a general understanding of the measurement principle. However, for transforming the measured TOF values into initial ion momenta, a calibration is needed that asks for a more detailed description of the spectrometer properties. Between the end of the spectrometer space and the MCP detector two grids are installed. Those are metal meshes with different voltages applied to them. The first grid encountered by the ions, as mentioned above, has the purpose to smoothly terminate the electric field of the spectrometer. Its potential is therefore adjusted to be slightly higher than that of the ion side of the spectrometer. The second grid has a much higher potential and serves to accelerate the ions to increase the detection efficiency of the following MCP detector. As a result, the ions actually experience different accelerations when passing through the stages between the spectrometer and the detector. As described in detail in Chapter 4, the time the ions spend between the end of the spectrometer and the MCP is proportional to the square of their mass-to-charge ratio and can be treated as a ion-species-specific time offset. The method of detecting ions and electrons and the principles of extracting time and position information is explained in the next section.

3.2.2 MCP detectors: measuring time

The particle detectors used in the REMI are microchannel plates (MCPs) [66]. They are thin plates with two-dimensional arrays of independently-working microscopic electron multiplier tubes. The ion detector consists of a stack of two

MCPs in chevron arrangement. Its sensitive area is circular with a diameter of 120 mm. The electron detector has three MCPs in Z-arrangement with a circular detection area of 80 mm in diameter.

A voltage of around 3 kV is applied between the front and back side of the MCPs. When a particle hits the wall of one of its channels, secondary emission of electrons causes a charge avalanche progressing along the respective channel. The initial charge of the particle is amplified such that a cloud of electrons leaves the MCP on the back side. The occurrence of a charge avalanche can be recorded as a drop in the voltage applied to the MCPs. This is the signal used to detect particle impacts. In addition, the voltage drop at the MCP is used to provide timing information on the arrival of a particle. The TOF of the particles is measured in reference to the trigger of the light source.

The dead time of the MCP detectors is approximately 10 ns which limits the time frame for measuring particles in coincidence. For example, two identical ions with the same initial momentum along the spectrometer axis cannot both be detected in coincidence.

The detection efficiency p_{det} of an MCP depends on the energy of an ion and on the MCPs active surface area. Ions that do not hit one of the microscopic channels, but the surface in between the channels, are not detected, so the layout of the channels on the MCP directly influences the detection efficiency. Ions of higher energy are more likely to cause a charge avalanche in the MCP. Therefore, the ions coming from the spectrometer are post-accelerated by a metal grid in front of the MCP surface to energies above 1 kV. Optimising the detection efficiency is especially important for coincidence measurements. The detection of each particle is an event independent of the detection of any other particle. Therefore, the probability p_{tot} to detect n ions from a specific dissociation event decreases exponentially with n : $p_{\text{tot}} = p_{\text{det}}^n$.

Because the channels of an MCP work independently, they can be used to obtain position information as well. The charge avalanche created by the detection of a single particle results in an electron cloud leaving the back side of the MCP at the location of the channel where the particle was detected. With a subsequent detector, the position of this channel can be measured. In the setup used for this work, a delayline anode provides the position information. Its functionality will be explained in the next section.

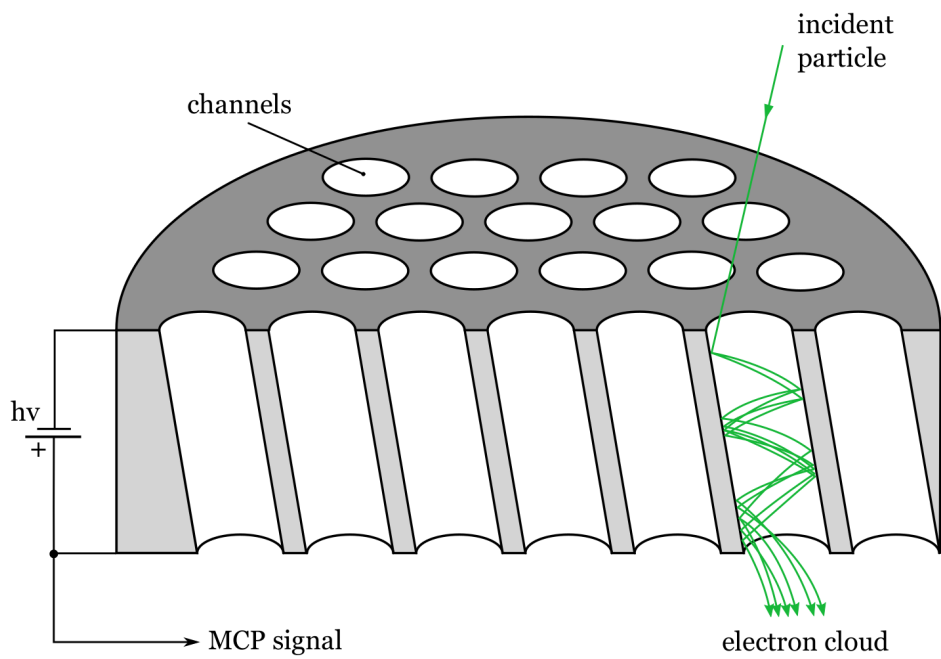


Figure 3.6: Schematic of an MCP with a charge avalanche created by an incident particle. The measured voltage drop indicates the detection of the particle and provides timing information. Figure taken from [46].

3.2.3 Delaylines: measuring position

To obtain information on where a particle has impacted on the MCP, a delayline anode detector installed directly behind the MCP is used. A delayline anode consists of a thin wire that is coiled around a rectangular support frame as shown in Figure 3.7. The wire is kept at a potential higher than the back side of the MCP such that the electron cloud expelled from the MCP is attracted to the wire. Upon impact it creates a voltage spike that propagates along the wire in both directions. At both end of the wire the arrival time of the voltage spike is measured. From the difference between the two arrival times it can be calculated where along the wire the charge cloud impacted. For two-dimensional position information, a second delayline anode is needed. In the ion detector used for this work, two delayline anodes with perpendicular wires are used to measure x and y position information.

The sum of the two arrival times is always equal (determined by the total length of the wire), which is why the delayline anode detector is capable of multi-hit detection. The delaylines used in this work can detect two separate particles that arrive in a time frame as short as 8 ns [60].

The electron detector features a set of three independent delayline anodes, each rotated 120° with respect to the others, which is called a hexanode configuration. Using three layers increases the multi-hit capability of the detector because the complete two-dimensional position information can be obtained from any set of two of the three delayline anodes.

3.3 Target Delivery System

In order for the FEL pulses to interact with the target particles, those particles must be delivered to the focus region. Ideally, this is done without contaminating the vacuum in the spectrometer region and with a low velocity distribution of the target particles to allow for high momentum resolution. In addition, the sample must be delivered with appropriate particle density in the FEL focus region such that each FEL pulse has a significant probability to introduce a dissociation event. All this is achieved by creating a collimated supersonic gas jet composed of the target particles. This jet enters and exits the REMI main chamber through differential pumping stages which keep contamination of the ultra-high vacuum region to a minimum. Due to its creation in a supersonic expansion zone, the particles in the jet have very low relative momenta, making it effectively a cold (typically <20 K) and dilute ($\leq 10^{10}$ particles per cm^3) target [57].



Figure 3.7: Photo of the delayline detector of the ion side of the spectrometer, shortly before installation in the REMI on 21. September 2017.

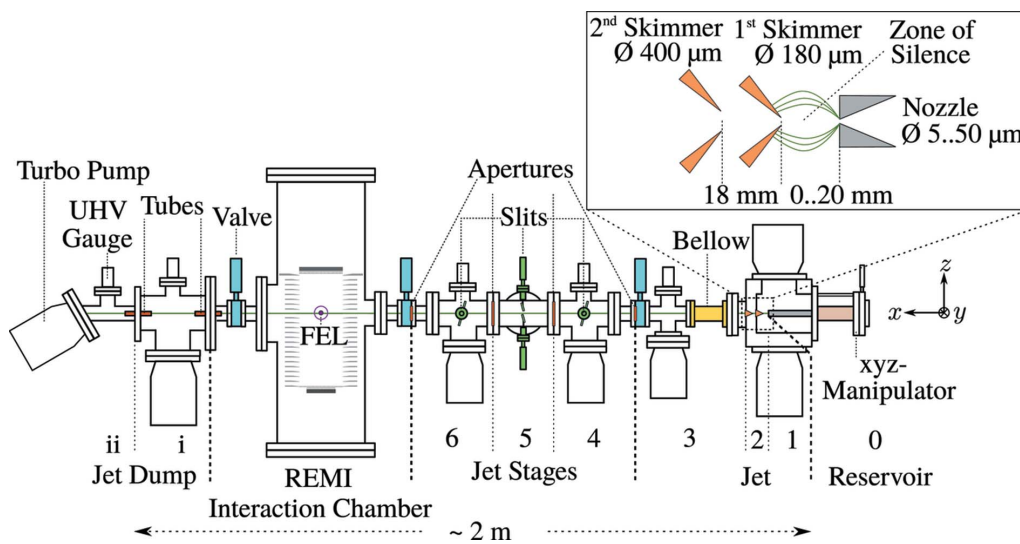


Figure 3.8: Schematic of the target delivery system. Figure from [57].

In order to create such a jet, the target gas is expanded into vacuum through a micrometre-size nozzle with a high backing pressure. [56] gives a more detailed description of the supersonic expansion process. The thermodynamic properties of such an expansion transform most of the gas particles' thermal energy into directional kinetic energy, effectively cooling and accelerating the gas. The result is a beam of gas particles with very low relative momenta, all travelling in the same direction at supersonic speed (several 100 m s^{-1} , depending on the specific target substance). The jet then passes through a set of conical copper skimmers and several apertures which act as differential pumping stages before it enters the main chamber. The spatial extension of the jet can be changed by three pairs of slits that can be moved in and out of the jet path to cut parts of it away. When exiting the main chamber, the jet passes through two tubes which again act as differential pumping stages before it impacts on the blades of a turbomolecular pump and is pumped away.

Because the supersonic expansion is creating a cool environment for the gas particles, they more easily form clusters such as dimers, trimers and larger clusters. For example, noble gas dimers [59, 61] and water dimers (publication pending) have been created in supersonic jet expansions and investigated in REMIs. This method of target delivery is therefore especially useful for the investigation of dynamics in particle clusters.

The supersonic jet expansion does in principle only work with gaseous targets. However, liquid and solid substances with a high partial pressure can create a sufficient backing pressure to undergo the same supersonic expansion and jet formation. Heating the target samples and using a carrier gas such as helium can help in the process. The target substance CH_2I_2 used in this work is liquid at standard temperature and pressure. It was deposited in a metal container ('bubbler') which was heated to increase its vapour pressure. In addition, helium was used as a carrier gas for the much heavier CH_2I_2 molecules.

For substances without sufficient partial pressure, a different target delivery method must be used. For example, in a measurement in 2019, C_{60} fullerene molecules were investigated. C_{60} is a solid that evaporates at several hundred degrees of temperature. An oven was constructed and tested which can heat and evaporate the C_{60} . It left the nozzle of the oven as a diffuse stream of gas instead of a supersonic jet. The target density in the focus was sufficient to investigate the C_{60} molecules with an XUV pump-probe measurement (publication pending).

3.4 Data Acquisition

When particles impact on the MCPs and delaylines, they create voltage signals in the detector output cables. Assigning timing information to these signals is the first step of data processing. These voltage signals can be interpreted into time-of-flight and position information from which particle momenta can be calculated (see Chapter 4 for details).

The REMI data acquisition system uses Acqiris DC282 digitiser cards for signal recording. When a voltage signal in a detector output cable passes an adjustable noise threshold, the entire voltage trace is recorded and stored. This is done for all channels in parallel (five for the ion detector, seven for the electron detector, one for the delay signal and one for the FEL intensity signal). The digitiser cards can sample the voltage traces at a maximum rate of 2 GHz in a range of ± 5 V [60].

FLASH2 delivers pulse trains with 10 Hz repetition rate. The pulses in each train arrive with 200 MHz repetition rate, so they have 5 μ s temporal distance. Reading out the digitiser cards' memory takes more than 5 μ s, so the voltage traces for all FEL pulses in a pulse train are stored on the digitiser cards. The read-out process is initiated by the FLASH2 trigger in between the pulse trains at 10 Hz rate.

Peak identification and assignment of time information is the first step of the offline analysis which is described in Chapter 4.

3.5 Subsequent Updates of the Setup

Since the measurements for this work were conducted, several additions were made to the REMI endstation at FLASH2.

An optical laser operated by DESY can be coupled into the beam line collinearly to the FEL [29]. This provides the capability for FEL-IR pump-probe experiments [36, 37]. Additionally, the optical laser can be used in a high-harmonic generation (HHG) setup to create HHG-XUV pulses. This further extends the measurement capabilities to two-colour XUV-XUV pump-probe experiments [4].

In 2021, a second experimental setup was placed downstream of the REMI in an in-line configuration with the FEL. Since the REMI operates with a dilute target, the FEL pulse is barely influenced by passing through the target jet and can be used for further measurements. The group of Christian Ott of MPIK designed

and commissioned a transient absorption setup using an XUV spectrometer. The FEL pulse downstream of the REMI is refocused by a toroidal mirror into a gas cell where it interacts with the sample before its spectrum is analysed on a shot-to-shot basis.

While the REMI and the XUV spectrometer can be operated independently, their cooperation provides the currently unique possibility for wavelength sorting of REMI dissociation data, introducing a new method of measurement with greatly enhanced spectral resolution [63].

Chapter 4

Data Calibration and Analysis

This chapter describes the steps that were undertaken to go from recorded detector voltage traces to ion momentum information. For information on how the detector signals were recorded, refer to Section 3.4.

Because in this work only ion momenta are described, this section is concerned with the data analysis regarding ions. The detection of electrons on the differently designed detector and under consideration of a magnetic field is not covered here. Information on the retrieval of electron momenta can be found in [56].

The data analysis consists of three steps named *acquire*, *unpack*, and *calc*.

- In the *acquire* step, the voltage traces of the detectors are translated into timing information. It uses a constant fraction discriminator (CFD) to identify the peak position within the recorded voltage traces. The output is timing information on signal peak positions in the different detector channels.
- The *unpack* step uses the peak positions in the individual channels to calculate time-of-flight and position information. Its output is a list of hits on the detector with the respective time and position values for each hit.
- In the *calc* step, the time and position information is used to identify specific ion species and calculate their initial momenta. The identified ions can then be grouped together based on conditions on their combined momenta. In case the momentum sum of a group of ions is small, they are identified to have originated from the same fragmentation process. This capability of

detecting all fragments of a dissociation in coincidence makes it possible to obtain kinematically complete information of the underlying breakup processes. The output of the *calc* step are two lists: one contains the identified ions with their assigned momentum values, the other contains the coincidences with the participating ions.

Each of the three steps requires calibration through the adjustment of parameters. The procedures of finding suitable calibration parameters is explained in detail in the following subsections.

4.1 *acquire* step

For the *acquire* step, one must specify the correct time distance between two FEL pulses. Only if this parameter is accurately adjusted can the spectra recorded for the individual FEL pulses correctly be convoluted into a single spectrum. A first approximation of the pulse distance parameter is obtained by looking at the MCP channel signal of the *acquire* step. One measures the number of histogram bins between the beginning of the first and the beginning of the last TOF spectrum, which can easily be identified by the narrow peak caused by scattered light from the FEL. This number is then divided by the number of pulses in the pulse train minus one to obtain the pulse separation in histogram bins. To convert to time information, the pulse distance in bins is multiplied by the bin size; in the case of this experiment the bin size was 1 ns. This gives the approximate time between two FEL pulses.

To obtain a more precise value, one can look at a two-dimensional histogram from the *unpack* step that shows the TOF values on the horizontal axis and the pulse number in the pulse train on the vertical axis. A typical feature to consider is, for example, the scattering light signal. If the pulse distance is correctly adjusted, it is supposed to be a straight line, meaning that the calculated arrival time of the FEL pulse does not change over the pulse train. If it tilts to one side, the pulse distance parameter needs to be adjusted, as is shown in Figure 4.1.

4.2 *unpack* step

In the *unpack* step, time signals from the MCP channel are transformed into TOF values of particles and position information is calculated from the delayline signals. Each process has its own calibration routine.

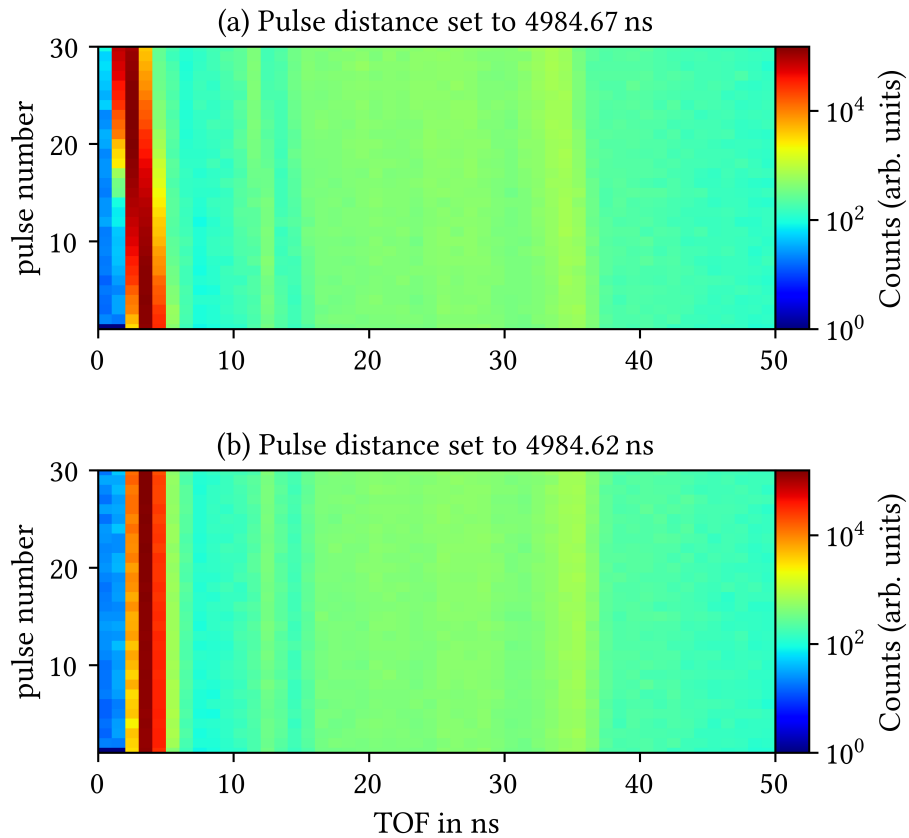


Figure 4.1: Two examples of histograms with TOF values plotted against pulse number. One pulse train consists of 30 pulses. The line at low TOF values is caused by FEL scatter light. Is it used as an indicator for the accuracy of the pulse distance parameter. When the parameter is correctly adjusted, as in (b), the TOF value does not vary with the pulse number. In that case, the individual TOF histograms are correctly superimposed. Note that the scattering light in these histograms does not arrive at time zero because no timing calibration has been done yet, as described in Section 4.2.

Every layer of the delayline anode has two channels, corresponding to the two ends of the wire. The sum of the travel times from the impact position to the two ends of the wire is constant, no matter where a particle impacted on the detector. Therefore, a time sum condition is employed to match the signals from the two pairs of delayline channels together and to filter out noise, e.g. signals in one channel that do not match a signal in the other channel of the same delayline layer with regard to the time sum condition. For more detailed information on how position information is obtained from the delayline signals, refer to [60]. Once an MCP signal is matched to its respective time-sum-condition-filtered delayline signal, their combined information needs to be transformed into TOF and position values. This requires a time offset calibration for the MCP and a position scaling and rotation for the delay lines.

For the MCP timing calibration, it is necessary to identify the precise time when the FEL pulse interacted with the target and created the detected particles. In a constant and homogeneous electric field, charged particles experience a constant acceleration, as further explained in Section 2.5.1. Their TOF value is then proportional to the square root of their mass-to-charge ratio. When plotting the TOF values against $\sqrt{m/q}$, one expects to see a straight line, characterised by a slope and a time offset. In order to correctly identify an ion species, it is important to know the time offset so one can correct for it.

In creating the TOF vs. $\sqrt{m/q}$ plot, one should look for narrow and isolated TOF peaks. Usually ions with no initial momentum after a dissociation are suitable, like the singly charged original ion or ions from the carrier gas such as helium. Background ions from the residual gas of the vacuum chamber can also be used if their peaks are isolated from other ions' TOF signals. The ions are identified in the spectrum, their TOF values are recorded and plotted against the square root of their mass-to-charge ratio. With a linear regression, a line is fitted to this data. The time offset of this line is used as the value of the time offset parameter in the data analysis *unpack* step. When now repeating the process of calculating the ions' TOF values, reading, plotting and fitting them, the resulting time offset should be zero, or at least smaller than the time resolution of the TOF spectrum. Once this is the case, time calibration is complete.

In Figure 4.2, a calibrated TOF spectrum is shown. The narrow peaks are caused by target ions with very low kinetic energy such as CH_2I_2^+ and He^+ . The broader peaks originate from ionised background gas like H_2O^+ , O_2^+ , N_2^+ , and CO_2^+ . Ions that were created in a molecular fragmentation have significant initial energy. Depending on the orientation of their initial momentum vector, this results in a large distribution of TOF values. The broad structures in the TOF spectrum belong to ion species such as I^+ , I^{++} , I^{+++} , and CH_2^+ , as well as CH_2I^+ and CH_2I^{++} .

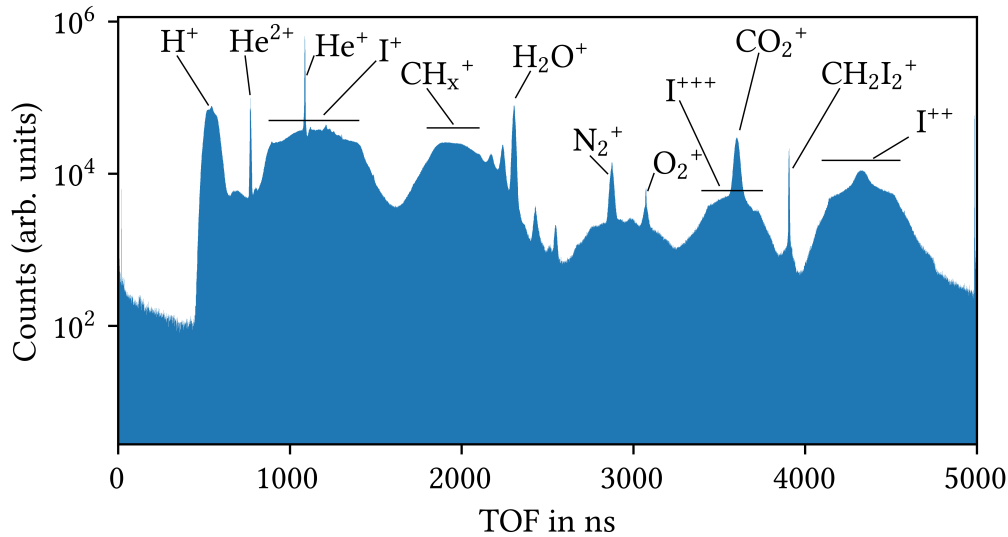


Figure 4.2: Time-of-flight spectrum of data set R960. The peaks and broad distributions of different ion species are shown. Some ions have a flight time to the detector that is longer than the pulse separation time of approximately 5000 ns.

Calibrating the detector with its two spatial dimensions requires a similar process. The goal is to have ions with zero initial momentum to be represented in the centre of the detector (at $x = y = 0$).

The first step involves centring the position coordinate system on the projected interaction point of the FEL with the target jet. In the second step, the coordinate system is rotated such that its x -axis points along the jet propagation direction. Because the particles in the jet have a significant speed compared to the change in velocity that the ions experience on their path to the detector, the initial jet velocity influences their measured position information. This initial drift velocity will be accounted for during the ion momentum calculation in the *calc* step. Here, in the *unpack* step, the calibration is done such that only ions with actual zero initial momentum appear in the detector centre at $x = y = 0$.

The centre of the position coordinate system can be shifted along its x - and y -axis by subtracting the values of the two parameters: x_0 and y_0 . The rotation parameter ϕ remains at zero for this first step.

The metric for evaluating whether x_0 and y_0 are set correctly is the ions' jet drift velocity. Only when these two parameters are well-adjusted are the initial speeds $v_x = x/\text{TOF}$ and $v_y = y/\text{TOF}$ constant for all ion species.

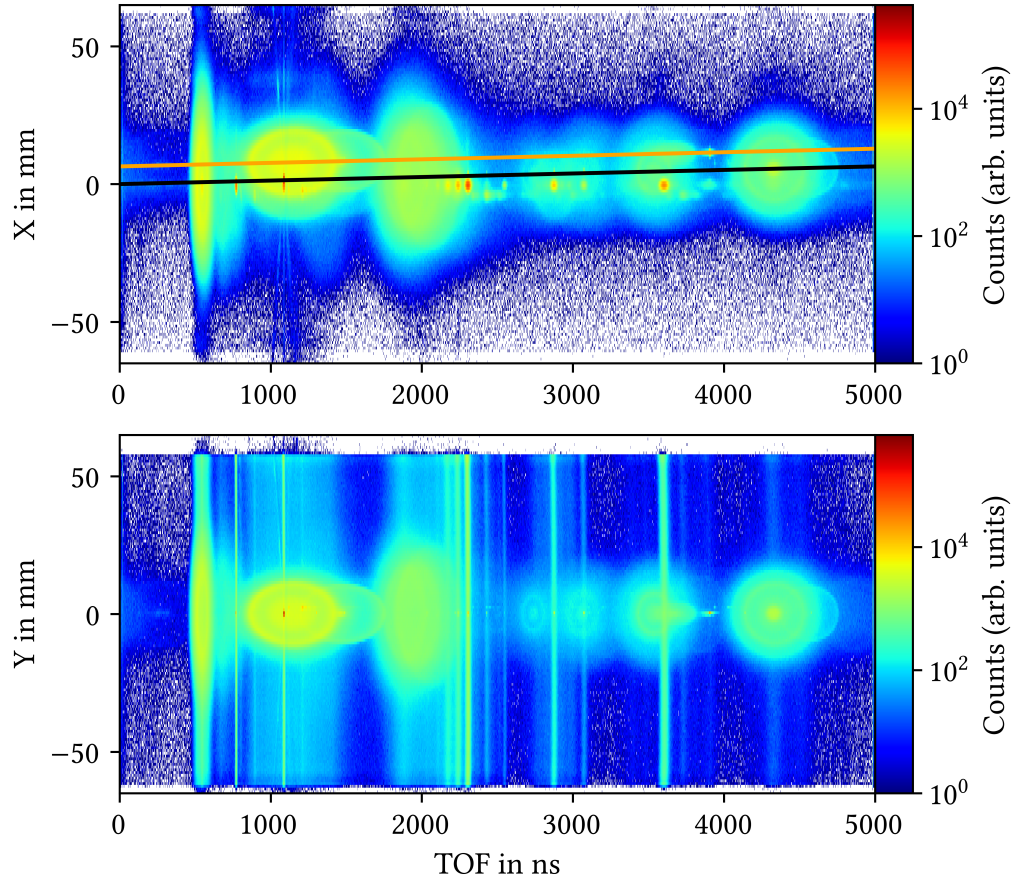


Figure 4.3: X vs. TOF (top) and Y vs. TOF (bottom) histograms of data set R960. The initial jet velocity along the x -axis results in a linear shift in x with ion TOF. The lines represent this shift for the current (black) and the previous (orange) FEL pulse. The ion peaks that have an x -position of zero do not originate from the jet. In the Y vs. TOF histogram, vertical lines indicate background ions. The FEL propagates through the spectrometer along the y -axis, so ions created from the background gas of the vacuum chamber are created at all values of y . The rings of ions originating from Coulomb explosions can be clearly recognized in both histograms.

Starting with the parameters $x_0 = 0$ and $y_0 = 0$, as well as $\phi = 0$, the drift velocities are calculated and plotted against the TOF value. The result is two two-dimensional histograms displaying the TOF value on the x -axis and the calculated speed (either v_x or v_y) on the y -axis. One should look again for ion species that do not originate from a Coulomb explosion, such that they have low initial momentum (other than their initial momentum from the jet). However, in this case it is important that they are ions from the target jet and not from the background because their initial jet velocity is used for the calibration process. When two such ion species have been identified, here named 1 and 2, their initial speeds $v_{x,1}$, $v_{y,1}$ as well as $v_{x,2}$ and $v_{y,2}$ are read from the histograms. The connection between the measured speeds, the measured position and the TOF value is (here for the x -dimension):

$$v_{x,i} = \frac{x_i}{t_i} = \frac{x_i^{true} + x'_0}{t_i} = v_x^{true} + \frac{x'_0}{t_i} \quad |i = 1, 2 \quad (4.1)$$

$v_{x,i}$ is the measured ion speed obtained with $x_0 = 0$. v_x^{true} represents the unknown true speed of the particles in the jet, which is assumed to be equal for all ion species. x'_0 is the desired calibration parameter. The same is true for the y -axis with the equivalent variables.

Subtracting the measured speeds for the two identified ion species according to Equation (4.1) gives

$$\begin{aligned} v_{x,1} - v_{x,2} &= v_x^{true} + \frac{x'_0}{t_1} - v_x^{true} - \frac{x'_0}{t_2} \\ &= x'_0 \left(\frac{1}{t_1} - \frac{1}{t_2} \right) \end{aligned} \quad (4.2)$$

Solving for x'_0 yields:

$$x'_0 = (v_{x,1} - v_{x,2}) \left(\frac{1}{t_1} - \frac{1}{t_2} \right)^{-1} \quad (4.3)$$

With correctly adjusted $x_0 = x'_0$, the speeds $v_{x,1}$ and $v_{x,2}$ are equal, which is why any following iteration of calculating x'_0 will yield zero. The same procedure is done for the y -axis to obtain the parameter y_0 . With both x_0 and y_0 correctly set, there is no difference any more among the initial speeds v_x and v_y with regard to different ion species.

Finally, the rotational orientation of the detector is calibrated. The parameter ϕ is adjusted such that the initial speed of the ions in y -direction becomes zero. Then, the x -axis of the position coordinate system is aligned with the jet propagation direction. The optimal value for ϕ was found by manual adjustment and iteration.

Figure 4.3 shows two histograms with either position dimension plotted against the TOF value. The broad distributions of energetic ions are now visible as rings. The reason for this is that a high z -component of an ion's initial momentum will result in a short or long TOF value, but simultaneously in a short travel distance in transversal direction (both x and y). Observing correlations in time and position data is a useful tool for the identification of ionic fragments from dissociation events.

With this, the *unpack* step is fully calibrated and the TOF and position values of the detector hits are forwarded to the *calc* step.

4.3 *calc* step

In the *calc* step, TOF and position values are used to identify the ion species of the detected particles. Their momenta are calculated and finally they are sorted into coincident sets of ions by employing momentum sum conditions. Each of these steps is explained in the following sections.

4.3.1 Ion identification

In the beginning of the *calc* step, there is a list of detector hits consisting of triples of time and two dimensional position information, (TOF, x , y). To assign an ion species to each of these triples, they are matched against a pre-defined list of ion species, for example CH_2^+ and I^+ . Ions of a defined species are expected to arrive in a certain time window; the CH_2^+ ions arrive much earlier than the heavier I^+ ions. Therefore, a time condition is used to filter out any detector hits with TOF values that lie outside of the expected TOF window. Similarly, a position condition can be applied to filter out detector hits with x - and y -values within a defined detector region. This can be used, for example, to filter out background ions from the FEL path that have passed the TOF condition.

Coincident ions are later matched using a momentum sum condition. This is a very efficient way of filtering out background ions which is why for the ion

identification only the TOF condition was used while the position condition let all detector hits pass.

4.3.2 Momentum calculation

Once a detector hit has been assigned an ion species, the initial momentum of that ion can be calculated from the (TOF, x , y) triple. In a homogeneous electric field $E = U/d$, charged particles experience a constant acceleration. The relation between acceleration a , time t , field extension d , and initial velocity v_z along the z -axis is therefore

$$d = \frac{1}{2}at^2 + v_z t \quad (4.4)$$

With $a = F/m = Eq/m = Uq/(dm)$ and $v_z = p_z/m$ with m and q being the mass and charge of the ion, respectively, it follows:

$$d = \frac{Uq}{2dm}t^2 + \frac{p_z}{m}t \quad (4.5)$$

Solving for p_z yields the equation that is used to calculate the momentum in z -direction from the TOF value with the ions charge and mass, the flight distance in z -direction and the spectrometer voltage as parameters:

$$p_z = \frac{2md^2 - Uqt^2}{2dt} \quad \text{with} \quad t = \text{TOF} - \Delta T_{p_z} \quad (4.6)$$

Here, TOF is the measured time of flight value and ΔT_{p_z} is a time offset parameter. ΔT_{p_z} represents the time it takes for an ion to travel from the end of the spectrometer's electric field region through the grids to the MCP. This method of calculating the momentum under the assumption that the ions passed through a homogeneous electric field until they were detected after time t is an idealised assumption. The spectrometer actually contains different regions with different electric field strengths, as explained in detail in Section 3.2.1.

The question that must be answered, then, is: What does such an idealised spectrometer model (with homogeneous electric field region) look like under the condition that it provides the same relation between initial ion momenta and measured TOF value as the real spectrometer?

The ideal method for such a momentum calibration would be to measure the dissociation of several systems with known energy releases. That way, it is possible to directly observe the relation between the known initial momenta of the ions and their TOF and position values. The parameters of the idealised spectrometer

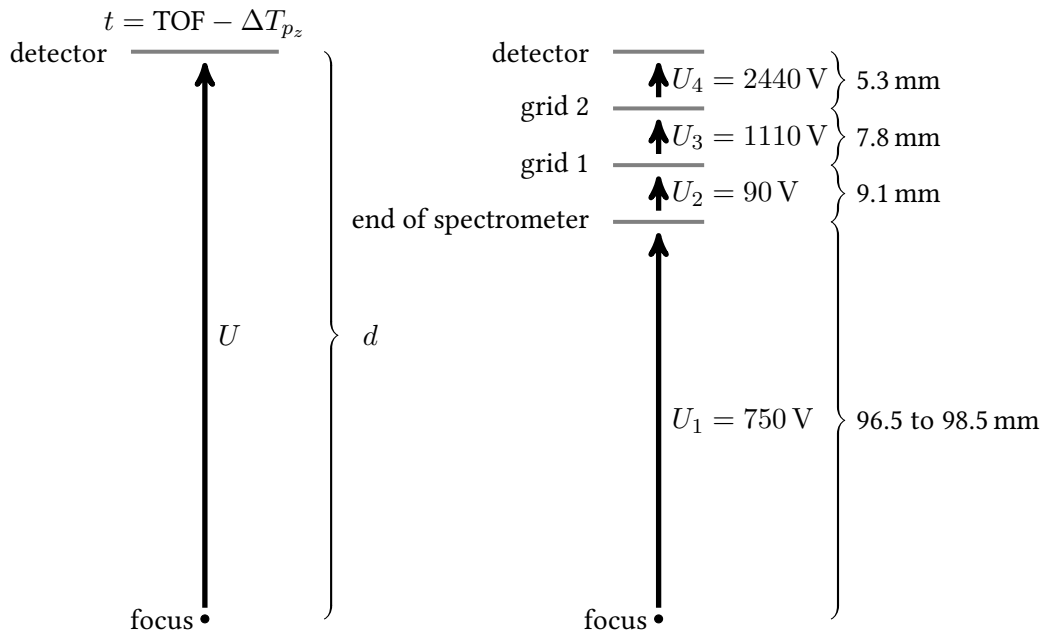


Figure 4.4: Sketch of the two linear models of the spectrometer. Left: simple model assuming a constant electric field from the focus to the detector. Voltage U , distance d and ΔT_{p_z} are parameters for the calculation of initial ion momenta from measured TOF values. Right: complex model of the spectrometer taking into account several acceleration stages between the spectrometer and the detector. The voltages and distances are approximate values for the situation during the measurement. The focus position was adjusted for each data set such that the calculated TOF values matched the data.

(flight distance d and voltage U) could then be adjusted to reproduce the known ion momenta from the measured data. Such calibration measurements were not done for the recorded data, which is why a different approach must be taken.

A more complex one-dimensional model of the spectrometer was created to translate initial ion momenta in z -direction into TOF values (see Figure 4.4). For this complex model, the real spectrometer dimensions and voltages applied during the experiment were used. When ions with an initial momentum distribution were simulated in this multi-stage spectrometer model, it generates their respective TOF distribution. The ions' maximum initial momentum was adjusted such that their maximum difference in TOF value ($t_{\max} - t_{\min}$) matches the observed TOF spread in the data.

Then, the simple spectrometer model that the analysis software employs was used to re-calculate the ions' momenta from the simulated TOF values according to Equation (4.6). The three parameters used during this back-calculation are a time offset ΔT_{pz} , the flight distance d and the spectrometer voltage U . A multi-dimensional fit function was used to adjust these three parameters until the back-calculated momentum distribution converges to the initially specified ion momenta. It is found that ΔT_{pz} , the time an ion spends to go from the end of the spectrometer and the MCP surface, depends linearly on the square root of the ions' mass-to-charge ratio, $\Delta T_{pz} \propto \sqrt{m/q}$. The resulting fit parameters are then used in the data analysis software to calculate the initial ion momenta according to Equation (4.6).

Of course it would be favourable to include this calibration method into the analysis software so that it could be automatically executed as part of the data analysis. However, as of the time of writing, this is still work in progress.

The transversal ion momenta p_x and p_y are calculated from the TOF and position information by dividing the respective distance by the flight time:

$$p_x = \left(\frac{x}{\text{TOF}} - v_{x,0} \right) \cdot m \quad (4.7)$$

$$p_y = \frac{y}{\text{TOF}} \cdot m \quad (4.8)$$

Here, the measured flight time TOF is used without the time offset parameter, because the ions' movement in transversal direction is independent of the changes in acceleration the ion experiences in z -direction. The distance an ion travels in transversal direction during its flight time TOF depends only on its initial velocity in transversal direction.

The velocity offset parameter $v_{x,0}$ is used to account for the initial jet velocity of the ions in the target. After the position calibration described in Section 4.2, the ions' initial jet velocity is aligned with the x -axis and no velocity offset parameter in y -direction is necessary.

For the molecular dissociations covered in this work, the observed ion momenta do not depend on spatial orientation. All dissociation processes appear to result in isotropic distributions of fragment momenta. It is therefore plausible to assume that the absolute momentum value an ion receives from a dissociation shall be independent of spatial orientation as well. To calibrate the ions' momenta in the transversal directions x and y , the scale parameters $scalePx$ and $scalePy$ are multiplied with each ion's momentum value in x - and y -direction, respectively. They are chosen such that the width of each of the transversal momentum distributions is equal to the width in the already calibrated z -direction.

4.3.3 Momentum resolution

The resolution with which the ion momenta can be obtained depends on various aspects of the measurement setup, some of which are dependent on the momentum dimension.

The detectors have an intrinsic timing accuracy which is on the order of a few hundred picoseconds for an MCP. Inhomogeneities of the electric field are an additional limitation to momentum resolution. Finally, variation of the initial position and velocity of the target molecule before ionisation further limit the measurement's accuracy.

[60] has measured with the same spectrometer, identical detectors and the same method of target jet preparation. There, the temperature distribution of iodine molecules in the jet were analysed. It was found that only the temperature distribution in jet propagation direction along the x -axis was affecting the momentum resolution. According to [60], for ions with low momentum the primary limitation on momentum resolution is the jet temperature distribution while at higher momenta inhomogeneities of the electric field limit the resolution.

The uncertainties of ion momenta (FWHM) in the three spatial dimensions were determined by [60] to be 12 au for p_x , 2.0 au for p_y and 0.1 au for p_z for measuring iodine ions. By error propagation, the uncertainty of the total ion momentum p is:

$$\Delta p = \frac{2}{p} \sqrt{(p_x \Delta p_x)^2 + (p_y \Delta p_y)^2 + (p_z \Delta p_z)^2} \quad (4.9)$$

In an isotropic distribution of ion momentum p in three dimensions, the values of p_x , p_y , and p_z form the surface of a sphere. The mean value of each momentum component squared in such a case is $p_i^2 = p^2/3$. Using this approximation in Equation (4.9) gives the uncertainty of the total momentum:

$$\Delta p \approx \frac{2}{\sqrt{3}} \sqrt{(\Delta p_x)^2 + (\Delta p_y)^2 + (\Delta p_z)^2} \approx 14 \text{ au} \quad (4.10)$$

When kinetic energies are calculated from ion momenta, the energy error depends on the ion's mass and its energy:

$$E_{\text{kin}} = \frac{p^2}{2m} \Rightarrow \Delta E_{\text{kin}} = \frac{p}{m} \Delta p = \sqrt{\frac{2E_{\text{kin}}}{m}} \Delta p \quad (4.11)$$

4.3.4 Coincidence detection

Ions from the same FEL pulse are said to be coincident when the sums of all their momentum components are below an adjustable threshold value. The momentum sum is then small and the ions are considered to have originated from the same dissociation event.

When plotting the TOF values of all ions of one species against the TOF values of another species, a diagonal coincidence line will appear if some of the selected ions appear in coincidence, as described in Sections 4.2 and 2.5 in more detail. A two-dimensional condition can then be placed to accept only ion pairs on the line as valid coincidences. The momentum sum in z -direction then is already very narrow, as expected when selecting ion pairs with correlated TOF values, which correspond to correlated z -momenta. There is a background underlying the coincidence line which is composed of particles that did not originate from the same fragmentation but that nevertheless have a z -momentum sum close to zero. These can be misidentified background ions (e.g. CO_2^+ has a similar flight time than I^{+++} ions) as well as actual ions of the coincident species but from different original molecules. Since their momenta are not correlated, their momentum sums in transversal direction will most probably not be zero. Therefore, narrowing the momentum sum conditions in x - and y -direction filters out most of the background signal. The momentum sums for all three dimensions as well as the coincidence line for the channel $\text{I}^{+++} + \text{CH}_2\text{I}^+$ can be seen in Figure 4.5.

An electron with a kinetic energy of 100 eV has a momentum of 2.7 au. Since the photon energy used in the measurement presented in this work was 97.6 eV,

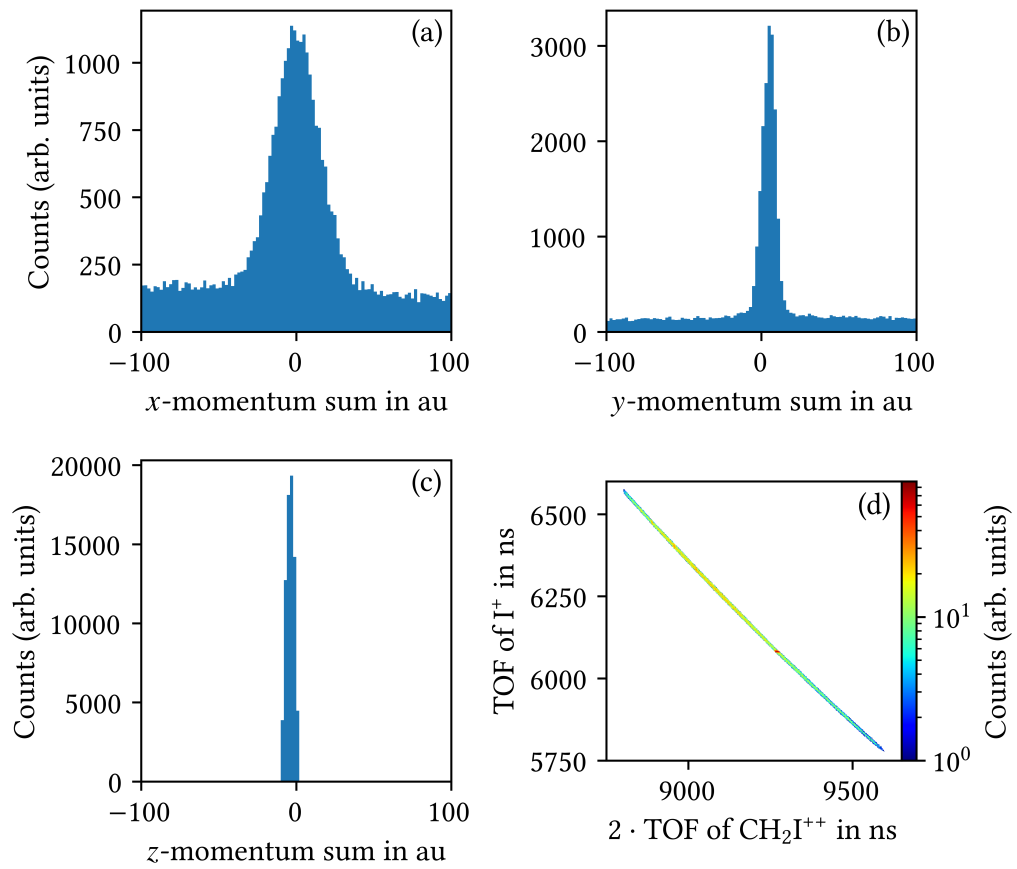


Figure 4.5: (a) to (c): momentum sum spectra of coincidence channel $\text{CH}_2\text{I}^{++} + \text{I}^+$ from data set R947. (d): PiPiCo histogram after two-dimensional condition is applied to extract coincidence line.

no electron emitted from an irradiated molecule can have a momentum larger than 2.7 au. This is larger than the total ion momentum resolution as described in Section 4.3.3.

Chapter 5

Fragmentation Dynamics of Diiodomethane

In the experiment presented in this work, diiodomethane molecules were irradiated by FEL pulses with a photon energy of 97.6 eV and a pulse duration of approximately 50 fs. The intensity in the focus region was estimated to be $3 \times 10^{15} \text{ W cm}^{-2}$. The incoming FEL pulses were split into two parts and one part was delayed relative to the other in a pump-probe measurement technique. The delay was varied between -1 and 1 ps. The CH_2I_2 molecules were ionised and some fragmented after photon absorption. The created ions were detected in coincidence with a reaction microscope, presented in Chapter 3.

The ions and coincidence channels of the dissociation of CH_2I_2 are presented in this chapter according to the number of photons that were absorbed by the molecule. When multiple photons are absorbed, there can exist a time delay between the two absorption processes due to the adjusted delay between the two XUV pulses. A fragmentation process initiated by one-photon absorption fundamentally cannot exhibit any dynamics that depend on the temporal shift between the two pulses. In addition, the charge states reached by one-photon absorption are, generally speaking, lower than the number of charges created by two or more photons.

The iodine atom has a giant resonance for inner-valence ionisation around 90 eV (see Section 2.2). The cross section for photon interaction in this energy region is dominated by photoionisation of a 4d electron [41]. The singly charged ion created by 4d ionisation is highly excited and can undergo de-excitation via Auger decay. The relaxation can take two forms: single Auger decay in which a second electron is emitted, and double Auger decay [41]. Double Auger decay is a cascade of two Auger decays which each emit a further electron such that the final

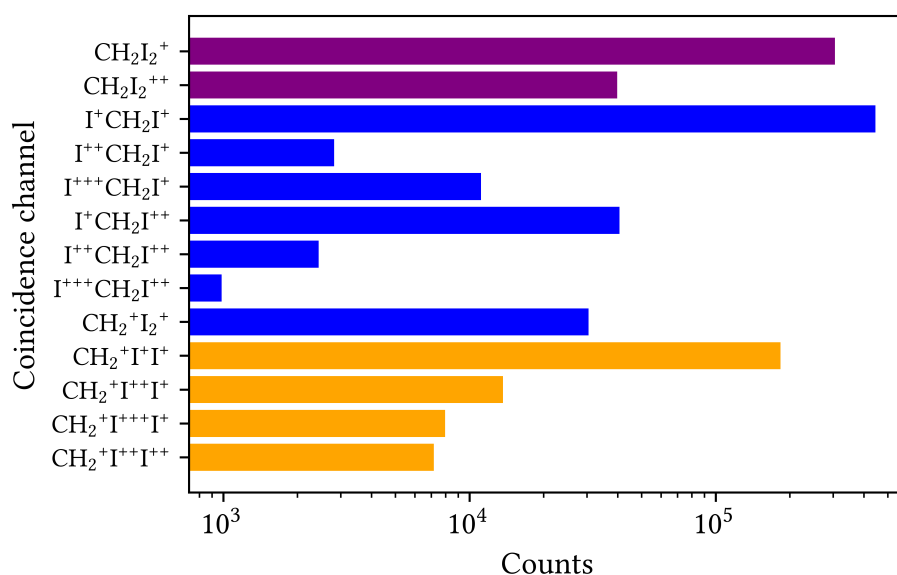


Figure 5.1: Total number of coincidence events measured for each fragmentation channel up to a total charge state of 5+. The numbers have not been corrected for detector efficiency.

charge state reached is I^{+++} . Thus, by absorption of a single XUV photon, the iodine atom can ultimately be doubly or triply charged. The 4d giant resonance has been observed in iodine ions as well. Both I^+ and I^{++} show a maximum cross section for 4d ionisation of 23 Mb for I^+ and 24 Mb for I^{++} , respectively, around a photon energy of 90 eV [25]. The 4d-hole-excited doubly charged iodine can relax through single and double Auger decay, but the probability for single Auger, resulting in I^{+++} , is much higher [25]. 4d ionisation of I^{++} followed by single Auger decay results in I^{4+} ions.

The 4d shape resonance exists in molecular iodine as well [6, 60] and has been demonstrated in other molecules containing iodine such as CH_3I [14, 31]. It was noted in [31] that the behaviour of the I atom in the CH_3I molecule was atomic-like, showing quite similar ionisation dynamics as an isolated iodine atom. It is therefore expected that the iodine atoms in CH_2I_2 exhibit similar behaviour regarding 4d inner valence ionisation via the giant resonance followed by Auger decay.

Several ion pairs and triples have been detected in coincidence after fragmentation of the diiodomethane molecules. Figure Figure 5.1 gives an overview over the coincidence channels detected in this measurement, up to a total charge state

of 5+. It is not always possible to separate the ion species C^+ and CH^+ due to their broad distribution of initial momentum which they gain in part from fragmentation of the CH_2 group. Additionally, the detection of H^+ ions from the target is difficult because of the large signal from the hydrogen background gas that is dissociated into protons by the FEL pulse. Therefore, in this work, only coincidences where the CH_2 group remains intact are considered.

At first, a distinction is made regarding the number of photons that were absorbed to create the detected ions. The methods to identify the photon number for a specific ion species or set of coincident ions are three-fold:

- A single XUV photon can create up to three charges in a CH_2I_2 molecule via 4d ionisation followed by double Auger decay. This means that ions with a charge state of 4+ and higher must have been created by a process that was initiated by the absorption of more than one photon. The same is true for coincident fragments of molecular dissociation where the added charge states of all participating ions exceed 3+.
- When fragmentation is initiated by a single XUV photon, the combined kinetic energy of all ions of a coincidence channel (called kinetic energy release, KER) must be constant with delay. This does not mean that all fragmentation channels with a delay-independent KER have been initiated by a single photon; two or more photons may be absorbed from the same pulse and none from the other pulse, still resulting in a constant KER with respect to the delay. This is for example the case for the coincidence of $CH_2^+ + I^{++} + I^+$, caused by the absorption of two photons, which exhibits a constant KER channel as well as a channel where KER is decreasing with delay.
- The probability to absorb n photons is proportional to the FEL intensity to the power of n . Therefore, the ion yield for a one-photon process is expected to increase linearly with the FEL intensity. Observing the ion yield depending on the FEL intensity is therefore an indicator for the number of photons that were absorbed in the creation of these ions.

Section 5.1 presents the ions and coincidences for one-photon absorption. The different fragmentation pathways leading to $CH_2^+ + I^+ + I^+$ coincident ions are presented there. Section 5.2 covers the dynamics of molecular dissociation probed by delay-dependent fragmentations with emphasis on the measurement of charge transfer timescales.

5.1 Dissociation by absorption of a single XUV photon

The ions that are observed to originate from molecular fragmentation following one-photon absorption are CH_2^+ , I^+ , CH_2I^+ , CH_2I^{++} , and I_2^+ . Additionally, singly and doubly charged original molecules were detected: CH_2I_2^+ and $\text{CH}_2\text{I}_2^{++}$. Since the Auger decay timescale is on the order of a few femtoseconds, it is likely that the singly charged molecule is formed by regular valence ionisation. Figure 5.2 shows a summary of the identified fragmentation pathways following one-photon absorption.

In the following subsections the detection of coincident ions is separated by total charge state. Section 5.1.1 covers dissociation following single Auger decay with a total charge state of 2+. The coincidences originating from molecules that de-excite by the double Auger process are described in Section 5.1.2. In Section 5.1.3, the results of simulations conducted by Martín et al. are compared to the measured momentum correlation of the $\text{CH}_2^+ + \text{I}^+ + \text{I}^+$ coincidence channel.

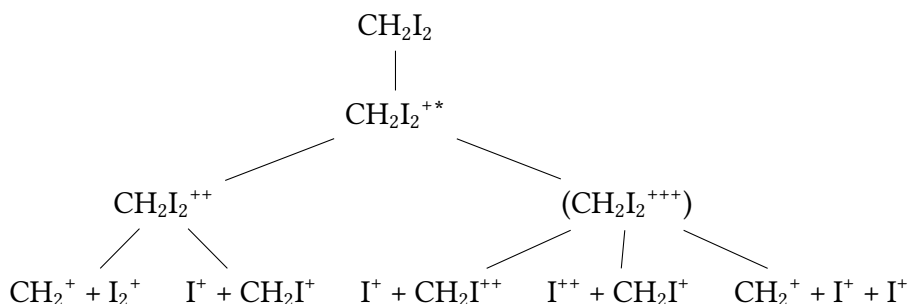


Figure 5.2: Dissociation pathways detected following absorption of a single XUV photon. The $\text{CH}_2\text{I}_2^{++}$ and CH_2I^{++} ions have been recorded at the detector, so they can be stable on the microsecond scale. The triply charged CH_2I_2 ion, however, has not been detected.

5.1.1 Single Auger decay: 2 charges

When single Auger decay occurs after 4d ionisation, the doubly charged parent molecule does not always dissociate quickly. Some $\text{CH}_2\text{I}_2^{++}$ molecules stay intact for at least several microseconds and reach the detector without dissociating. The fraction of non-dissociating $\text{CH}_2\text{I}_2^{++}$ molecules is estimated to be less than 5%.

When dissociation of the doubly charged diiodomethane molecule occurs, two coincidence channels are detected under participation of two singly charged ions each: $I^+ + CH_2I^+$ and $CH_2^+ + I_2^+$. Not considering the formation of neutral fragments and under the condition that the CH_2^+ group stays intact, as mentioned above, these are the only two possibilities to separate a CH_2I_2 molecule into two singly charged fragments. The number of detected coincidence events shows that the $I^+ + CH_2I^+$ dissociation occurs around 15 times more often than the fragmentation into I_2^+ and CH_2^+

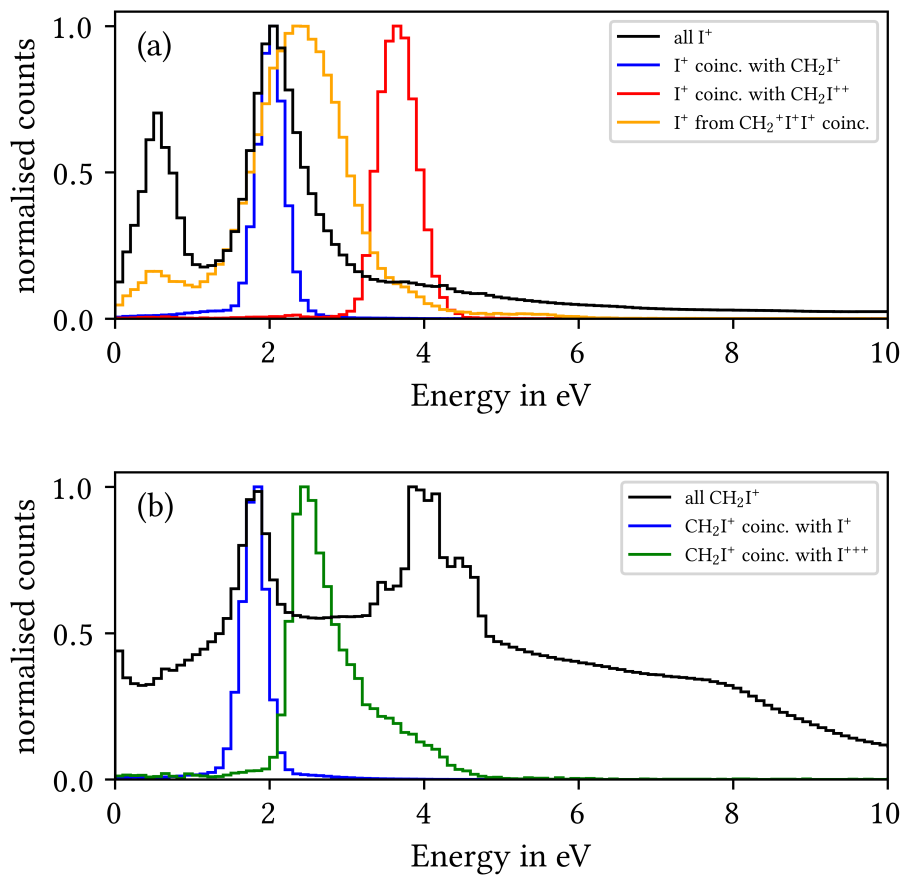


Figure 5.3: Energy spectra of the ions I^+ (a) and CH_2I^+ (b). Superimposed are the energy distributions that belong to specific coincidence channels as depicted in the legend. All spectra have been normalised to their maximum value.

The energy spectra of the detected ions are presented in Figures 5.3 and 5.4. The energy of all detected ions are plotted in comparison with the energy spectra of the ions measured in coincidence. All spectra have been normalised with re-

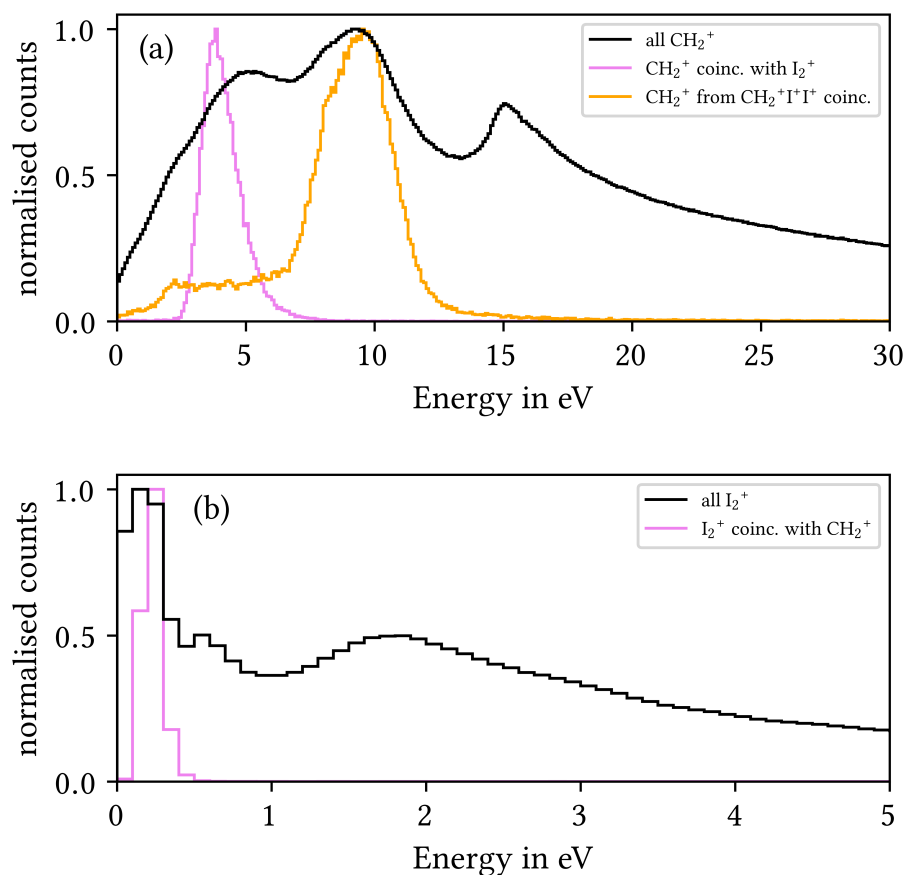


Figure 5.4: Energy spectra of the ions CH_2^+ (a) and I_2^+ (b). Superimposed are the energy distributions that belong to specific coincidence channels. All spectra have been normalised to their maximum value.

gards to their maximum. The sets of ‘all’ ions have only been identified by their TOF value, no position or other filter conditions have been applied. Their spectra therefore contain in some cases significant contributions from background ions, carrier gas ions or other target ions with a similar time-of-flight. For example, the energy spectrum of the CH_2I^+ ions contains a large peak at around 4 eV originating from the carrier gas He^+ ions from the previous FEL pulse. These contaminations are effectively filtered out by the momentum sum conditions of the coincidence analysis. Therefore, the coincident ions have in most cases a much more narrow energy distribution.

The I^+ ion, as shown in (a) of Figure 5.3, exhibits two distinct peaks in its energy distribution at approximately 0.6 eV and 2.0 eV. Additionally, there is a shoulder

feature at around 3.7 eV. The energy peak at 2.0 eV originates from the coincidence with an CH_2I^+ ion of around 1.8 eV (see energy spectrum of CH_2I^+ in (b) of Figure 5.3).

The CH_2I^+ ion has two peaks as well: one close to zero energy and one at 1.8 eV, the latter from the $\text{I}^+ + \text{CH}_2\text{I}^+$ coincidence. There is a broader additional distribution at higher energies.

Very low energy values such as the peak around 0.6 eV in I^+ and the CH_2I^+ ions with less than 1 eV are assumed to originate mainly from dissociation with a neutral partner. In the REMI experimental setup, only charged particles can be detected, which is why coincidences with neutral fragments are not investigated here.

The coincidence channel of $\text{I}^+ + \text{CH}_2\text{I}^+$ exhibits a single KER peak at approximately 3.9 eV (see Section 5.1.1). In a system of two point charges separated by a known distance, the electrostatic potential energy can be calculated. The distance at which two positive unit charges have a potential energy of 3.9 eV is around 370 pm. This is slightly larger than the maximum distance of two atoms in the ground state of the CH_2I_2 molecule, which is the distance between the two iodine atoms at 341 pm (not considering the hydrogen atoms). The reason for this mismatch may be that the analysis calibration yields too small values for the ion energies or that the molecular geometry changed in the time between the XUV photon absorption and the final dissociation into I^+ and CH_2I^+ ions, or a mixture of both reasons.

The second dissociation channel, $\text{CH}_2^+ + \text{I}_2^+$, has a similar KER with a maximum at 4.0 eV but a much wider distribution (Section 5.1.1). The energy distributions of the ions CH_2^+ and I_2^+ are shown in Figure Figure 5.4. Due to the much larger mass difference between these ion species, the energy distribution is accordingly much more asymmetric: the CH_2^+ ion receives almost all of the energy (3.8 eV) while the I_2^+ receives only around 0.2 eV.

The electrostatic potential energy of 4.0 eV corresponds to a charge separation distance of 360 pm. This is still slightly longer than the I–I distance in the molecular ground state and much longer than the C–I distance of 212 pm. Because the internuclear distance of molecular iodine is only 267 pm [23] and therefore shorter than the I–I distance in the CH_2I_2 ground state, it is plausible that the original molecular geometry changes after ionisation to enable the separation into I_2^+ and CH_2^+ . However, the possible change of the molecular structure in the time between ionisation and fragmentation cannot be determined in this type of dissociation. From two-body dissociation initiated by one-photon absorption,

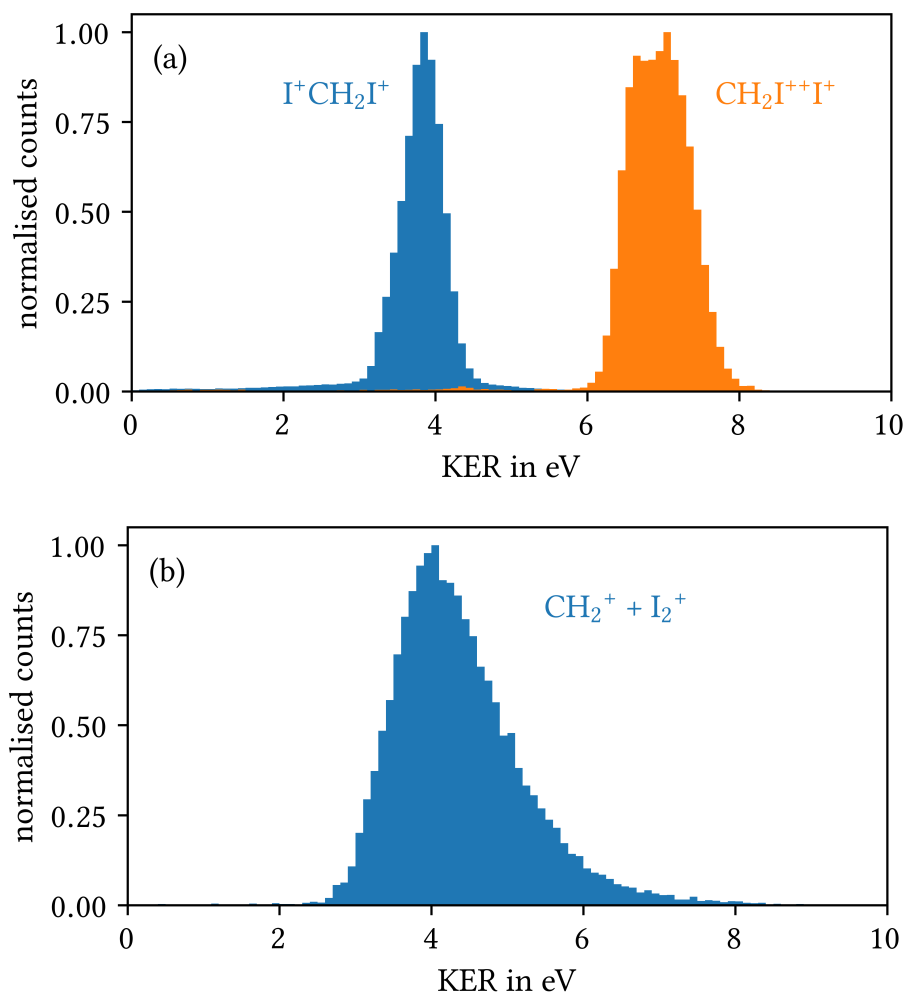


Figure 5.5: KER spectra of the two-body fragmentation processes observed after one-photon absorption. (a): $I^+ + CH_2I^+$ and $CH_2I^{++} + I^+$ coincidences. (b): $CH_2^+ + I_2^+$ coincidence.

neither momentum correlation nor temporal information can be extracted. This changes regarding momentum correlations for dissociation involving three final fragments, as shown in the next subsection.

5.1.2 Double Auger decay: 3 charges

When three charges are created in the CH_2I_2 molecule due to double Auger decay, other dissociation channels compared to the case of two charges appear. In

addition to two-ion coincidence channels with asymmetric charge distribution, the fragmentation into three charged particles becomes possible.

Two-body fragmentation into $\text{CH}_2\text{I}^{++} + \text{I}^+$ has been detected with a KER of approximately 7.0 eV (see Section 5.1.2). The ion energies are higher than for the $\text{I}^+ + \text{CH}_2\text{I}^+$ channel because of the increased combined charge state and the stronger electrostatic repulsion of the fragments. The CH_2I^{++} ion participating in this dissociation receives 3.3 eV of energy (see Section 5.1.2). The shoulder feature at approximately 3.7 eV in the I^+ energy distribution (see Figure 5.3) is the signature of the $\text{CH}_2\text{I}^{++} + \text{I}^+$ dissociation channel.

The fragmentation into a doubly charged iodine and a singly charged CH_2I^+ molecule is strongly suppressed. The ratio of events in the channels $\text{I}^{++} + \text{CH}_2\text{I}^+$ to $\text{I}^+ + \text{CH}_2\text{I}^{++}$ is approximately 0.07. The number of events detected is insufficient to discern any clear energy distribution of the fragments. It appears that after double Auger decay, the iodine ion that is emitted from the molecule in a two-body fragmentation almost always has a charge state of 1+.

It is interesting to note that the detection of CH_2I^{++} shows how this doubly charged cation can be stable for at least several microseconds. It is later concluded that instances of CH_2I^{++} ions exist which continue to dissociate into I^+ and CH_2^+ . Their lifetime must be much shorter than the microsecond scale, as is inferred from momentum correlations in triple ion coincidences.

The triple ion dissociation channel of CH_2I_2 into $\text{CH}_2^+ + \text{I}^+ + \text{I}^+$ has a broad KER range from approximately 11 to 17 eV. The KER does not vary with the delay between the two pulses, as shown in Figure 5.7, which substantiates that this fragmentation is initiated by one-photon absorption.

In two-body fragmentation, when viewed from the rest frame of the original molecule, the momentum vectors of both particles are always antiparallel to each other and identical in magnitude due to momentum conservation. Momentum conservation in the data analysis is enforced by the momentum sum conditions. In three-body fragmentation, the three momentum vectors always define a plane, again due to momentum conservation. However, both the length of its momentum vector as well as its direction relative to the other fragments' momentum vectors can vary depending on the dynamics of the breakup process. Studying correlations both of absolute momentum and of direction can therefore give insight into how the fragments formed from the original system. One suitable method of displaying this momentum correlation information is a Newton plot. In short, a Newton plot is created by rotating the rest frame of the dissociated sys-

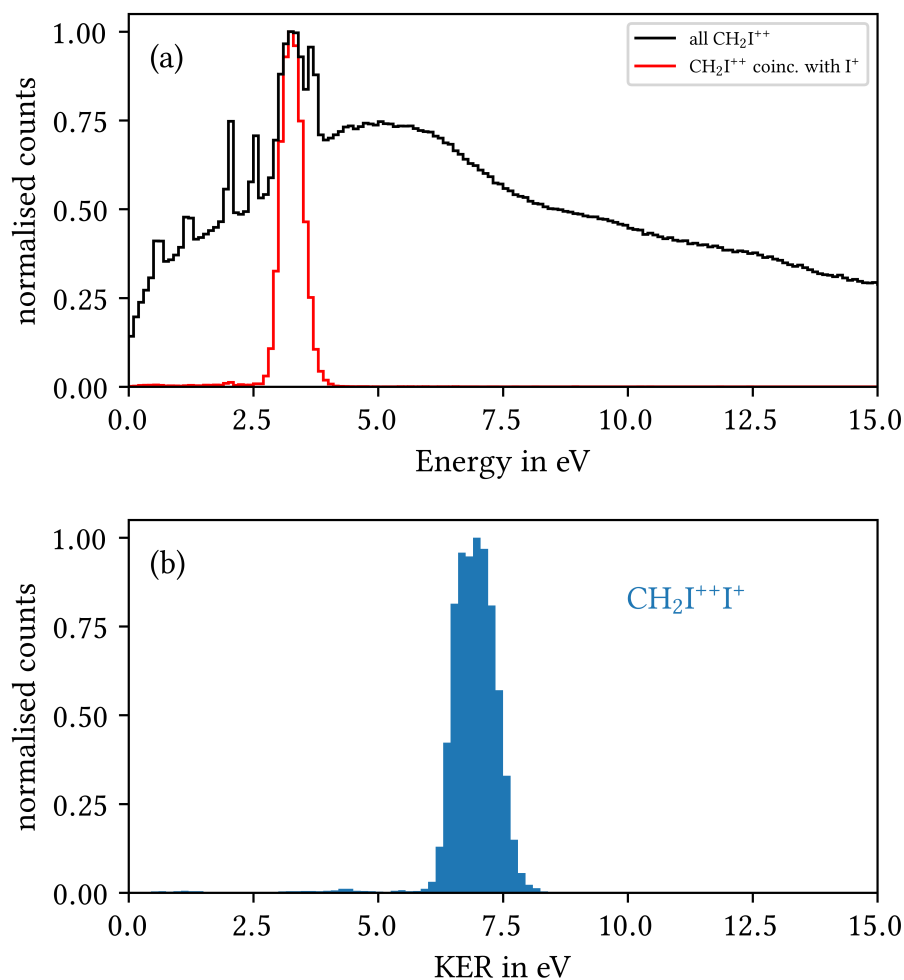


Figure 5.6: (a): Energy spectrum of CH_2I^{++} with superimposed contributions from specific coincidence channels. (b): KER spectrum of coincidences $\text{CH}_2\text{I}^{++} + \text{I}^+$. All spectra have been normalised to their maximum value.

tem such that the momentum vector of one specific fragment is always oriented parallel to the x -axis of the diagram. Plotted are then the momentum values of the other two fragments according to their x - and y -coordinates. The momentum of the first fragment which defines the axis is not plotted, it only defines the frame of reference. Even though a Newton plot does not display the actual coincident ion triples, it can show how the momenta of all three ions correlate with regard to their direction and, in the case of the plotted ion momenta, also their magnitude.

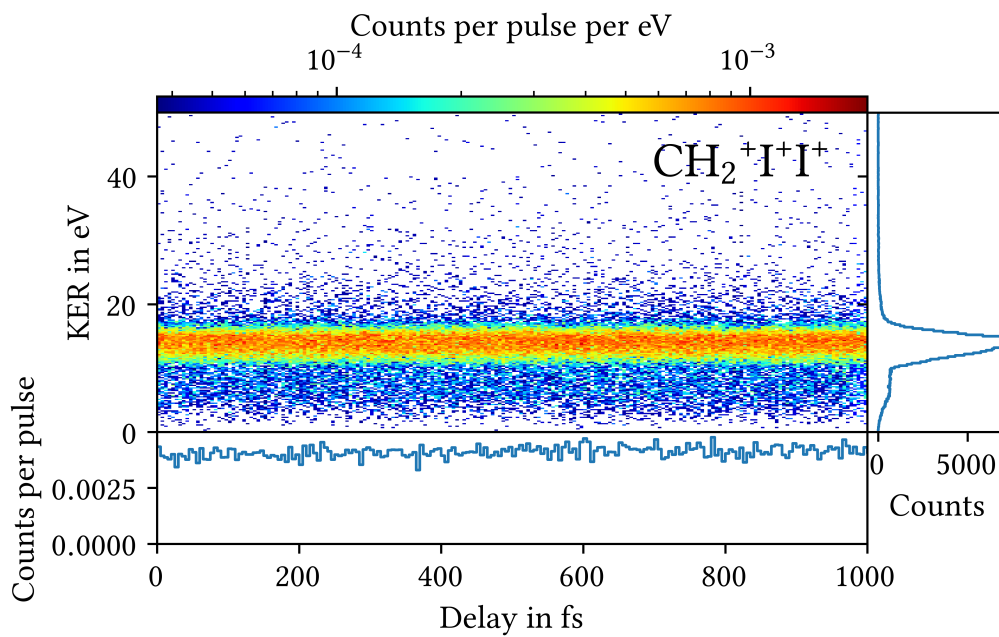


Figure 5.7: KER vs. delay histogram of the $\text{CH}_2^+ + \text{I}^+ + \text{I}^+$ coincidence channel. The KER does not vary with the delay, as expected for a one-photon process, confirmed by the projection on the delay axis.

The Newton plot for the $\text{CH}_2^+ + \text{I}^+ + \text{I}^+$ dissociation is shown in Figure 5.8 with the CH_2^+ ion momentum along the positive x -axis (not plotted). The three insets show each ion's respective absolute momentum spectrum.

Two distinct features can be observed in the plot: The most prominent structure is an oval shape with maxima at the upper and lower parts. Outside of the oval there are two larger rings similar in diameter that encompass the oval shape and are shifted against each other along the x -axis.

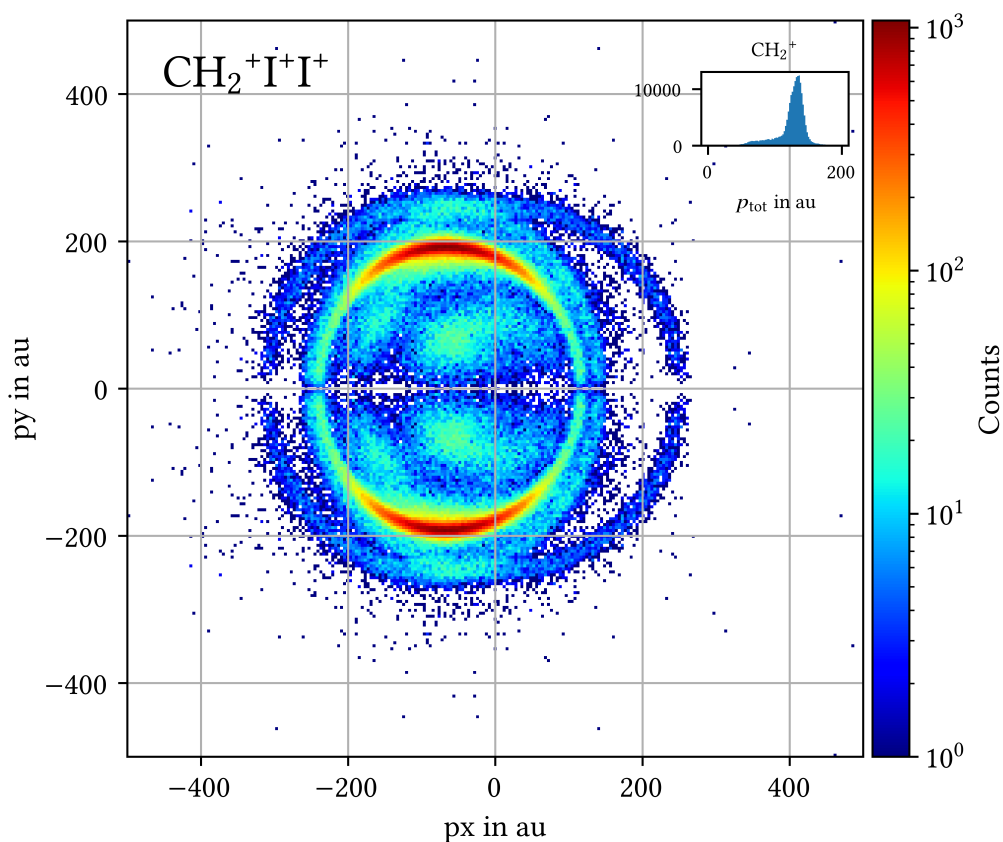


Figure 5.8: Newton plot of the one-photon dissociation of CH_2I_2 into CH_2^+ , I^+ , and I^+ . The inset shows the total momentum spectrum of the CH_2^+ ion.

The maxima on the oval shape are a result of direct three-body breakup of the CH_2I_2 ion, also called the concerted fragmentation pathway. When the triply charged original molecule directly breaks apart into two iodine ions and a CH_2^+ group, the momenta of the ions are primarily the result of electrostatic repulsion. This conclusion is substantiated by classical simulations (see Section 2.3 for details on the simulation methods). When simulating the dissociation solely

on the basis of electrostatic repulsion, the resulting ion momenta reproduce the two maxima of the Newton plot, as shown in Figure 5.10.

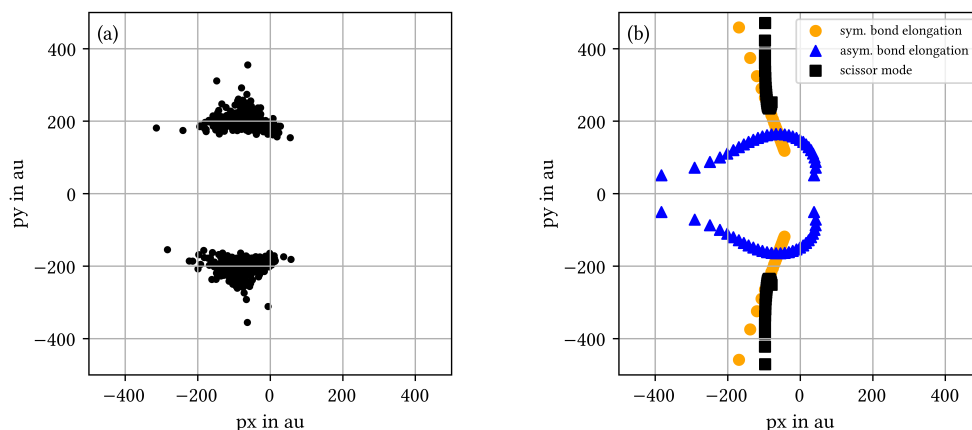


Figure 5.9: Newton plots of simulated $\text{CH}_2^+ + \text{I}^+ + \text{I}^+$ concerted dissociation. The momentum of the CH_2^+ fragment is not plotted. (a): The initial positions of the three ionic fragments were randomly varied around the molecular ground state geometry. (b): Different modes of molecular vibration affect the initial positions of the atoms and, therefore, the resulting momenta.

The large ring structure in the Newton plot (Figure 5.8) cannot be explained by variations of the initial molecular geometry. Stretching of the C–I bonds, both symmetric and asymmetric, as well as the scissor vibrational mode of the CH_2I_2 molecule fail to reproduce these rings, as indicated by the classical simulation results shown in Section 5.1.2. This indicates that the rings must be created by a process other than concerted three-body fragmentation.

Similar ring structures have been observed for three-body fragmentation of molecules before [42, 49, 67]. They have been interpreted as the result of a sequential breakup process via an intermediate rotating molecular ion. In particular, [22] observed similar ring structures in a Newton plot of the $\text{CH}_2^+ + \text{I}^+ + \text{I}^+$ coincidence channel after diiodomethane molecules were exposed to near-infrared laser radiation.

When simulating a sequential breakup of the CH_2I_2 molecule via an intermediate CH_2I^{++} ion, the resulting momentum correlations appear to be similar to the data, as shown in Figure 5.10. The simulation started from the molecular ground state geometry with one unit charge at each of the iodine atoms and the carbon atom. The CH_2^+ group and one of the iodine atoms were bound together via a

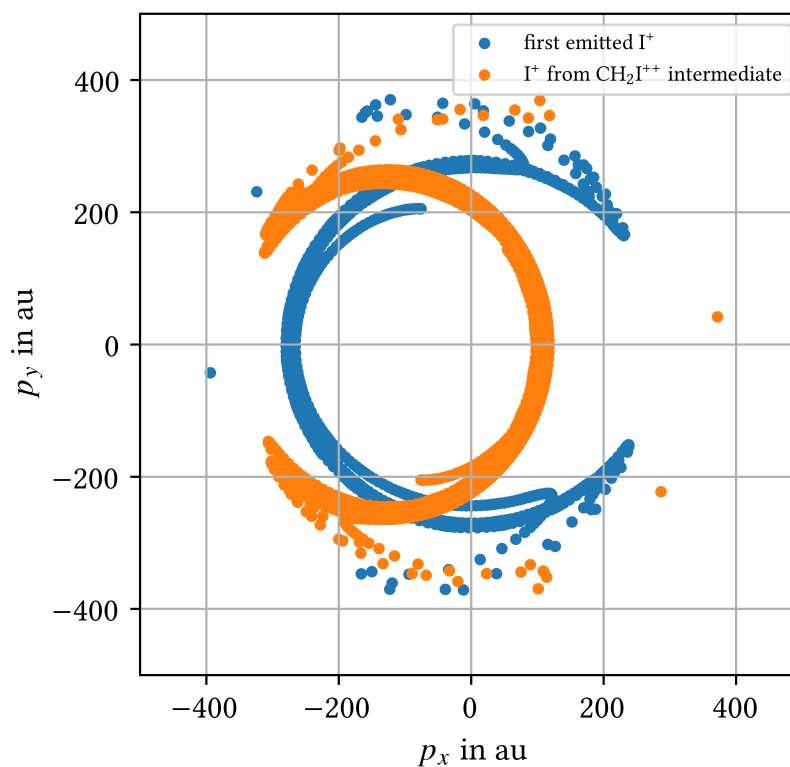


Figure 5.10: Newton plot of the simulated sequential three-body dissociation of CH_2I_2 into $\text{CH}_2^+ + \text{I}^+ + \text{I}^+$ via an intermediate CH_2I^{++} molecular ion. The two colors represent the different iodine atoms: blue is the first ejected I^+ , orange is the I^+ from the CH_2I^{++} group. The time at which the binding potential in the CH_2I^{++} ion is switched off is varied from zero to 1000 fs in steps of 1 fs.

simulated Lennard-Jones potential. Due to the electrostatic repulsion between the primary emitted I^+ ion and the charge at the carbon atom, a rotation is induced in the intermediate CH_2I^{++} molecular ion. When some time has passed, the binding potential is switched off and the molecular ion dissociates into I^+ and CH_2^+ fragments. The time at which this secondary dissociation occurs influences the orientation of the final ion momenta.

It is difficult to predict where in the CH_2I^{++} ion the charges are located. A carbon atom has a slightly lower electronegativity than an iodine atom and has been described as an electron donor in the context of molecular Auger decay [11]. It is therefore assumed that at least one of the charges is located at the carbon atom. In general, the simulation reproduces the ring structure in momentum space for a variety of charge distributions within the CH_2I^{++} ion, as long as the geometric

centre of the charges is closer to the carbon atom than the centre of mass. Once the charge centre is placed close to the centre of mass (which is located near the iodine atom), the rotation induced by electrostatic repulsion slows down significantly. The orientation of rotation is inverted when the charge centre is on the iodine-side of the centre of mass and the resulting simulated momentum correlation changes drastically, such that it does no longer resemble the measured momentum distribution.

The classical simulation based on electrostatic repulsion can reproduce the outer ring structure observed in the $\text{CH}_2^+ + \text{I}^+ + \text{I}^+$ dissociation channel by assuming a sequential breakup via a rotating intermediate CH_2I^{++} molecular ion. It is therefore concluded that there are at least two different competing dissociation pathways in the $\text{CH}_2^+ + \text{I}^+ + \text{I}^+$ coincidence: direct three-body dissociation and sequential dissociation via a rotating intermediate CH_2I^{++} state.

5.1.3 ADMP Simulation of CH_2I_2 fragmentation

More sophisticated simulations have been performed on the fragmentation of CH_2I_2 molecules by Fernando Martín et al. The results of these calculations are presented here and compared to the measurements as well as to the classical simulations.

Martín et al. performed molecular fragmentation calculations using the ‘Atom Centered Density Matrix Propagation’ (ADMP) molecular dynamics model at the B3LYP/SDDall theory level. Sergio Díaz-Tendero of Martín’s research group, describes the calculations with the words: ‘This method performs trajectory simulations similar to Born-Oppenheimer molecular dynamics but with a reduced computational cost. ADMP belongs to the extended Lagrangian approach to molecular dynamics, using Gaussian basis functions and propagating the density matrix.’ [12] Details on the calculation method can be found in [18, 54, 55]. In short, the forces acting on the atoms are derived by calculating the electronic potential energy surfaces of the molecule. The atoms are then propagated classically through time according to the resulting accelerations. The output of the simulation is three-dimensional trajectories of all five atoms. The time step is 0.1 fs and the simulated time is 2000 fs.

The initial state is the electronic ground state of the $\text{CH}_2\text{I}_2^{3+}$ molecule. The five atoms (two iodine, two hydrogen and one carbon atom) are arranged according to the ground state geometry of the neutral molecule, ignoring any rearrangement that may have occurred between ionisation and Auger decay. Martín et al. have used a ground state geometry different from the data published by PubChem and

Channel	initial energy		
	1 eV	3 eV	5 eV
I/CH ₂ I	100	87	30
H/CHI ₂	0	0	6
CH ₂ /I/I	0	13	61
H/I/CHI	0	0	3

Table 5.1: Branching ratios of the fragmentation simulations by Martín et al. Values are in percent of the total number of simulation instances.

used for the classical simulations described above. For these ADMP calculations, the initial C–I bond length was assumed to be 220 pm (4.16 au) and the initial I–I distance was 373 pm (7.05 au), leading to a larger angle of 116° between the two C–I bonds (compared to $\sim 107^\circ$ for the classical simulations).

The precise effects of the Auger decay on the molecular electronic states is unknown and ignored by the simulation. Assuming that the triply charged molecule is in its electronic ground state is a simplification. In this electronic ground state, rotational and vibrational excited states are most probably introduced by the XUV photon absorption and subsequent Auger decay. However, the precise nature of these states and their population density as unknown as well. Therefore, Martín et al. introduced an initial excitation energy into the molecular system to approximate excited vibrational and rotational states.

The total amount of initial excitation energy is pre-defined (either 1, 3, or 5 eV) and randomly distributed among the five atoms in the form of initial kinetic energy. The trajectory calculation is deterministic, which means a given ground state geometry of atoms with zero initial momentum results in one determined set of atom trajectories. The random distribution of initial kinetic energy and, therefore, momentum among the atoms introduces variation in the simulated fragmentation dynamics.

Fragmentation channels were separated by a condition on the atoms' position at the final simulated time step. If the distance between two atoms at 2000 fs is larger than 10 au (529 pm), they are considered separated. According to this condition, the final states of the simulated trajectories are sorted into dissociation channels. Table 5.1 gives an overview of the branching ratios regarding different dissociation channels with respect to the initial excitation energy.

In addition, the ADMP simulations considered the spin state of the electronic ground state of the $\text{CH}_2\text{I}_2^{3+}$ molecule. The doublet and the quadruplet spin state were considered. However, the spin state showed only a minor influence on the resulting fragmentation branching ratios. Therefore, the results presented here are not differentiated according to the spin state.

The dissociation channels observed in the ADMP simulations are two-body fragmentation into $\text{I}/\text{CH}_2\text{I}$ and H/CHI_2 as well as three-body fragmentation into $\text{CH}_2/\text{I}/\text{I}$ and $\text{H}/\text{I}/\text{CHI}$. The calculation does not take into account charge distribution. It is therefore not known which fragment has which charge state. The two dissociation channels $\text{I}/\text{CH}_2\text{I}$ and $\text{CH}_2/\text{I}/\text{I}$ are the most prominent coincident ion groups detected in the measurement (as shown in Figure 5.1). The other two channels with hydrogen fragments have not been detected during the measurement. For an initial energy of 1 eV, all simulation instances lead to the dissociation into a single iodine atom and the remaining CH_2I group. For higher energy values the branching ratio shifts towards three-body dissociation into $\text{CH}_2/\text{I}/\text{I}$ with minor contributions in the other two channels. In the 5 eV case, most of the molecules dissociate into two iodine atoms and the CH_2 group.

The final momentum correlation of the $\text{CH}_2/\text{I}/\text{I}$ fragmentations is shown in a Newton plot in Figure 5.11. Compared to the Newton plot of the measured coincident ions in Figure 5.8, the simulation reproduces the inner ring structure with a radius of just below 200 au. The distribution of the two prominent maxima at the upper and lower end of the ring is not seen in the simulation. The outer ring structure visible in the data, which is indicative of the sequential fragmentation pathway, is not reproduced by the ADMP simulation.

From the trajectory data of the simulation output it is possible to identify the time step when dissociations occur. Dissociation of one atom from another is defined as the time when the distance between the two respective atoms crossed the threshold of 10 au for the last time. In Figure 5.12 the dissociation times of the first and the second iodine atom from the carbon atom are plotted. Only the $\text{CH}_2/\text{I}/\text{I}$ channel has been considered here. It can be seen that in most of the simulation instances the first iodine atom leaves the molecule before the 100 fs mark. Dissociation of the CH_2I group then follows shortly after the emission of the first iodine. Fragmentation into three particles has been completed in most cases before 150 fs. Only in a few cases does the intermediate CH_2I group live for longer than 100 fs.

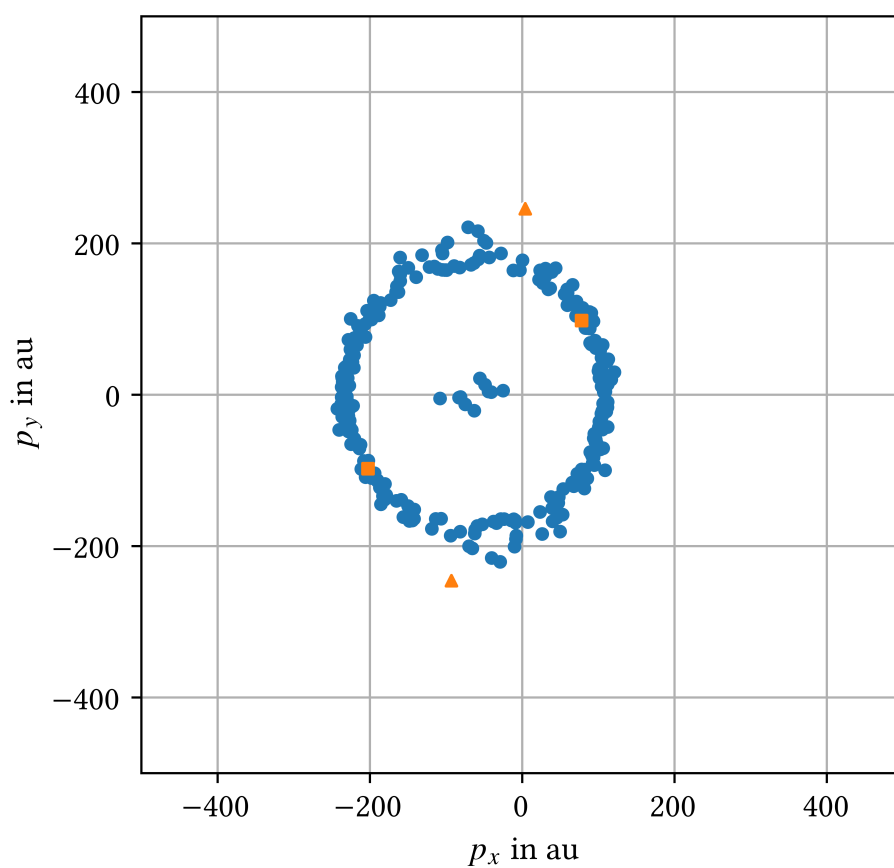


Figure 5.11: Newton plot of triple-ion coincidence channel $\text{CH}_2^+ + \text{I}^+ + \text{I}^+$ as simulated by Martín. 3 eV and 5 eV initial excitation energies combined, 2 ps simulation duration, 0.1 fs time step. The momentum of the C atom is oriented along the positive x -axis (not plotted). The hydrogen atoms are ignored.

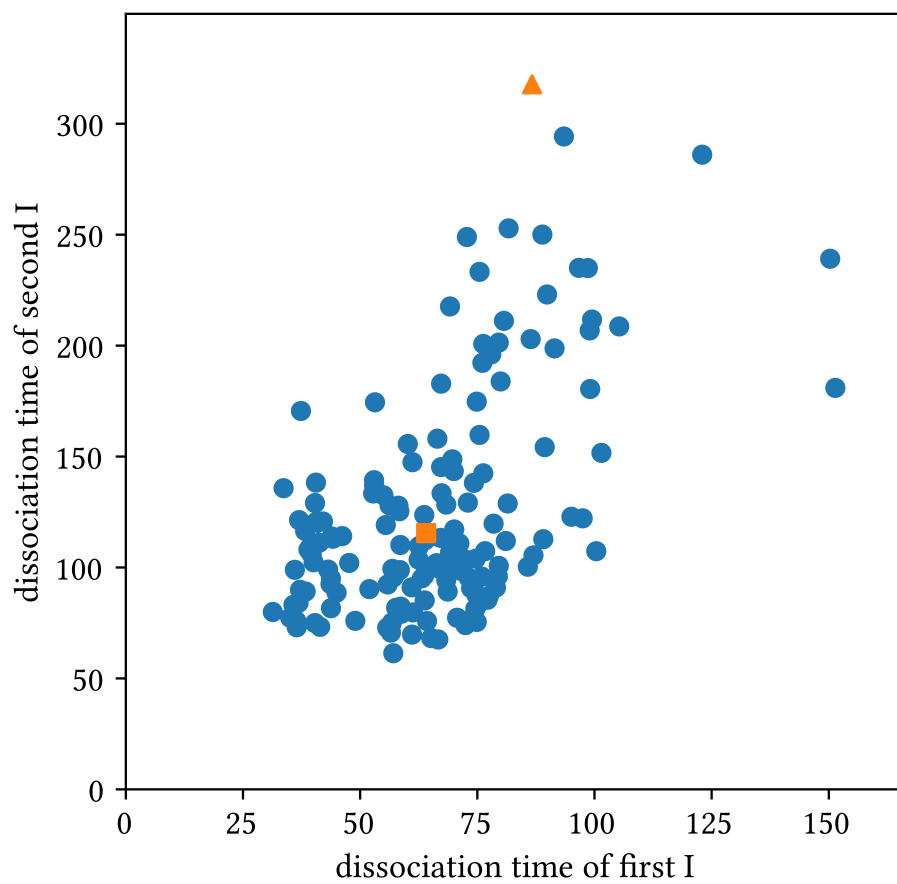


Figure 5.12: Correlation of the dissociation times of the two iodine atoms.

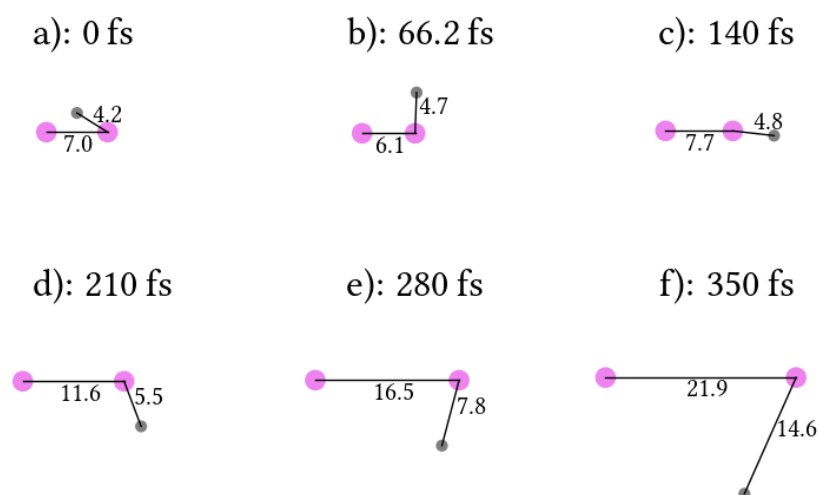


Figure 5.13: Pictures of molecular geometry at different time steps during ADMP simulation. The instance shown here has the latest dissociation time of the CH₂I group, 317.8 fs. The iodine atoms are shown in violet, the carbon atom in grey. The hydrogen atoms are ignored. The geometries are displayed in the centre of mass reference frame.

Figure 5.13 shows pictures of molecular geometry at different time steps during one of the simulation instances. The simulation run shown¹ is the one with the latest dissociation time of the CH_2I group, which is 317.8 fs (indicated by an orange triangle in the dissociation time correlation plot in Figure 5.12).

The pictures show the relative position of the two iodine atoms and the carbon atom in the centre of mass frame. The hydrogen atoms are not shown. The thin lines represent the distances between the positions of the atoms. From the original ground state geometry, the carbon atom moves outward and rotates around one of the iodine atoms. During the first few tens of femtoseconds the distance between the iodine atoms becomes smaller, reaching its minimum at 66.2 fs. Then, the I–I distance increases again while the carbon atom continues to rotate around the iodine it is attached to. These motions continue until finally, after approximately three quarters of a full rotation, the carbon atom separates from the iodine, resulting in fragmentation of the CH_2I group.

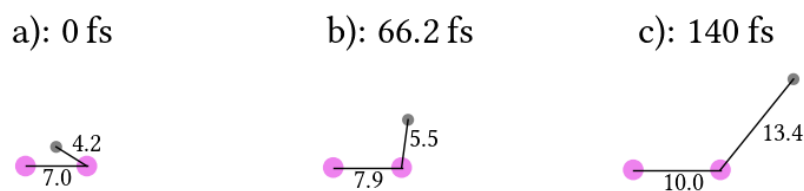


Figure 5.14: Same as Figure 5.13, but for simulation instance where the dissociation times for both iodine atoms are close to the respective mean dissociation time regarding all instances.

The molecular geometry of a different simulation instance is shown in Figure 5.14. There, the dissociation times of the two iodine atoms are close to the mean values of all instances (indicated in the dissociation time correlation plot by an orange square, see Figure 5.12)². The two iodine atoms show no significant initial reduction in their distance while the carbon atom briefly rotates around one of the iodine atoms. After approximately a quarter of a rotation it dissociates and the three-body fragmentation is complete. This behaviour is much more similar to the concerted fragmentation pathway than to the sequential dissociation,

¹The instance has the reference $\text{CH}_2\text{I}_2.\text{Q}3.\text{M}4.\text{NKE}183747.\text{trj}050$, meaning quadruplet spin state and 5 eV initial energy.

²The instance has the reference $\text{CH}_2\text{I}_2.\text{Q}3.\text{M}2.\text{NKE}183747.\text{trj}016$, meaning doublet spin state and 5 eV initial energy.

which is reflected in the momentum correlation seen in the Newton plot, where the iodine momenta of this simulation instance have been highlighted by orange squares.

The rotation of the intermediate CH_2I molecule is plausible in light of the measurements performed in this work and others [42, 49, 67], where sequential dissociation pathways of molecules have been detected. The observed momentum correlations are explained by the existence of a rotating intermediate molecule. However, in order to cause the observed ring structure in a Newton plot characteristic for sequential fragmentation, the lifetime of the intermediate step must be long compared to its rotational period. The intermediate molecule must ‘forget’ its original orientation in order to create the closed rings in the Newton plot. If dissociation of the intermediate molecular state occurs before even a single full rotation has been completed, as in all instances of the ADMP simulations, the Newton plot momentum correlation can not show closed rings. The latest dissociation of the CH_2I group observed for any simulation instance creates momenta of the fragmentation products that are quite distinct from the other more short-lived instances, as can be seen by the ion pair in the Newton plot highlighted by the orange triangles.

The short lifetime of the simulated CH_2I group (compared to its rotational period) is therefore the most probable reason why the simulation does not reproduce the momentum correlation characteristics of sequential fragmentation observed during this measurement.

5.2 Charge transfer in diiodomethane dissociation fragments

One-photon absorption can trigger dissociation of CH_2I_2 in various ways, as described in the previous section. When a second photon is absorbed, in general, higher charge states of the created ions are detected. If there is a time delay between the two photon absorption events, for some ions the detection rate and the kinetic energy varies with the adjusted time delay. Varying the delay between the pump and probe pulse probes the dissociating system at different times during its development. The result is a kinetic energy release (KER) that changes with the delay. Of special interest is the delay-dependent detection rate for some ion coincidences. This effect shows that the formation of some ionic charge states strongly depends on the time delay between the pump and probe pulses. Charge

transfer between the ions at small time delay and therefore short distances are the most likely explanation for the delay-dependent detection rates.

This section focuses on the most well-understood fragmentation channels detected, which are the two-ion channel $I^{+++} + CH_2I^+$ (Section 5.2.1) and the two interrelated three-ion coincidences $CH_2^+ + I^{+++} + I^+$ and $CH_2^+ + I^{++} + I^{++}$ (Section 5.2.2). Some ions have been detected in coincidence, such as $I^{++} + CH_2I^{++}$ and $I^{+++} + CH_2I^{++}$, but the total number of detected coincidence events is not sufficient to make any clear statement about the details of these dissociations. Other coincidence channels have been measured in sufficient numbers but they are still subject to ongoing analysis.

5.2.1 Dynamics of two-ion dissociation channel $I^{+++} + CH_2I^+$

The coincidence channel $I^{+++} + CH_2I^+$ is characterised by an asymmetric charge distribution between the two fragments. Three possible pathways could lead to the formation of this ion pair (see Figure 5.15): After the first photon absorption followed by Auger decay, the molecule fragments into the two singly charged ions I^+ and CH_2I^+ . This is one of the most likely fragmentation pathways for diiodomethane in this experiment. Photon absorption at the CH_2I^+ ion would most likely lead to a different fragmentation channel through breakup of the most likely then triply charged CH_2I group. If the I^+ ion absorbs another photon, inner-valence ionisation can occur, followed by Auger decay, which increases its charge state to $3+$. This process is sensitive to the time delay between the two FEL pulses because over time the distance between the two ions in the $I^+ + CH_2I^+$ dissociation channel increases due to Coulomb explosion. When the delay is small, the distance between the initial fragments is small and the change in charge state from I^+ to I^{+++} adds a high amount of potential energy to the ions. As a result, the observed KER is high. In contrast, for long delays, the two initial fragments have already separated by a larger distance and a smaller amount of potential energy is left between them. When a second photon then further ionises the I^+ ion, the energy increase is smaller and the KER is lower. The asymptotic limit of the decreasing KER for increasing delay is the energy release of the initial $I^+ + CH_2I^+$ fragmentation.

A different possible dissociation pathway could proceed via a stable intermediate original molecule. Since some $CH_2I_2^{++}$ ions have been found to be stable on the microsecond timescale, it is possible that such an ion remains stable for the time delay between the two FEL pulses. It can then absorb a second photon from the probe pulse which ejects two more electrons from the molecule which

initiates fragmentation. Because of the stability of the $\text{CH}_2\text{I}_2^{++}$ ion, the KER of the subsequent dissociation would be independent of the time delay, except for eventual changes in the molecular geometry caused by the first ionisation. The result would be a delay-independent KER signal. However, as is shown later, this process is not observed during this measurement.

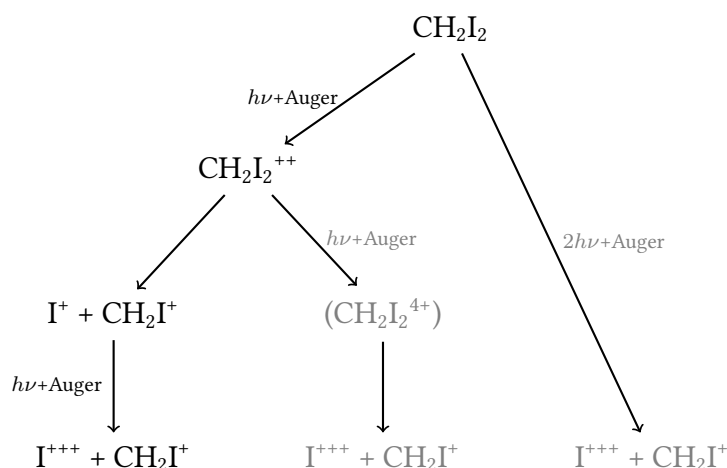


Figure 5.15: Possible dissociation pathways for the creation of an $\text{I}^{+++} + \text{CH}_2\text{I}^+$ ion pair from CH_2I_2 via two inner-valence ionisations followed by Auger decay. The delay-independent pathways via stable $\text{CH}_2\text{I}_2^{++}$ and via absorption of two photons from the same pulse (both in grey) are not observed.

Last, it is possible that the two absorbed photons originate from the same FEL pulse, either the pump or the probe pulse. Then, the other pulse would have no effect on the dynamics and a delay-independent KER is expected as well. This pathway is also not observed in the measurement.

When displaying the KER of the $\text{I}^{+++} + \text{CH}_2\text{I}^+$ fragmentation channel with respect to the time delay, as shown in Figure 5.16, several aspects are observed:

- There is no delay-independent kinetic energy release for the $\text{I}^{+++} + \text{CH}_2\text{I}^+$ fragmentation channel. This means that the two hypothetical delay-independent fragmentation pathways described above are not observed.
- The KER of the $\text{I}^{+++} + \text{CH}_2\text{I}^+$ coincidence decreases with increasing delay, as expected for an intermediate dissociating $\text{I}^+ + \text{CH}_2\text{I}^+$ state. At short delays, the maximum observed KER is around 9 eV. It decreases to around 5 eV for a delay of 1 ps. The KER is expected to decrease further towards the KER

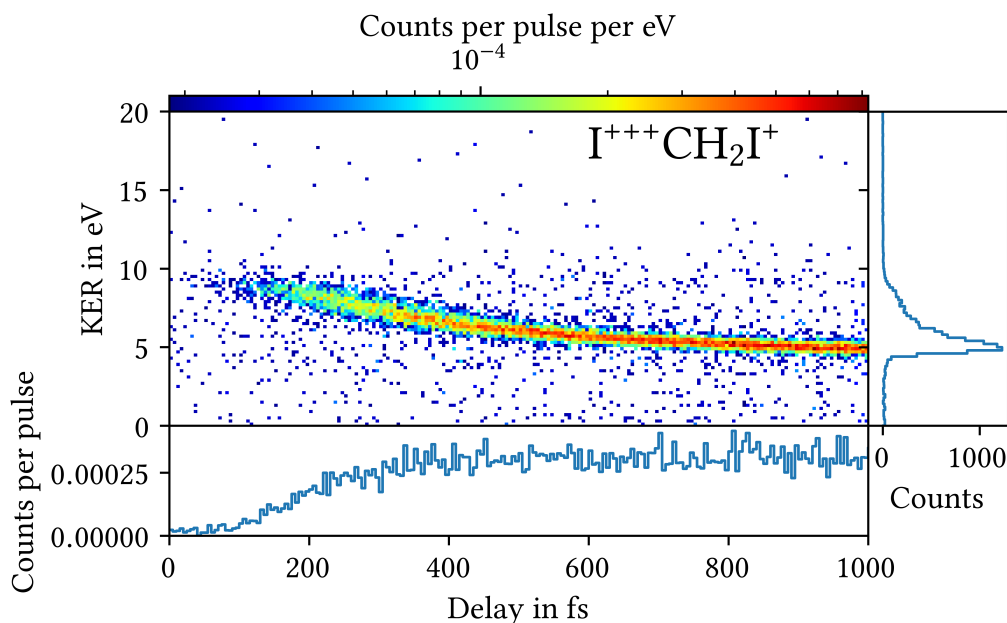


Figure 5.16: KER vs. delay histogram of the $I^{+++} + CH_2I^+$ coincidence channel.

of the $I^+ + CH_2I^+$ dissociation which was measured to be around 3.9 eV in the previous section.

- For short delays, the detection rate for $I^{+++} + CH_2I^+$ coincidence events decreases significantly. Almost no events are detected for delays between zero and 100 fs. For increasing delay the rate increases and reaches a plateau between 350 and 400 fs.

The interpretation of these observations is that the ion pair $I^{+++} + CH_2I^+$ is formed via the intermediate dissociation state of $I^+ + CH_2I^+$. When the probe pulse arrives, it causes further ionisation of the iodine ion. If the time delay is long, the distance between the CH_2I^+ and the iodine ion has increased sufficiently such that the two ions are isolated and the I^+ is turned into an I^{+++} ion. This explains the decreasing kinetic energy for increasing delay.

For short delays, the $I^{+++} + CH_2I^+$ fragmentation channel is suppressed because charge transfer occurs between the I^{+++} ion and the CH_2I^+ group such that the final charge state of the iodine ion is lower than 3+. Such events would then not be counted as $I^{+++} + CH_2I^+$ coincidences as they are removed from this channel.

It is for this case not possible to determine the ion species that result from the charge transfer. The coincidence channel $I^{++} + CH_2I^{++}$, which is one possible

candidate, has not been detected in sufficient numbers to make any statement about delay-dependent behaviour. The formation of the the three-ion coincidence channel $\text{CH}_2^+ + \text{I}^{++} + \text{I}^+$, a different candidate possibly formed by fragmentation of the CH_2I group after charge transfer occurred, is subject of current analysis and has not been fully understood yet. However, possible ionic products resulting from charge transfer have been detected in the two three-ion coincidence channels $\text{CH}_2^+ + \text{I}^{+++} + \text{I}^+$ and $\text{CH}_2^+ + \text{I}^{++} + \text{I}^{++}$, as is explained in the next Subsection.

5.2.2 Charge transfer dynamics in three-ion dissociation channels

The dissociation channel $\text{CH}_2^+ + \text{I}^{+++} + \text{I}^+$ displays a similar behaviour as the previously described two-body dissociation $\text{I}^{+++} + \text{CH}_2\text{I}^+$ regarding KER changes with delay. When observing the kinetic energy release of this three-ion channel, as shown in Figure 5.18, the same general features appear: The count rate of the channel is lower for small delay values, increases for larger delay and reaches a plateau at approximately 200 fs. The KER decreases with increasing delay from above 20 eV to an asymptotic value of around 15 eV. No KER distribution constant with the delay is observed.

The interpretation is that the formation of $\text{CH}_2^+ + \text{I}^{+++} + \text{I}^+$ occurs via the precursor dissociation channel $\text{CH}_2^+ + \text{I}^+ + \text{I}^+$. The different fragmentation pathways are schematically represented in Figure 5.17. The three singly charged ions are created from the original molecule by one-photon absorption followed by double Auger decay. When at long delay values the second FEL pulse arrives, the absorption of a second photon at one of the I^+ ions increases its charge state to 3+. This process explains the decreasing KER with increasing delay. For the maximum delay value of 1 ps the KER is around 15 eV which is within the KER distribution of the $\text{CH}_2^+ + \text{I}^+ + \text{I}^+$ channel, supporting the identification of this precursor state. Similarly to the coincident I^{+++} and CH_2I^+ ions, the interpretation for small delay values is that charge transfer occurs and suppresses the detection rate of the $\text{CH}_2^+ + \text{I}^{+++} + \text{I}^+$ channel.

The origin of the electron that is transferred to the I^{+++} ion could, in principle, be either the other iodine atom or the methylene group. As stated before, fragments of the CH_2 group as well as doubly charged CH_2^{++} ions have not been identified. It must therefore be stated that charge transfer between the I^{+++} and the CH_2^+ ions is considered a possibility, but it has not been detected in this work. How-

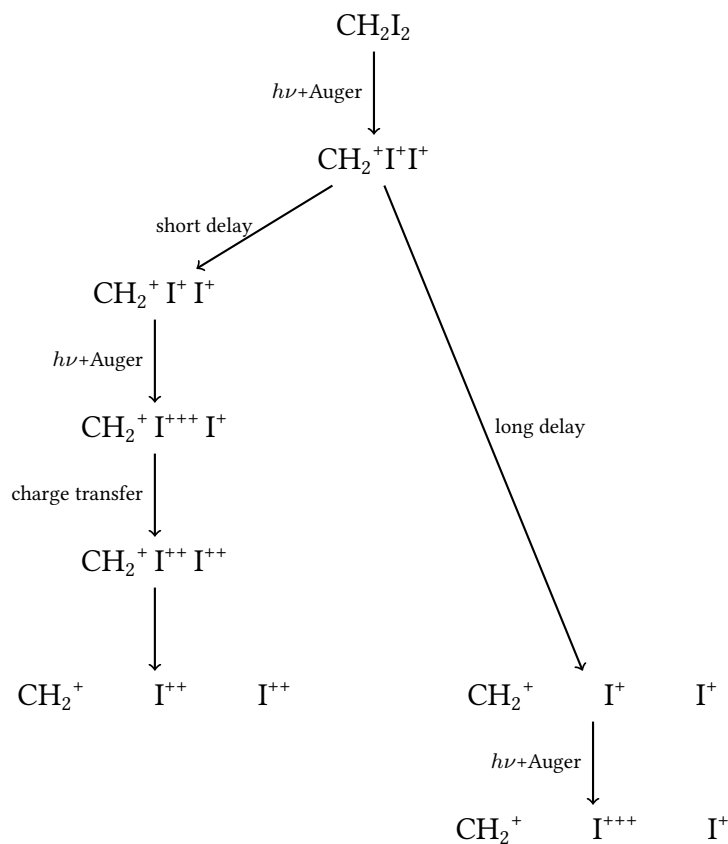


Figure 5.17: Fragmentation pathways leading to $\text{CH}_2^+ + \text{I}^{++} + \text{I}^{++}$ via charge transfer for short delay values or $\text{CH}_2^+ + \text{I}^{+++} + \text{I}^+$ for long delay values.

ever, charge transfer between the two iodine ions would lead to two I^{++} ions which have indeed been detected in coincidence with the CH_2^+ ion.

The $\text{CH}_2^+ + \text{I}^{++} + \text{I}^{++}$ coincidence channel shows a different development of the KER value with FEL pulse delay, as shown in Figure 5.19. There is a KER distribution between 25 and 35 eV that is constant with the delay between the two pulses. At delay values lower than 200 fs, the count rate of the $\text{CH}_2^+ + \text{I}^{++} + \text{I}^{++}$ channel is increased compared to longer delays. In this range the KER values appear to have a similar distribution compared to the KER-independent feature, but with a slight trend towards lower KER for longer delay.

Because there are at least two photons required for the creation of this ion triple, it is possible that all photons are absorbed during one of the FEL pulses. This effectively results in a kinetic energy release independent from the pulse delay, because no photons are absorbed from one of the pulses, either the pump or the

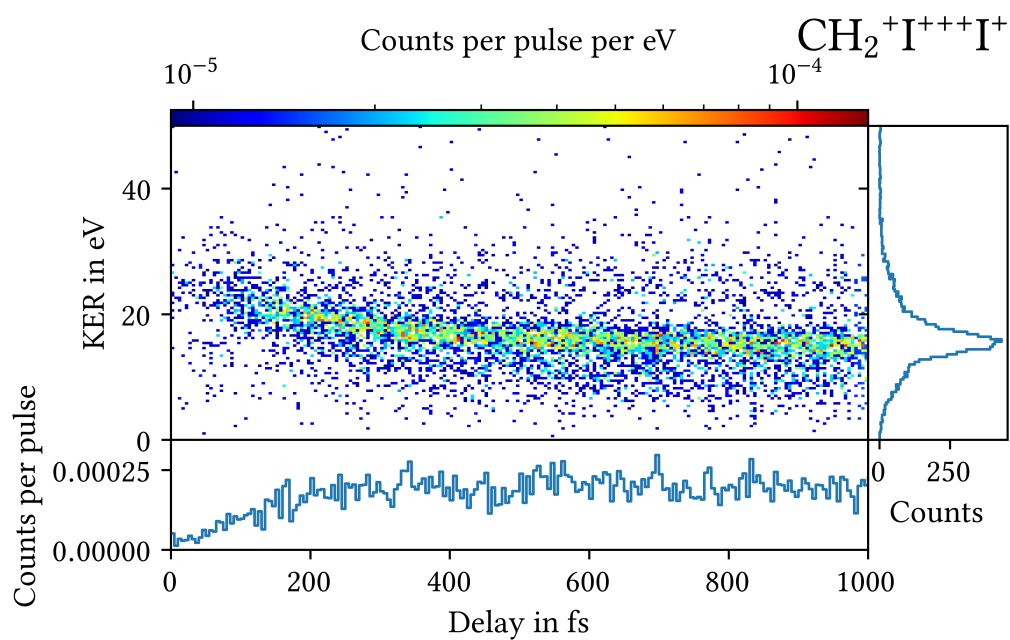


Figure 5.18: KER vs. delay histogram of the $\text{CH}_2^+ + \text{I}^{+++} + \text{I}^+$ coincidence channel.

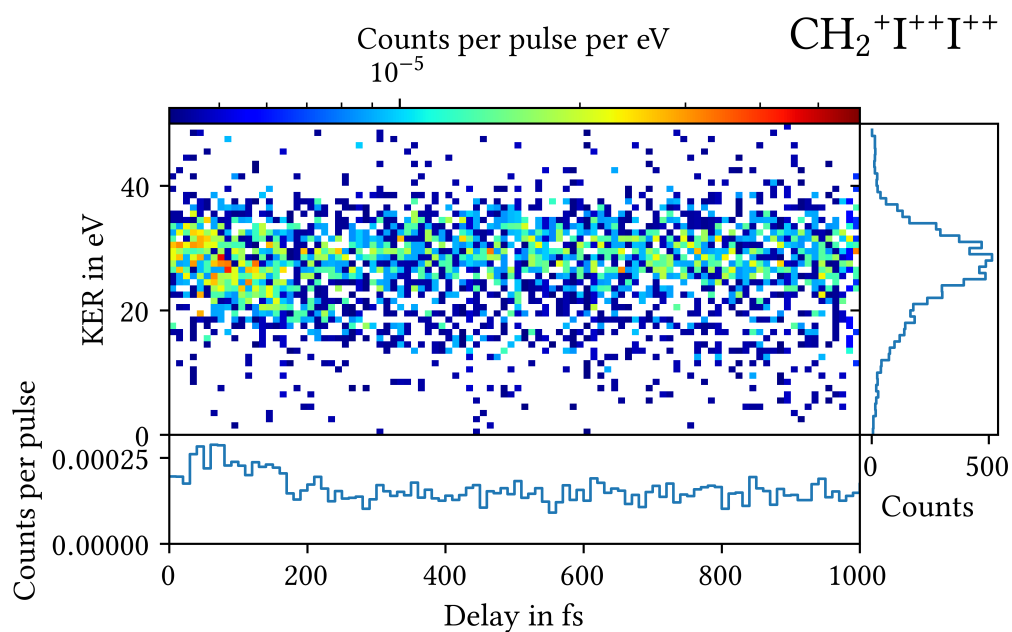


Figure 5.19: KER vs. delay histogram of the $\text{CH}_2^+ + \text{I}^{++} + \text{I}^{++}$ coincidence channel.

probe pulse. It is therefore likely that the constant KER distribution is either created by two-photon absorption in short succession from one FEL pulse or possibly via an intermediate stable $\text{CH}_2\text{I}_2^{++}$ ion. Those processes are indistinguishable in the presented data.

At delay values below 200 fs, the increased rate of $\text{CH}_2^+ + \text{I}^{++} + \text{I}^{++}$ coincidences is interpreted such that the channel is additionally populated by charge transfer from $\text{CH}_2^+ + \text{I}^{+++} + \text{I}^+$ precursor states where an electron is transferred from the I^+ to the I^{+++} , creating two doubly charged iodine ions.

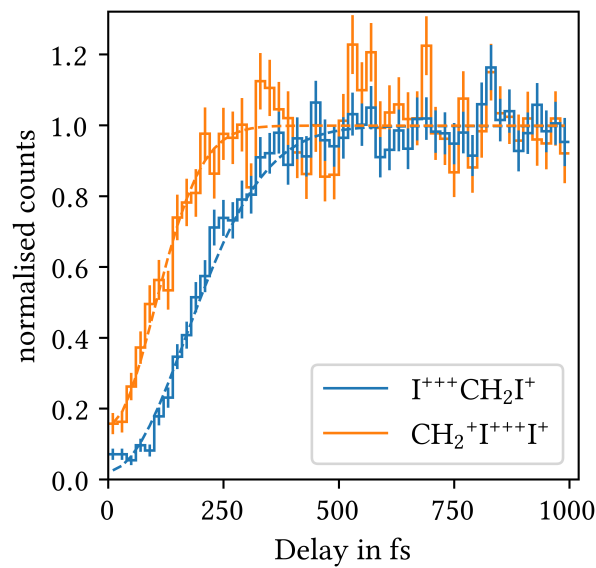


Figure 5.20: Detection rate of coincidence channels $\text{I}^{+++} + \text{CH}_2\text{I}^+$ and $\text{CH}_2^+ + \text{I}^{+++} + \text{I}^+$. The rates have been normalised to their mean value between 680 and 1000 fs. The dashed lines represent a Gaussian fit to each delay-dependent rate. The half width at half depth is (200 ± 11) fs for $\text{I}^{+++} + \text{CH}_2\text{I}^+$ and (119 ± 15) fs for $\text{CH}_2^+ + \text{I}^{+++} + \text{I}^+$.

From this change in detection rate it is possible to determine the timescale of charge transfer in both scenarios. The delay-dependent detection rate for both coincidence channels $\text{I}^{+++} + \text{CH}_2\text{I}^+$ and $\text{CH}_2^+ + \text{I}^{+++} + \text{I}^+$ is shown in Figure 5.20. Both rates have been normalised to their respective mean values at delays between 680 and 1000 fs. The detection rates have been computed by dividing the detected events in a specific delay bin by the FEL pulse number in that delay bin. The error bars are obtained by using the square root of the detected events as uncertainty, according to a Poisson distribution of the number of events in a certain time frame. A Gaussian function has been fitted to each data set with the condi-

tion that the minimum is at zero delay. The dashed lines represent the fit function with the optimised parameters.

For the $I^{+++} + CH_2I^+$ detection rate, the half width at half depth (HWHD) of the distribution is (200 ± 11) fs, for the $CH_2^+ + I^{+++} + I^+$ rate it is (119 ± 15) fs. The HWHD has been calculated from the standard deviation parameter σ of the Gaussian fit function, where $HWHD = \sqrt{2 \log 2} \sigma$. The error of the HWHD has been derived from the parameter fit covariance matrix.

The timescale for charge transfer in $I^{+++} + CH_2I^+$ is significantly longer than in $CH_2^+ + I^{+++} + I^+$. This can be understood when considering the precursor states of these two channels, $I^+ + CH_2I^+$ and $CH_2^+ + I^+ + I^+$, respectively. The Coulomb repulsion in the case where three charges are present is stronger than for the two-ion case. This results in an increased acceleration of the Coulomb explosion, leading to a faster increase in distance between the fragments. Therefore, the $CH_2^+ + I^+ + I^+$ precursor leaves a smaller time window for the possibility of charge transfer.

A delay-dependent decrease in I^{+++} ion yield from diiodomethane dissociation has been observed by [17] in an XUV-pump XUV-probe experiment at 82.7 eV photon energy. There, ions were not detected in coincidence, and only the delay-dependent detection yield of triply charged iodine is presented. The depletion of I^{+++} formation for small delays is similarly interpreted as an effect of charge transfer from the other fragments to the I^{+++} ion. In addition, the same measurement was performed for I^{+++} ion yield from CH_3I ions. There, a similar depletion for small delays is observed and interpreted as an effect of charge transfer as well.

The timescales for charge transfer reported by [17] are (in HWHD)³ (146 ± 15) fs for CH_2I_2 and (60 ± 8) fs for CH_3I . Because this was not a coincidence measurement, the change in I^{+++} ion detection rate is probably caused by a mixture of different dissociation channels that result in the formation of triply charged iodine ions. In the present work, the coincident detection of all ionic fragments allows for the separation of dissociation channels and their different charge transfer timescales.

Additionally, charge transfer is known to occur between differently charged iodine ions at small distances, as reported by [60]. There, molecular iodine (I_2) was irradiated by two XUV pulses in a pump-probe measurement at 87 eV photon energy. The created iodine ions were detected in coincidence. For short delays, the

³The original FWHM values reported are (292 ± 29) fs for CH_2I_2 and (120 ± 15) fs for CH_3I .

5.2.2 Charge transfer dynamics in three-ion dissociation channels

yield of coincidentally detected I^+ and I^{+++} decreases significantly while the yield of two coincident I^{++} ions increases. The HWHD of the depletion signal in the $I^{+++} + I^+$ channel is reported to be 128 fs. This value agrees within the uncertainty with the timescale presented here for the $CH_2^+ + I^{+++} + I^+$ channel where at least some of the charge transfer occurs between the singly and triply charged iodine ions.

Chapter 6

Summary and Outlook

The fragmentation dynamics of diiodomethane have been measured following irradiation with XUV pulses of 97.6 eV photon energy from the free-electron laser FLASH2. The results have been presented separated by one- and two-photon absorption.

In the one-photon case presented in Section 5.1, several two- and three-ion dissociation channels have been observed. The most prominent dissociations involved detachment of one or two iodine ions from the original molecule, leading to the ion coincidences $I^+ + CH_2I^+$ and $CH_2^+ + I^+ + I^+$.

Two different fragmentation pathways leading to the coincident detection of $CH_2^+ + I^+ + I^+$ have been identified: a concerted three-body dissociation and a sequential dissociation via an intermediate CH_2I^{++} ion. The latter creates characteristic ring structures in the Newton plot which displays momentum correlation between the fragments (see Figure 5.8). Similar ring structures have been identified for a variety of molecular fragmentations via intermediate steps [15, 42, 49]. In order to cause the observed ring structure, the intermediate molecular ions are expected to rotate with a period that is short compared to their lifetime such that there is no correlation between the direction of emission of the first ion and the orientation of the intermediate ion at the time of its subsequent dissociation. A drastically simplified classical model has been used to simulate the three-body fragmentation of diiodomethane based on the electrostatic repulsion between point charges. A sequential fragmentation via a rotating intermediate CH_2I^{++} molecular ion was simulated. The resulting momentum correlation between the three ions does qualitatively reproduce the experimental observation. This further indicates that the detected ring structures are in fact the result of a two-step fragmentation process.

Other simulations have been performed by Fernando Martín and Sergio Díaz-Tendero in the form of ADMP calculations, presented in Section 5.1.3. In a more general way, these simulations looked into the branching ratio of different dissociation channels of triply charged CH_2I_2 molecules. The precise nature of single and double Auger decay in diiodomethane are currently not known. Therefore, the simulation started with triply charged molecules in the electronic ground state, which is a simplification with regard to the expected state of the molecule after inner-valence photoionisation. The atoms of the molecule were given a random initial kinetic energy in order to approximate the excitation of rotational and vibrational states. The combined initial energy distributed among the atoms was set to fixed values of either 1, 3, or 5 eV. This initial energy was found to have a large influence on the branching ratio of the dissociation (as seen in Table 5.1).

In general, the results of the ADMP simulations approximate the dissociation dynamics of the concerted dissociation of diiodomethane into $\text{CH}_2^+ + \text{I}^+ + \text{I}^+$ with regard to total momentum distribution and momentum correlation. However, the ring structure characteristic for the sequential dissociation pathway does not emerge from the simulation results. A closer look into the timescales of the fragmentation reveals that both iodine atoms dissociate from the CH_2 group rather quickly within the first few 100 fs. There is a time difference between the dissociation of the first and the second iodine atom and the intermediate CH_2I group does briefly rotate, but the rotational period is, in all simulated dissociations, significantly longer than the lifetime of the intermediate molecule.

The absence of a rotating intermediate with a lifetime longer than the rotational period is the suspected reason why the ADMP simulations do not reproduce the momentum correlation of the sequential fragmentation pathway that was experimentally observed.

This shows that there is not yet a sufficient understanding of the dissociation dynamics for even small molecules like diiodomethane. With experimental setups such as the REMI at the atomic physics measurement endstation at FLASH2 and others it is now possible to investigate molecular dynamics during dissociation processes. Experimental results on competing fragmentation pathways, branching ratios and the properties of intermediate steps in breakup processes of molecular systems are a test for contemporary theoretical descriptions.

In the second part of the experimental results presented in Section 5.2, the timescales of charge transfer processes between dissociation fragments of diiodomethane have been determined. The two dissociation channels $\text{I}^{+++} + \text{CH}_2\text{I}^+$ and $\text{CH}_2^+ + \text{I}^{+++} + \text{I}^+$, both caused by the absorption of two XUV photons, have been identified. They show a kinetic energy release that decreases with the time delay between

the pump and probe pulse. Also, the rate of these coincident ion detection events decreases significantly for short delays. This was found to be a sign of charge transfer between the I^{+++} ion and the other fragments created in the dissociation process. In the case of the three-body dissociation $CH_2^+ + I^{+++} + I^+$, the decrease in rate for short delays coincides with an increase in the detection rate for the $CH_2^+ + I^{++} + I^{++}$ coincidence channel. This is interpreted as the result of a charge transfer between the I^{+++} ion and the I^+ ion at short distances.

The timescale for the charge transfer process was determined for both the two- and the three-body dissociation via a Gaussian fit to the delay-dependent detection rate. For $I^{+++} + CH_2I^+$, the half width at half depth (HWHD) was found to be (200 ± 11) fs. The timescale of the $CH_2^+ + I^{+++} + I^+$ channel was found to be substantially shorter at (119 ± 15) fs (see Figure 5.20). This indicates a faster increase in distance between the fragments in the three-body channel compared to the two-body dissociation. This behaviour is plausible when considering that the Coulomb repulsion in the $CH_2^+ + I^{+++} + I^+$ channel is larger because of the combined charge state of 5+, compared to 4+ in the $I^{+++} + CH_2I^+$ channel.

The timescales observed in this work are in agreement with previously determined charge transfer behaviour in I_2 [60] and CH_2I_2 [17]. The capability to observe different fragmentation channel-specific charge transfer timescales from the same target in the same measurement demonstrates the advantages of coincident ion spectroscopy.

In order to advance our understanding of molecular fragmentation dynamics and the nature of molecular systems in general, more work needs to be done both on the experimental and the theoretical side. The results presented here have shown that we lack a detailed understanding not only of the dissociation mechanisms of small molecules, but also of the effects that precede it, such as a precise electronic description of Auger decay and other de-excitation mechanisms in these systems. However, with the measurement techniques demonstrated in this work it is possible to observe kinematically complete dissociation events and investigate the nature of molecular systems. A better understanding of the electronic structure of excited dissociation products may be gained by analysing the electrons emitted by inner-valence ionisation and Auger decay. This can potentially illuminate the properties of intermediate molecular ions during sequential fragmentation, especially regarding their electronic and rotational-vibrational states. A different but similarly promising approach is to combine the measurement techniques of coincident ion-electron spectroscopy in a reaction microscope with the transient absorption method. This way, the observation of the final dissociation products can be compared with information on intermediate structural changes in the molecular geometry.

Appendix A

Atomic units

Atomic units are a system of measurement in atomic physics. Many quantities in this field have values that make atomic units a convenient reference system. The following is a list of atomic unit quantities and their corresponding values in SI units rounded to four significant figures.

dimension	SI value of one atomic unit (1 au)
length	5.292×10^{-11} m (Bohr radius)
time	2.419×10^{-17} s
charge	1.602×10^{-19} C (elemental charge)
mass	9.109×10^{-31} kg (electron mass)
velocity	2.188×10^6 m s ⁻¹
momentum	1.993×10^{-24} kg m s ⁻¹
energy	4.360×10^{-18} J (27.21 eV)
force	8.239×10^{-8} N
electric field	5.142×10^{11} V m ⁻¹

Appendix B

Inequation estimate

For simplicity, the indices for a specific ion are omitted. This is possible for the assumption that $x = 1$ and therefore $|p_2| = |p_1|$. Alternatively, $x = 0$ and therefore $|p_3| = |p_1|$ for the case of ion 3. It shall be shown that

$$\frac{p}{am} \gg \frac{p^2}{a^2m^2} \left(\frac{2s}{a} + \left(\frac{p}{am} \right)^2 \right)^{-\frac{1}{2}} \quad (\text{B.1})$$

Start with comparing the two terms in the inverse square root:

$$\begin{aligned} \left(\frac{p}{am} \right)^2 \cdot \left(\frac{2s}{a} \right)^{-1} &= \frac{p^2}{am^2 \cdot 2s} \quad | \quad a_2 = E \cdot \frac{q_2}{m} \\ &= \frac{p^2}{Eqm \cdot 2s} \quad | \quad p = \sqrt{2mQ}; \quad Q: \text{kinetic energy} \\ &= \frac{2mQ}{Eqm \cdot 2s} = \frac{Q}{Eqs} \end{aligned} \quad (\text{B.2})$$

This is the ratio of the ion's initial kinetic energy to the work exerted on the ion on its path from the interaction point to the detector. This ratio must be small for the experiment to work at all. If the electric field was too weak to significantly change the ion's kinetic energy, the ion would, in most cases, fly off and never reach the detector. The electric field strength is usually a few thousand volt per metre, leading to a kinetic energy change of a few hundred electronvolt per unit charge of an ion. The kinetic energy release of dissociation events is usually

below ten electronvolt. Therefore:

$$\begin{aligned}
& \frac{Q}{Eqs} \ll 1 \\
& \Rightarrow \frac{2s}{a} \gg \left(\frac{p}{am}\right)^2 \\
& \Rightarrow \frac{p^2}{a^2m^2} \left(\frac{2s}{a} + \left(\frac{p}{am}\right)^2\right)^{-\frac{1}{2}} \approx \frac{p^2}{a^2m^2} \sqrt{\frac{a}{2s}}
\end{aligned} \tag{B.3}$$

Now compare this to $\frac{p}{am}$:

$$\begin{aligned}
\frac{p^2}{a^2m^2} \sqrt{\frac{a}{2s}} \cdot \left(\frac{p}{am}\right)^{-1} &= \frac{p}{am} \sqrt{\frac{a}{2s}} = \frac{\sqrt{2mQ}}{Eq} \sqrt{\frac{Eq}{2sm}} \\
&= \sqrt{\frac{Q}{Eqs}}
\end{aligned} \tag{B.4}$$

As before, this fraction must be small for the experiment to work. It follows:

$$\frac{p}{am} \gg \frac{p^2}{a^2m^2} \left(\frac{2s}{a} + \left(\frac{p}{am}\right)^2\right)^{-\frac{1}{2}} \tag{B.5}$$

q.e.d.

Co-authored publications cited in this work

- [4] E. Appi et al. “Synchronized beamline at FLASH2 based on high-order harmonic generation for two-color dynamics studies”. *Review of Scientific Instruments* 92.12 (2021), p. 123004. ∞ (cit. on p. 53).
- [36] S. Meister et al. “Linear dichroism in few-photon ionization of laser-dressed helium”. *The European Physical Journal D* 75.205 (2021). ∞ (cit. on p. 53).
- [37] S. Meister et al. “Photoelectron spectroscopy of laser-dressed atomic helium”. *Phys. Rev. A* 102 (6 2020), p. 062809. ∞ (cit. on p. 53).
- [57] G. Schmid et al. “Reaction microscope endstation at FLASH2”. *Journal of Synchrotron Radiation* 26.3 (2019). ∞ (cit. on pp. 39, 41, 42, 47, 50, 51).
- [59] G. Schmid et al. “Tracing charge transfer in argon dimers by XUV-pump IR-probe experiments at FLASH”. *The Journal of Chemical Physics* 151.8 (2019), p. 084314. ∞ (cit. on pp. 1, 2, 6, 52).
- [63] M. Straub et al. “Differential Measurement of Electron Ejection after Two-Photon Two-Electron Excitation of Helium”. *Phys. Rev. Lett.* 129 (18 2022), p. 183204. ∞ (cit. on p. 54).

Co-authored publications not cited in this work

- [3] E. Appi et al. “A synchronized VUV light source based on high-order harmonic generation at FLASH”. *Scientific Reports* 10.6867 (2020). [∞](#).
- [5] S. Augustin et al. “Signatures of autoionization in the angular electron distribution in two-photon double ionization of Ar”. *Phys. Rev. A* 98 (3 2018), p. 033408. [∞](#).
- [35] S. Meister et al. “Atomic, Molecular and Cluster Science with the Reaction Microscope Endstation at FLASH2”. *Applied Sciences* 10.8 (2020). [∞](#).
- [58] G. Schmid et al. “Terahertz-Field-Induced Time Shifts in Atomic Photoemission”. *Phys. Rev. Lett.* 122 (7 2019), p. 073001. [∞](#).

Bibliography

- [1] W. Ackermann et al. “Operation of a free-electron laser from the extreme ultraviolet to the water window”. *Nature Photonics* 1 (2007), pp. 336–342. ∞ (cit. on p. 39).
- [2] P. Andersen et al. “Absolute cross sections for the photoionization of 4d electrons in Xe^+ and Xe^{2+} ions”. *Journal of Physics B: Atomic, Molecular and Optical Physics* 34.10 (2001), p. 2009. ∞ (cit. on pp. 7, 8).
- [6] B. H. Boo and N. Saito. “Dissociative multiple photoionization of Br_2 , IBr , and I_2 in the VUV and X-ray regions: a comparative study of the inner-shell processes involving $\text{Br}(3d,3p,3s)$ and $\text{I}(4d,4p,4s,3d,3p)$ ”. *Journal of Electron Spectroscopy and Related Phenomena* 127.3 (2002), pp. 139–152. ∞ (cit. on pp. 9, 70).
- [7] C. Brechignac and J. P. Connerade. “Giant resonances in free atoms and in clusters”. *Journal of Physics B: Atomic, Molecular and Optical Physics* 27.17 (1994), p. 3795. ∞ (cit. on p. 7).
- [8] A. Cartoni et al. “VUV Photofragmentation of CH_2I_2 : The $[\text{CH}_2\text{I}-\text{I}]^{\bullet+}$ Iododimethane Intermediate in the I-Loss Channel from $[\text{CH}_2\text{I}_2]^{\bullet+}$ ”. *The Journal of Physical Chemistry A* 119.16 (2015), pp. 3704–3709. ∞ (cit. on p. 12).
- [9] L. Chen et al. “Fragmentation of SO_2^{q+} ($q = 2-4$) induced by 1 keV electron collision”. *The Journal of Chemical Physics* 158.5 (2023), p. 054301. ∞ (cit. on p. 1).
- [10] J. P. Connerade. “The Non-Rydberg Spectroscopy of Atoms”. *Contemporary Physics* 19.5 (1978), pp. 415–447. ∞ (cit. on pp. 7, 8).
- [11] J. N. Cutler, G. M. Bancroft and K. H. Tan. “Ligand-field splittings and core-level linewidths in I 4d photoelectron spectra of iodine molecules”. *The Journal of Chemical Physics* 97.11 (1992), pp. 7932–7943. ∞ (cit. on pp. 9, 82).
- [12] Sergio Díaz-Tendero. personal communication. 18th Mar. 2023 (cit. on p. 83).

- [13] B. Faatz et al. “Simultaneous operation of two soft x-ray free-electron lasers driven by one linear accelerator”. *New Journal of Physics* 18.6 (2016), p. 062002. ∞ (cit. on p. 39).
- [14] R. Forbes et al. “Photoionization of the I 4d and valence orbitals of methyl iodide”. *Journal of Physics B: Atomic, Molecular and Optical Physics* 53.15 (2020), p. 155101. ∞ (cit. on p. 70).
- [15] R. Guillemin et al. “Selecting core-hole localization or delocalization in CS₂ by photofragmentation dynamics”. *Nature Communications* 6.6166 (2015). ∞ (cit. on p. 101).
- [16] I. V. Hertel and C.-P. Schulz. *Atoms, Molecules and Optical Physics 1, Atoms and Spectroscopy*. Springer-Verlag Berlin Heidelberg, 2015. ISBN: 978-3-642-54321-0 (cit. on p. 5).
- [17] M. Hollstein et al. “Ultrafast charge redistribution in small iodine containing molecules”. *New Journal of Physics* 21.3 (2019), p. 033017. ∞ (cit. on pp. 98, 103).
- [18] S. S. Iyengar et al. “*Ab initio* molecular dynamics: Propagating the density matrix with Gaussian orbitals. II. Generalizations based on mass-weighting, idempotency, energy conservation and choice of initial conditions”. *The Journal of Chemical Physics* 115.22 (2001), pp. 10291–10302. ∞ (cit. on p. 83).
- [19] M. R. Jana et al. “Ion-induced triple fragmentation of CO₂³⁺ into C⁺ + O⁺ + O⁺”. *Phys. Rev. A* 84 (6 2011), p. 062715. ∞ (cit. on p. 2).
- [20] R. Johnsen and M. A. Biondi. “Measurements of radiative charge-transfer reactions of doubly and singly charged rare-gas ions with rare-gas atoms at thermal energies”. *Phys. Rev. A* 18 (3 1978), pp. 996–1003. ∞ (cit. on pp. 1, 6).
- [21] J. E. Jones and S. Chapman. “On the determination of molecular fields. —II. From the equation of state of a gas”. *Proceedings of the Royal Society of London. Series A, Containing Papers of a Mathematical and Physical Character* 106.738 (1924), pp. 463–477. ∞ (cit. on p. 15).
- [22] B. Kaderiya. *Imaging photo-induced dynamics in halomethane molecules with coincident ion momentum spectroscopy*. eng. 2021 (cit. on pp. 12, 13, 81).
- [23] I. L. Karle. “Anomalous Electron Scattering from Iodine Vapor”. *J. Chem. Phys.* 23 (1955), p. 1739. ∞ (cit. on p. 75).
- [24] M. Kawasaki, S. J. Lee and R. Bersohn. “Photodissociation of molecular beams of methylene iodide and iodoform”. *The Journal of Chemical Physics* 63.2 (1975), pp. 809–814. ∞ (cit. on p. 12).

- [25] H. Kjeldsen et al. “Absolute photoionization cross sections of I^+ and I^{2+} in the $4d$ ionization region”. *Phys. Rev. A* 62 (2 2000), p. 020702. ∞ (cit. on p. 70).
- [26] N. G. Kling et al. “Time-resolved molecular dynamics of single and double hydrogen migration in ethanol”. *Nature Communications* 10.2813 (2019). ∞ (cit. on p. 2).
- [27] M. Krikunova et al. “Ultrafast photofragmentation dynamics of molecular iodine driven with timed XUV and near-infrared light pulses”. *The Journal of Chemical Physics* 134.2 (2011), p. 024313. ∞ (cit. on p. 8).
- [28] H. Kumar et al. “Three-body dissociation of OCS^{3+} : Separating sequential and concerted pathways”. *The Journal of Chemical Physics* 148.6 (2018), p. 064302. ∞ (cit. on p. 2).
- [29] T. Lang et al. *Versatile OPCPA Pump-Probe Laser System for the FLASH2 XUV FEL Beamline at DESY*. 2019, pp. 1–1 (cit. on p. 53).
- [30] F. Légaré et al. “Imaging the time-dependent structure of a molecule as it undergoes dynamics”. *Phys. Rev. A* 72 (5 2005), p. 052717. ∞ (cit. on p. 2).
- [31] D. W. Lindle et al. “Inner-shell photoemission from the iodine atom in CH_3I ”. *Phys. Rev. A* 30 (1 1984), pp. 239–244. ∞ (cit. on p. 70).
- [32] Y.-J. Liu et al. “Spin-Orbit Ab Initio Investigation of the Ultraviolet Photolysis of Diiodomethane”. *ChemPhysChem* 8.6 (2007), pp. 890–898. ∞ (cit. on p. 12).
- [33] U. Marvet and M. Dantus. “Femtosecond observation of a concerted chemical reaction”. *Chemical Physics Letters* 256.1 (1996), pp. 57–62. ∞ (cit. on p. 12).
- [34] W. Mehlhorn. “70 years of Auger spectroscopy, a historical perspective”. *Journal of Electron Spectroscopy and Related Phenomena* 93.1 (1998), pp. 1–15. ∞ (cit. on p. 9).
- [38] L. Meitner. “Über die β -Strahl-Spektren und ihren Zusammenhang mit der γ -Strahlung”. *Zeitschrift für Physik* 11 (1922), pp. 35–54. ∞ (cit. on p. 8).
- [39] W. J. Moore. *Physikalische Chemie*. Ed. by D. O. Hummel. Zweite Auflage. Walter de Gruyter, 1976. ISBN: 3-11-002127-7 (cit. on p. 18).
- [40] R. Moshhammer et al. “A 4π recoil-ion electron momentum analyzer: a high-resolution “microscope” for the investigation of the dynamics of atomic, molecular and nuclear reactions”. *Nuclear Instruments and Methods in Physics Research Section B: Beam Interactions with Materials and Atoms* 108.4 (1996), pp. 425–445. ∞ (cit. on p. 43).

- [41] L. Nahon, A. Svensson and P. Morin. “Experimental study of the $4d$ ionization continuum in atomic iodine by photoelectron and photoion spectroscopy”. *Phys. Rev. A* 43 (5 1991), pp. 2328–2337. ∞ (cit. on pp. 3, 7, 8, 69).
- [42] N. Neumann et al. “Fragmentation Dynamics of CO_2^{3+} Investigated by Multiple Electron Capture in Collisions with Slow Highly Charged Ions”. *Phys. Rev. Lett.* 104 (10 2010), p. 103201. ∞ (cit. on pp. 2, 81, 90, 101).
- [43] M. R. Panman et al. “Observing the Structural Evolution in the Photodissociation of Diiodomethane with Femtosecond Solution X-Ray Scattering”. *Phys. Rev. Lett.* 125 (22 2020), p. 226001. ∞ (cit. on p. 12).
- [44] L. Pauling. “THE NATURE OF THE CHEMICAL BOND. IV. THE ENERGY OF SINGLE BONDS AND THE RELATIVE ELECTRONEGATIVITY OF ATOMS”. *Journal of the American Chemical Society* 54.9 (1932), pp. 3570–3582. ∞ (cit. on p. 18).
- [45] F. Penent et al. “Multielectron Spectroscopy: The Xenon $4d$ Hole Double Auger Decay”. *Phys. Rev. Lett.* 95 (8 2005), p. 083002. ∞ (cit. on pp. 9, 10).
- [46] T. Pflüger. *Electron impact ionization studies of small rare gas clusters*. eng. 2012, Online–Ressource (158 S.) (Cit. on p. 49).
- [47] National Center for Biotechnology Information PubChem. *Diiodomethane ground state geometry, PubChem Identifier: CID 6346*. 2023. URL: <https://pubchem.ncbi.nlm.nih.gov/compound/diiodomethane#section=3D-Conformer> (visited on 10/03/2023) (cit. on pp. 11, 15).
- [48] J. Rajput and C. P. Safvan. “Orientation and alignment effects in ion-induced fragmentation of water: A triple coincidence study”. *The Journal of Chemical Physics* 141.16 (2014), p. 164313. ∞ (cit. on p. 1).
- [49] J. Rajput et al. “Native Frames: Disentangling Sequential from Concerted Three-Body Fragmentation”. *Phys. Rev. Lett.* 120 (10 2018), p. 103001. ∞ (cit. on pp. 2, 81, 90, 101).
- [50] M. Rebholz et al. “All-XUV Pump-Probe Transient Absorption Spectroscopy of the Structural Molecular Dynamics of Di-iodomethane”. *Phys. Rev. X* 11 (3 2021), p. 031001. ∞ (cit. on p. 12).
- [51] N. Saito et al. “Evidence of radiative charge transfer in argon dimers”. *Chemical Physics Letters* 441.1 (2007), pp. 16–19. ∞ (cit. on pp. 1, 6).
- [52] K. Sakai et al. “Electron-Transfer-Mediated Decay and Interatomic Coulombic Decay from the Triply Ionized States in Argon Dimers”. *Phys. Rev. Lett.* 106 (3 2011), p. 033401. ∞ (cit. on pp. 1, 6).

- [53] M. Satta et al. “A joint theoretical and experimental study on diiodomethane: Ions and neutrals in the gas phase”. *The Journal of Chemical Physics* 143.24 (2015), p. 244312. ∞ (cit. on p. 12).
- [54] H. B. Schlegel et al. “*Ab initio* molecular dynamics: Propagating the density matrix with Gaussian orbitals”. *The Journal of Chemical Physics* 114.22 (2001), pp. 9758–9763. ∞ (cit. on p. 83).
- [55] H. B. Schlegel et al. “*Ab initio* molecular dynamics: Propagating the density matrix with Gaussian orbitals. III. Comparison with Born–Oppenheimer dynamics”. *The Journal of Chemical Physics* 117.19 (2002), pp. 8694–8704. ∞ (cit. on p. 83).
- [56] G. Schmid. *Two-color pump-probe experiments on small quantum systems at the free-electron laser in Hamburg*. eng. Heidelberg, 2018, 1 Online–Ressource (230 Seiten) (cit. on pp. 39, 41–43, 52, 55).
- [60] K. Schnorr. *XUV pump-probe experiments on electron rearrangement and interatomic coulombic decay in diatomic molecules*. eng. Mit Zsfassungen in dt. und engl. Sprache. 2014, Online–Ressource (213 S.) (Cit. on pp. 9, 39, 45, 50, 53, 58, 66, 70, 98, 103).
- [61] K. Schnorr et al. “Time-resolved study of ICD in Ne dimers using FEL radiation”. *Journal of Electron Spectroscopy and Related Phenomena* 204 (2015), pp. 245–256. ∞ (cit. on pp. 1, 6, 52).
- [62] B. Siegmann et al. “Complete Coulomb fragmentation of CO₂ in collisions with 5.9 MeV u⁻¹ Xe¹⁸⁺ and Xe⁴³⁺”. *Journal of Physics B: Atomic, Molecular and Optical Physics* 35.17 (2002), p. 3755. ∞ (cit. on p. 1).
- [64] A. N. Tarnovsky et al. “Photodissociation dynamics of diiodomethane in solution”. *Chemical Physics Letters* 312.2 (1999), pp. 121–130. ∞ (cit. on p. 12).
- [65] Z. Wei et al. “Ultrafast dissociative ionization and large-amplitude vibrational wave packet dynamics of strong-field-ionized di-iodomethane”. *The Journal of Chemical Physics* 151.21 (2019), p. 214308. ∞ (cit. on p. 12).
- [66] J. L. Wiza. “Microchannel plate detectors”. *Nuclear Instruments and Methods* 162.1 (1979), pp. 587–601. ∞ (cit. on p. 47).
- [67] C. Wu et al. “Nonsequential and Sequential Fragmentation of CO₂³⁺ in Intense Laser Fields”. *Phys. Rev. Lett.* 110 (10 2013), p. 103601. ∞ (cit. on pp. 2, 81, 90).
- [68] J. Zobeley, R. Santra and L. S. Cederbaum. “Electronic decay in weakly bound heteroclusters: Energy transfer versus electron transfer”. *The Journal of Chemical Physics* 115.11 (2001), pp. 5076–5088. ∞ (cit. on pp. 1, 6).

Danksagung

An dieser Stelle möchte ich allen Menschen danken, die mich in meinem Leben und insbesondere in den letzten Jahren unterstützt haben. Dazu gehören:

- Robert, der es mir ermöglicht hat, an diesem interessanten Forschungsprojekt zu arbeiten, sowohl in Hamburg als auch in Heidelberg. Deine manchmal ungewöhnlichen aber stets praktischen und überaus hilfreichen Ratschläge weiß ich sehr zu schätzen.
- Thomas dafür, dass er mir ganz am Anfang von der Forschung am MPIK erzählt hat. Ich finde es großartig, dass du deine Begeisterung für die Wissenschaft stets mit anderen teilst.
- Hannes, der immer versteht, Computer das Richtige tun zu lassen. Danke für die vielen guten Zeiten im Büro und an der Beamline sowie deine große Hilfe bei komplizierten Fragen.
- meine ehemaligen Kollegen Kirsten, Sven, Georg, Severin, Patrizia und Yifan für viele erfolgreiche Messungen und ihre Bereitschaft, mir bei Fragen weiterzuhelfen.
- Claus Dieter für seine unerlässliche Hilfe bei der Vakuumtechnik.
- Marc Simon, Renaud Guillemin und Maria-Novella Piancastelli für die hervorragende Zusammenarbeit und die wissenschaftliche Unterstützung bei der Datenauswertung und -interpretation.
- Frans, der stets bereit war, die Wölfe fernzuhalten.
- die Photonenkoordinatoren, die Kontrollraum-Crew und alle Wissenschaftler und Techniker, welche den Betrieb des FLASH-FELs ermöglichen, für dieses Projekt und viele weitere.
- mein guter Freund Dr. Gianni Klesse, der stets bereit und fähig ist, mit neuen Sichtweisen weiterzuhelfen.
- Gergana, Carina, David, Weiyu, Hannes, Lennard und Gianni für das Korrekturlesen.
- die deutschen Steuerzahler für die Finanzierung dieses Forschungsprojekts.
- die großartigen Menschen der VEGA und des Astronomischen Sommerlagers für die unvergesslichen Zeiten, nicht nur unter dem Sternenhimmel und in der Werkstatt. Möget ihr euch stets vor den Thunfischen in Acht nehmen.

- meine Freundinnen und Freunde der Fechtschule Krifon.
- die anderen SpaceMaster, von denen und mit denen ich lernen durfte.
- meine Eltern, Großeltern und meine ganze Familie.

